INVESTIGATION OF SOOT OXIDATION KINETICS, NANOSTRUCTURE, AND SURFACE ELEMENTAL ANALYSIS

by

Joseph Douglas Levinthal

A dissertation submitted to the faculty of
The University of Utah
in partial fulfillment of the requirements for the degree of

Master of Science

Department of Chemical Engineering

The University of Utah

December 2013

The University of Utah Graduate School

STATEMENT OF THESIS APPROVAL

The thesis of **Joseph Douglas Levinthal**

has been approved by the following supervisory committee members:

JoAnn S. Lighty	, Chair	**August 16, 2013** Date Approved
Eric Eddings	, Member	**August 16, 2013** Date Approved
Marc Porter	, Member	**August 16, 2013** Date Approved

and by **Milind Deo** , Chair/Dean of

the Department/College/School of **Chemical Engineering**

and by David B. Kieda, Dean of The Graduate School.

ABSTRACT

The goal of this research was to provide a better understanding of how soot oxidation kinetics are affected by nanostructure, surface functional groups (SFGs) , C-C sp^2,C-C sp^3, phenol, carbonyl and carboxylic, pressure, and type of fuel. The oxidation kinetics of soot were studied using thermogravimetric analysis (TGA) to determine kinetic parameters such as the kinetic rate of oxidation, activation energy and pre-exponential factor using Arrhenius kinetics. High-resolution transmission electron microscope (HRTEM) was used to obtain images of the soot and an image analysis algorithm identified the fringe length and tortuosity of the soot samples, which are indications of soot nanostructure. A high-pressure TGA was used to partially oxidize samples at a range of pressures, which were then studied using image analysis to identify changes in the nanostructure. The surface functional groups were studied using X-ray photoelectron spectroscopy and CasaXPS, peak-fitting software was used for identification of the SFGs present. The more structured soot had higher activation energies and slower kinetic rates while soot with less structure demonstrated lower activation energies and faster kinetic rates. There was no significant correlation found between SFGs and oxidation behavior.

for my loving wife and son

TABLE OF CONTENTS

NOMENCLATURE

A	pre-exponential factor, $Pa^{-1}min^{-1}$
A_s	transaction area of the crucible, m^2
D_{AB}	bulk diffusivity between two components in a mixture,cm^2/s
D_e	molecular diffusion coefficient, m^2/s
$D_{eff,p}$	effective diffusion coefficient inside the particle, m^2/s
$D_{eff,1}$	effective diffusion coefficient between sample particles, m^2/s
E_a	activation energy of the reaction, kJ/mol
e	thickness of the particle layer, m
k_c	reaction rate constant, $Pa^{-1}min^{-1}$
k_s	intrinsic rate constant, s m/kg
k_s'	effective reaction rate constant, s/m
L	height of crucible, m
m_c	initial mass of soot, mg
m_p	mass of particle, kg
n	reaction order of oxygen
M_c	molecular weight of carbon, kg/mol
M_A	molecular weights of oxygen, kg/mol

M_B	molecular weights of nitrogen, kg/mol
p_{O_2}	partial pressure of oxygen, Pa
$p_{O_{2,x}}$	local partial oxygen pressure, Pa
$p_{O_{2,o}}$	oxygen partial pressure of bulk flow, Pa
$p_{O_{2,s}}$	partial pressure of oxygen at the surface of the particle layer, Pa
P_t	total pressure of the gas, atm
R_u	universal gas constant , J/kmol
S_g	specific surface area of a particle,m^2/kg
r_p	radius of the particle, m
$r'_{O_2,}$	actual total oxygen consumption rate, mol/s
T	absolute temperature, K
x	distance from the bottom of the crucible to a point inside a particle layer, m

GREEK SYMBOLS

β	stoichiometric coefficient, mol oxygen/ mol carbon
η_1	effectiveness factor for diffusion to the particle layer
η_p	effectiveness factor for diffusion to the particle
η_e	effectiveness factor for external diffusion
$\emptyset_1$	Thiele diffusion modulus between particles
$\emptyset_p$	Thiele diffusion modulus inside the particle
φ_1	porosity between particles
φ_p	porosity inside particles
$\rho_{b,p}$	bulk density of a particle, kg/m^3
$\rho_{b,1}$	bulk density of the soot sample layer, kg/m^3
τ_1	tortuosity between particles
τ_p	tortuosity in particles
Ω_{AB}	collision integral
σ_{AB}	force constants in the Lennard-Jones potential function

ACKNOWLEDGEMENTS

I would like to express my sincere appreciation to my advisor, Dr. JoAnn S. Lighty for her support getting into the graduate program and continued guidance during my studies.

I wish to thank my committee members, Dr. Eric Eddings and Dr. Marc Porter for their time and willingness to evaluate this dissertation.

I would like to express my gratitude to Dr. Cristiana Jaramillo; her continued guidance, assistance and knowledge made this research possible.

I would like to thank Mr. Dana Overacker for his patience, advice and the technical support he provided.

I am deeply thankful to my wife "Lindsey," her parents and my family for their continued support, help in raising our son, love and understanding that gave me this opportunity to pursue my passion.

This work is funded by the Department of Energy Basic Energy Sciences under Grant No DE-SC 0004769. Their support was greatly appreciated.

CHAPTER 1

MOTIVTION AND OBJECTIVES

1.1 Motivation

There is an established awareness of the negative health effects and environmental damages that are caused by soot emissions from diesel engines used in transportation applications. Soot particles are dangerous due to the large number of harmful substances that they carry and because the particles themselves are made up of often dangerous carbonaceous materials. Epidemiological studies show correlations between carbonaceous material in the atmosphere and adverse health effects including allergies, asthma, cardiovascular, and respiratory diseases (*1-3, 7*).

Soot is one of the largest man-made contributors to global warming. Soot pollutants are a significant cause of rapid warming in the Northern Hemisphere, changes in rainfall patterns of the Asian Monsoon, and the increasing snowmelt rate in Antarctica (*1-5*). The dark carbonaceous material in soot heats up the atmosphere by absorbing the incoming sunrays, radiating that heat into the atmosphere, and scattering the sunrays. On the surface of the snow and ice, soot warms and increases the snowmelt rate by reducing the light reflection abilities of the snow and ice (*5*).

A better understanding of how fuel additives, temperature and pressure affect the nanostructure and the oxidation kinetics of soot can be used to create more efficient methods of soot reduction and removal. One of the current strategies for reducing soot emissions includes trapping the soot particles within on-board diesel particulate filters (DPF), which are effective until the filter gets progressively loaded by filtering the soot laden flue gases, causing an increasing pressure drop, until regeneration takes place (*5*). Other strategies use biofuels or oxygenated fuels to lower the soot concentration produced by diesel engines. Metal catalysts can also be used in exhaust systems to remove pollutants and reduce soot emissions (*1-5*).

1.2 Objectives

The main objectives of this dissertation were to determine the role that soot nanostructure has in soot oxidation as a function of surface functional groups (SFGs), fuel composition, temperature, and pressure.

The work had the following objectives: (1) improve and optimize the ability of the flat-flame burner to create soot from a variety of fuel combinations, (2) determine kinetic parameters for several different model carbons and soots which were created from different surrogate fuels in the high-pressure thermogravimetric analyzer (high-pressure TGA) and TGA under varying temperatures and pressures, (3) relate the kinetic parameters to the nanostructure of the soot using High Resolution Transmission Electron Microscope (HRTEM) images and image analysis software to determine what effect soot nanostructure has on the kinetic parameters, (4) relate how different surrogate fuel formulations effect the nanostructure and kinetic rate of soot oxidation, and (5) determine

the effect surface functional groups (SFGs) have on the kinetic rate constant for the oxidation of soot.

1.3 References

1. Bockhorn H.; Soot Formation In Combustion: Mechanisms And Models; Springer-Verlag: New York, N.Y., 1994**.**

2. Bond T. C.; Doherty S. J.; Fahey D. W.; Bounding The Role Of Black Carbon In The Climate System: A Scientific Assessment Journal Of Geophysical Research. Atmospheres **2013,** *118*, 5380–5552.

3. Borosky G. L.; Journal of Organic Chemistry **1999,** *64*, 7738-7744.

4. Lighty J. S.; Veranth J. M.; Sarofim A. F., Journal of the Air & Waste Management Association **2000,** *50*, 1565-1618.

5. Mcenally C. S.; Pfefferle L. D., Combustion and Flame **2000,** *123*, 344-357.

6. Sarofim A. F.; Lighty J. S.; Eddings E. G., Fine Particles: Health Effects, Characterization, Mechanisms of Formation, and Modeling. 224th ACS National Meeting **2002,** 618-621.

7. Shiraiwa M.; Seizle K.; Poschl U.; Hazardous Components And Health Effects Of Atmospheric Aerosol Particles: Reactive Oxygen Species, Soot, Polycyclic Aromatic Compounds And Allergenic Proteins. Free Radical Research **2012,** *46*, 927-39.

CHAPTER 2

BACKGROUND

2.1 Soot Formation

Soot formation is a complex process with a great number of chemical and physical steps and is a major focus of experimental and theoretical studies. The steps behind soot formation are not completely understood, but the widely accepted reaction path that leads to the formation of soot in flames is illustrated in Figure 2.1 and described below. The major steps of soot formation are molecular precursor formation, particle inception, coagulation and soot growth, particle agglomeration of the primary particles to form chain-like aggregates, and oxidation (*4-8*).

The first step in the soot formation process is the formation of molecular precursors. This involves the oxidative pyrolysis of the fuel, which degrades into smaller hydrocarbons and free radicals. The reaction of the molecular precursors leads to the formation of ions, polyacetylenes, and polycyclic aromatic hydrocarbons (PAHs), which are the building blocks of soot (*4-15*). It is commonly thought that ions interact with free radicals, polyacetylenes, and the PAH repeatedly to create larger particles (*10, 11, 12*).

The frontier in combustion chemistry and soot prediction is the development of predictive reaction computer models. Chemical kinetic models use scientific data

collected via experiments and apply it to predictive models that can assess, and identify problems and be used to improve the experimental and theoretical work. Experimental and modeling studies support the hypothesis that the formation of soot from aliphatic fuels generally proceeds through the conversion of the aliphatic molecule to polycyclic aromatic compounds (PAHs), that undergo polymerization to soot (*4, 6-8, 13-16*). Forming of the PAHs is believed to be the rate-limiting step that leads to the formation of soot. There are many pathways proposed for the formation of the first aromatic ring.

The most common is the addition of acetylene to nC_4 radical, proceeding to the formation of benzene or phenyl radical by an aromatization process (*7*). Miller and Mellius (*17*) reported that nC_4 radicals transform to a resonantly stabilized isomer, and proposed a mechanism that involves self-combination of propargyl radicals, preceded by a series of cyclization steps to form benzene or phenyl rings. This mechanism is highly dependent on fuel and flame type. Alternative pathways for the formation of the first aromatic ring are the reactions between C_5H_5 and CH_3 radicals to form benzene or the combination of propargyl and acetylene to form cyclopentadienyl radical, which then proceeds to benzene (*7, 20*).

Once the first PAHs are formed, they continue to form higher-ordered aromatic species by hydrogen abstraction and acetylene addition (HACA) mechanism, or pathways involving resonantly stabilized free radicals (*6,7,13,14,22-24*). The HACA mechanism is a two-step process wherein the aromatic ring is activated by the hydrogen atom abstraction allowing for subsequent acetylene addition, promoting growth of PAHs and soot. Growth of the PAHs can also occur by the addition of acetylene to the chair

structure, known as the Diels-Alder reaction, which takes place at the edges of the PAHs (*15, 25, 26*).

Once the PAHs have gained enough mass they begin to form spherical particles. There are two theories for particle inception, either the physical condensation or chemical combination model. The Ammans et al. (*28*) physical condensation model showed that the partial pressure of the molecular precursors forces the heavier PAHs to condense physically into particles. The chemical growth showed that once the PAHs begin colliding and forming dimmers, trimmers and so on, until the first particle nucleus was formed (*7*).

Coagulation and surface reactions are occurring side by side to form larger particles and continue the soot growth. Coagulation is described as the process of individual particles colliding and being held together by interaction forces (*29-31*). Surface reactions involve the formation of active sites due to hydrogen abstraction and subsequent C_2H_2 addition from gas-phase. The surface growth of the particles is assumed to be dominated by the HACA mechanism (*3, 5-7, 13, 16, 22, 32*).

The final phase of soot growth is particle agglomeration, which is characterized by a decrease in surface growth and an increase in the particle size is called superficial aging. Figure 2.2 shows the formation of chain-like aggregates due to superficial aging (*4, 6, 33, 34*). Recent studies based on simulation results and mechanistic interpretation attribute superficial aging to a decrease in hydrogen atom concentration on the surface of the soot, decreasing the number of active sites on the particle surface.

2.2 Soot Oxidation

Oxidation, occurring throughout the soot formation process, is difficult to study under typical flame conditions. Therefore a method was created to characterize the oxidation of soot after it was created using the flat-flame burner and oxidized in the TGA.

The two major species that are widely accepted as soot oxidizers are O_2 and OH^* radicals (*4, 6, 7, 38-40)*. The other species present, H_2O, CO and CO_2, have been shown to be negligible under typical flame conditions (*4, 39, 41, 43, 44*). There has been a considerable amount of research on the formulation of semi-empirical correlations to improve the understanding of the soot oxidation process by O_2. Lee et al. (*41*) reported a first order reaction rate expression that is often cited and used in research. Nagle and Strickland-Constable (*40*) created a widely used expression for the oxidation of carbonaceous material by O_2. This semi-empirical model for the oxidation rate of soot assumed that the surface of the soot particles consist partially of reactive areas, A, and less reactive areas, B. This assumption is also used in some detailed models.

Oxidation of soot is commonly studied by measuring the weight change during oxidation. This weight change is often determined by using a thermogravimetric analyzer (TGA). Song et al. (*46*) have proposed a theoretical analysis to extract a rate constant based on the mass-loss curves measured under isothermal conditions. Further, other kinetic parameters of activation energy and a frequency factor or pre-exponential factor can be determined from the data.

In spite of significant progress in experimental studies, computer modeling, and theoretical interpretation of soot formation and oxidation, there are many aspects of this complex process that are not understood completely. Studies have focused on PAHs

reaction with O_2, NO_2 and NO in order to better understand soot formation and oxidation (*48, 49*). Cheng et al. proposed that PAHs physically deposit on the soot surface contributing to the soot growth process and the physical structure of the soot. The oxidation rate of soot particles is affected by physical and chemical modifications of its nanostructure by the addition of PAHs (*50*). The PAHs size, amount, structure, elemental composition, and functional groups depend on the type of fuel and operating conditions. To further pursue the goal of producing more reactive and ultimately less polluting soot, continued theoretical modeling and experimental studies are needed to better understand how the fuel and operating conditions can control the affect on PAHs formation and oxidation process.

2.3 References

1. Bockhorn H.; Soot Formation In Combustion: Mechanisms And Models; Springer-Verlag: New York, N.Y., 1995.

2. Lighty J. S.; Veranth J. M.; Sarofim A. F., Journal of the Air & Waste Management Association **2000,** *50*, 1565-1618.

3. Sarofim A. F.; Lighty J. S.; Eddings E. G., Fine Particles: Health Effects, Characterization, Mechanisms of Formation, and Modeling. 224th ACS National Meeting **2002,** 618-621.

4. Frenklach M.; Clary D. W.; Yuan T.; Gardiner W. C.; Stein S. E., Combustion Science and Technology, **1986,** *50*, 79 - 115.

5. Frenklach M., Physical Chemistry Chemical Physics, **2002,** *4*, 2028-2037.

6. Frenklach M.; Wang H., Soot Formation In Combustion: Mechanisms And Models. Springer-Verlag: New York, N.Y., 1994**,** 165-190.

7. Bartok W.; Sarofim A. F., Fossil Fuel Combustion: A Source Book, Wiley: New York, 1991.

8. Hall-Roberts V. J.; Hayhurst A. N.; Knight D. E.; Taylor S. G.; The Origin Of Soot In Flames: Is The Nucleus And Ion? Combustion and Flame **2000,** *120*, 578-584.

9. Homann K. H.; Wagner H. G., Proceedings of the Combustion Institute **1967,** *11* 71-379.

10. Homann K. H.; Wagner H. G., Proc. R. Soc. Lond. **1968,** *307*, 141-152.

11. Calcote H. F., Combustion and Flame **1957,** *1*, 385.

12. Calcote H. F.; Combustion and Flame **1981,** *42*, 215.

13. D'Anna A.; Violi A.; D'Alessio A.; Sarofim A. F., Combustion and Flame **2001,** *127*, 1995-2003.

14. Violi A.; Sarofim A. F.; Truong T. N., Combustion and Flame **2001,** *126*, 1506-1515.

15. Siegmann K.; Sattler K., Journal of Chemical Physics **2000,** *112*, 698-709.

16. Cullis C. F.; Read I. A.; Trimm D. L., Proceedings of the Combustion Institute **1967,** *11*, 391.

17. Miller J. A.; Melius C. F., Combustion and Flame **1992,** 21.

18. Mcenally C. S.; Pfefferle L. D., Combustion and Flame **2000,** *123*, 344-357.

19. Pope III C. A.; Burnett R. T.; Thurston G. D.; Thun M. J.; Calle E. E.; Krewski D.; Godleski J. J., Cardiovascular Mortality And Long-Term Exposure To Particulate Air Pollution. Circulation **2004,** *109*, 71-77.

20. Sidebotham G. W.; Glassman I., Combustion and Flame **1992,** *90*, 269.

21. Melius C. F.; Colvin M. E.; Marinov N. M.; Pit W. J.; Senkan S. M., Proceedings of the Combustion Institute **1996,** *26*, 685.

22. Winans R. E.; Tomczyk N. A.; Hunt J. E.; Solum M. S.; Pugmire R. J.; Jiang Y. J.; Fletcher T. H., Energy & Fuels **2007,** *21*, 2584-2593.

23. D'Anna A.; Violi A.; D'Alessio A., Combustion and Flame **2000,** *121*, 418-429.

24. D'Anna A.; D'Alessio A.; Kent J., Combustion and Flame **2001,** *125*, 1196-1206.

25. Violi A., Combustion and Flame **2004,** *139*, 279-287.

26. Siegmann K.; Hepp H.; Sattler K., Combustion Science and Technology **1995,** *109*, 165 - 181.

27. Frenklach M.; Ebert L. B., The Journal of Physical Chemistry **1988**, *92*, 561-563.

28. D'Anna A.; Rolando A.; Allouis C.; Minutolo P.; D'Alessio A., Proceedings of the Combustion Institute **2005,** *30*, 1449-1456.

29. Amann C. A.; Siegla D. C., Aerosol Science and Technology **1981,** *1*, 73 - 101.

30. D'Alessio A.; D'Anna A.; Gambi G.; Minutolo P., Journal of Aerosol Science **1998,** *29*, 397-409.

31. D'Alessio A.; D'Anna A.; Minutolo P.; Sgro L. A.; Violi A., Proceedings of the Combustion Institute **2000,** *28*, 2547-2554.

32. D'Alessio A.; Barone A. C.; Cau R.; D'Anna A.; Minutolo P., Proceedings of the Combustion Institute **2005**, *30*, 2595-2603.

33. Hwang J. Y.; Chung S. H., Combustion and Flame **2001,** *125*, 752.

34. Dobbins R. A.; Megaridis C. M., Langmuir **1987,** *3*, 254-259.

35. Palotàs A. P.; Feldermann C. J.; Sarofim A. F.; Vander Sande J. B., Microscopy Research and Technique **1996,** *33*, 266-278.

36. Harris S. J.; Weiner A. M., Combustion Science and Technology **1983,** *32*, 267 - 275.

37. Harris S. J.; Maricq M. M., Journal of Aerosol Science **2001,** *32*, 749-764.

38. Harris S. J.; Maricq M. M., Journal of Aerosol Science **2002,** *33*, 935-942.

39. Nagle J.; Strickland-Constable R. F., Proceedings of the Fifth Carbon Conference **1962,** 154-164.

40. Lee K. B.; Thring M. W.; Beer J. M., Combustion and Flame **1962,** *6*, 137-145.

41. Hurt R. H.; Haynes B. S., Proceedings of the Combustion Institute **2005,** *30*, 2157-2164.

42. Neoh K. G., Soot Burnout In Flames Thesis Sc.D., MIT **1981.**

43. Neoh K. G.; Howard J. B.; Sarofim A. F., Proceedings of the Combustion Institute **1985,** *20*, 951-957.

44. Neoh K. G.; Howard J. B.; Sarofim A. F., Particulate Carbon: Formation During Combustion, Plenum: New York, **1981,** 261-277.

45. Song; Juhun; Alam; Mahabubul; Boehman; André L.; Impact Of Alternative Fuels On Soot Properties And Dpf Regeneration. Combustion Science and Technology **2007,** *179*, 9, 1991 — 2037.

46. Agafonov G. L.; Smirnov V. N.; Vlasov P. A.; Shock Tube And Modeling Study Of Soot Formation During The Pyrolysis And Oxidation Of A Number Of Aliphatic And Aromatic Hydrocarbons. Preceding of the Combustion Institute **2011,** *33*, 625-632.

47. Oubal M., A New Semi-Empirical Model For The Oxidation Of Polycyclic Aromatic Hydrocarbon (PAHs) Molecules Physisorbed On Soot, Application To The Reaction PAH + OH For A Series Of Large PAH Molecules. Theoretical Chemistry Of Atmospheric Processes **2011,** 259-267.

48. Raj A.; Peter L. W.; Totton T. S.; Sander M.; Shirley A.; Kraft M., New Polycyclic Aromatic Hydrocarbon (PAH) Surface Processes To Improve The Model Prediction Of The Composition Of Combustion-Generated PAHs And Soot. Carbon **2010,** *48*, 2, 319-332.

49. Raj A., Structural Effects On The Oxidation Of Soot Particles By O_2: Experimental And Theoretical Study. Combustion and Flame **2013,** *160*, 9, 1812-1826.

50. Cheng X.; Chen L.; Yan F.; Dong S., Study On Soot Formation Characteristics In The Diesel Combustion Process Based On An Improved Detailed Soot Model. Energy Conversion And Management **2013,** *75*, 1-10.

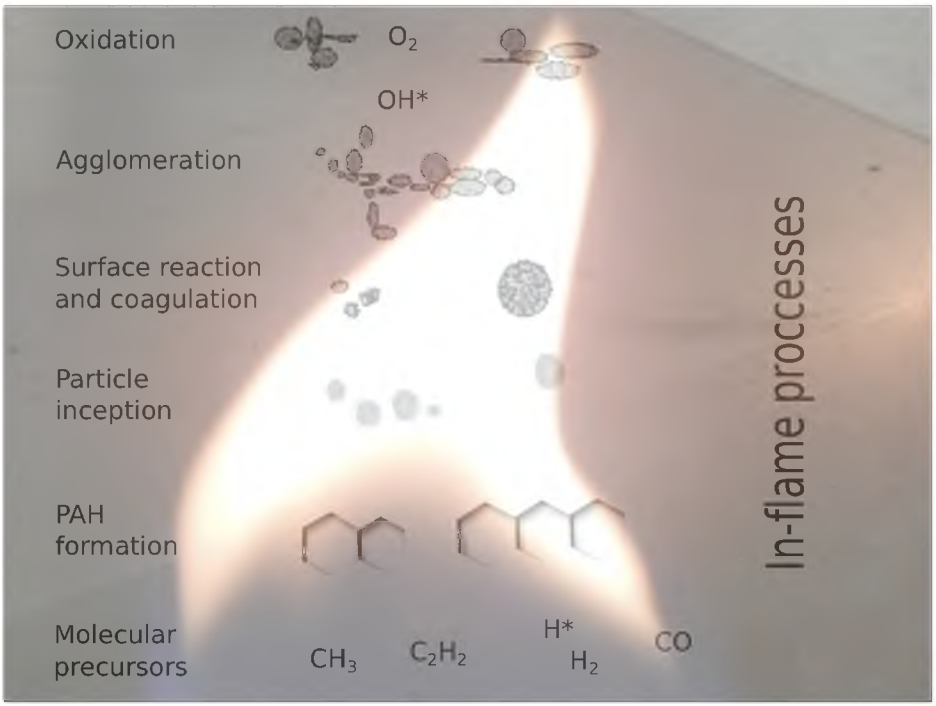

Figure 2.1 Schematic representation of the widely accepted reaction path that leads to soot formation.

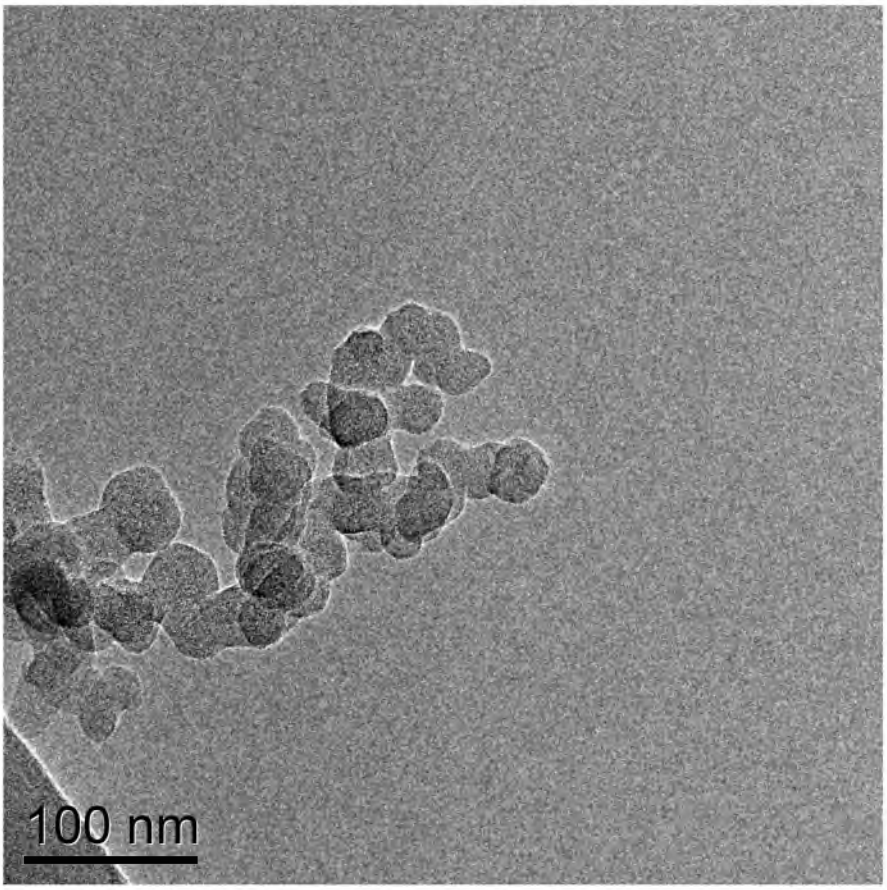

Figure 2.2 Spherical soot aggregates formed in a premixed flat-flame burner using *m*-xylene/*n*-dodoecane surrogate fuel, collected 5 cm above the surface of the burner on a TEM lacey carbon grid.

CHAPTER 3

EXPERIMENTAL APROACH

3.1 Surrogate Fuels and Model Carbons

Jet fuels, diesel fuels, and oxygenated fuels are composed of a multitude of different molecular components, vary in molecular weight, and exhibit different structures that range from linear alkanes to complex aromatics (*40*). Fuel molecules are a complex combination of different structural groups. Fuels can also have significant variations in their chemical and physical properties from shipment to shipment due to inconsistencies in production. This creates challenges to well-controlled fundamental modeling and experimental studies that require a more definite chemical composition for reproducibility and tractability.

Mixtures used in these studies are referred to as physical and chemical surrogates. Physical surrogates are mixtures having similar physical properties (*i.e.,* density, viscosity, heat capacity, and thermal conductivity) to the jet, diesel or biodiesel fuels being studied. Chemical surrogates generally have the same chemical class composition, average molecular weight, and correct proportion of aromatics, naphthenes, and paraffins (*31*).

Model carbons were used to correlate nanostructure to oxidation kinetics. Carbon nanostructure refers to the degree of ordered atomic-level structure within the soot samples. Lamella length and tortuosity are primary parameters to quantify to what degree the nanostructure is organized. Fringe length is a measure of the physical extent of the atomic carbon layer planes as seen in the HRTEM images, and tortuosity is a measure of the curvature of the fringes (*16, 17, 18,19, 21*). These parameters describe the overall structure for the samples and can be related to the kinetic parameters. Figure 3.1 shows the model carbons M1300, R250 and the Onion-Like Carbon (OLC). M1300 is the least ordered nanostructure with short fringe length and a high tortuosity up to the OLC with a highly organized nanostructure.

3.1.1 Model Carbon and Diesel Soot Samples

Model carbons were chosen to show a range of nanostructure and surface area, this intrinsic information was then related to the kinetic parameters of the model carbons. The chosen model carbons are an amorphous least-structured Monarch 1300 (M1300), a more structured Regal 250 (R250), both from Cabot, and the highly structured onion-like carbon (OLC). A commercially-produced diesel soot sample was used for comparison with the model carbons. Carboxen 1000 was chosen as the reference soot for the surrogate fuel formulations, due to its well-known kinetic parameters and physical properties (*32*).

3.1.2 Surrogate Jet-Fuel Formulations

The jet-fuel surrogate is a mixture of 83 mol% *m*-xylene and 17 mol% *n*-dodecane that contains straight, branched, and cyclic aliphatic hydrocarbons, of which *n*-dodecane and *m*-xylene are important components [16, 17]. This surrogate has been used in similar studies [39]. The pure compounds, *m*-xylene, *n*-dodecane, *n*-butanol were also studied for comparison with the jet-fuel and oxygenated fuel surrogates.

3.1.3 Oxygenated Surrogate Fuels

A 40 mol% *n*-butanol and 60 mol% *n*-dodecane was chosen as an oxygenated surrogate fuel, discussed in Chapter 4. The oxygenated surrogate fuel formulation of 10, 20, 30, 40, and 60 mol% *n*-butanol and remainder *n*-dodecane were chosen to investigate the effect of adding the oxygenated fuel on the oxidation kinetics, nanostructure and surface functional groups.

3.2 Premixed Flat Flame Burner, Soot Generation, Collection and Preparation

All surrogate soot samples were created by a premixed, flat-flame burner and captured on a water-cooled stabilization plate that was placed 5 cm above the surface of the burner, shown in Figure 3.2. Soot collected on the stabilization plate was crushed into a powder using a mortar and pestle and placed into airtight metal containers prior to being used in TGA experiments. Soot used for XPS analysis was collected from the stabilization plate, crushed using a glass stirrer and a glass vial, then placed in a nitrogen filled glass vials, care was taken not to contaminate the samples.

The experimental conditions used to produce the soot are displayed in Table 3.1. The equivalence ratio (Φ) is the actual fuel/oxidant ratio normalized by the stoichiometric fuel/oxidant ratio:

$$\Phi = \frac{(Fuel/Oxidant)_{actual}}{(Fuel/Oxidant)_{stoichiometric}} \quad (3.1)$$

Fuel-lean flames have an equivalence ratio less than 1 and fuel-rich flames have an equivalence ratio greater than 1. Heavily sooting flames used in this study required an equivalence ratio of about 2.

The burner consists of a stainless steel chamber (2 inches ID, Schedule 80, 5 inches long) with a bundle of tubes (1/16 inches ID, 1 ¼ inches long) used for flame stabilization and a nitrogen shroud, which shields the flame to minimize atmospheric interference. Liquid mixtures were fed to the burner using a temperature controlled vaporizer and manifold system designed in house.

3.2.1 Temperature Measurement

Flame temperatures profiles were measured at the centerline of the premixed flame using an uncoated type-B thermocouple (wire diameter = 0.002032 cm). The thermocouple was inserted into the flame 5 cm above the surface of the burner. For each measurement, the transient response of the thermocouple was recorded at a sampling rate of 50 samples per second for 25 seconds. When a thermocouple is inserted into a sooting flame, soot is driven to the thermocouple surface due to the thermophoretic gradient between the flame environment and the cold thermocouple surface. As the soot is deposited on the surface the temperature reading drops continuously. A correlation of the transient response rate, due to the soot deposition, was used to estimate the local gas

temperature. Temperature corrections were applied using the methodology developed by Rosner et al.). The temperature of the gases (T_g) is estimated using a quasisteady energy balance at the junction between the depositing soot and the thermocouple as follows:

$$\varepsilon_j \sigma T_j^4 = \frac{k_{g0} Nu_j}{2d_j}\left(T_g^2 T_j^2\right) \tag{3.2}$$

where T_j is the junction temperature, ε_j is the junction/bead emissivity, σ is the Stefan-Boltzmann constant, Nu_j is the junction Nusselt number, d_j is the junction diameter, and k_{g0} is the gas thermal conductivity. T_j can be estimated from the response curve of the thermocouple by extrapolating the temperature at $t = 0$ seconds. The emissivity of type-B thermocouples can be estimated as a function of the temperature shown below:

$$\varepsilon = 0.1083 \ln(T_j) - 0.5644 \tag{3.3}$$

The Nusselt number has been evaluated for similar systems in the range from 2.26 to 2.35. k_{g0} is assumed constant, which is reasonable for combustion gases at high temperature. The error in temperatures due to soot deposition-imposed changes in the junction diameter and emissivity were calculated to be less than 60 K for the gas temperature range of 1550-1900 K (*18*).

3.3 High-Pressure Thermogravimetric Analyzer (High-Pressure TGA)

The Cahn Thermax 500 high-pressure thermogravimetric analyzer (TGA) was used for all experiments requiring pressure and the majority of the experiments at atmospheric conditions. The TGA records the weight change of a sample over time with a reading taken every second. Figure 3.3 is an image of the TGA system. Ten mg of soot was placed in a cylindrical quartz crucible (18 mm diameter and 20 mm height) along with inert silicon carbide beads that were used in all of the experiments to help minimize

diffusional effects by decreasing the stagnant atmosphere between the surface of the soot and the entrance of the container. The crucible is suspended from a ceramic coil attached to a microbalance, and the furnace and balance were purged for 15 minutes with both nitrogen and helium prior to each experiment. Isothermal tests were performed at varying temperatures from 400 to 800°C, a heating rate of 10°C/min was used to reach the oxidation temperature under a controlled gas environment during which helium was used to drive off volatiles contained in the soot. Nitrogen flowed at 0.55 L/min through the microbalance to protect the microbalance from exhaust gases released during oxidation of the soot samples. The oxidizer used was a mixture of 5, 10, or 21% oxygen in nitrogen with a flow rate of 1.0 L/min.

3.3.1 Optimization of High-Pressure TGA Variables

Working with the high-pressure TGA requires the optimization of sample size, amount of inert material added, and oxidizer flow rate, which reduces the mass-transfer limitations and improves the reproducibility of the experiments. Figure 3.4 shows the mass-based oxidation rates were less than 10% for two separate experiments at 600°C, 10 mg sample and 1.0 L/min of 21% oxygen in nitrogen, showing the quality and reproducibility of the data.

In order to find the optimal sample mass, a temperature of 600°C and a constant flow rate for the oxidizer of 1.0 L/min was chosen, while varying the sample mass from 5 to 30 mg. Figure 3.5 shows the results of the mass-based oxidation rates. The rates were very similar for loading masses of 10 and 20 mg and small differences are likely attributable to experimental error. A sample mass of 5 mg was discarded due to the rapid

oxidation of the sample, which produced small data sets and unreliable results. The mass-based oxidation rate for a 30 mg sample was slower than experiments at lower initial sample mass.

This is demonstrated by the slope in the graph, and resulted in incomplete burnout, indicating that mass-transfer resistances are present in the oxidation of the 30 mg sample. An initial loading mass of 10 mg was chosen as the optimum mass for the remaining experiments because it displayed a consistent oxidation rate (k_s).

The oxidizer flow rate was varied between 0.50, 0.75 and 1.0 L/min and the mass-based oxidation rates are shown in Figure 3.6. The rates do not have significant differences for the 0.75 L/min and the 1.0 L/min but the rate was decreased for the 0.5 L/min flow, indicating possible oxygen diffusion limitations. The 1.0 L/min flow rate was chosen for the remainder of experiments, because it had the highest and most consistent rate.

3.4 Q600 TGA

A Q600 thermogravimetric analyzer (TGA) was used to oxidize the soot samples in a quartz crucible under isothermal and atmospheric conditions. The Q600 was used for experiments in Chapters 5 and 6. During a 10^{o}C/min heating period, a flow of 500 mL/min of nitrogen was used to drive off volatiles present in the soot samples. Once the target temperature was reached and stabilized for 5 minutes, the oxidizer gas (air) was switched on at the same 500 mL/min while nitrogen was switched off. Time, temperature and mass data were recorded every 0.5 seconds. The Q600 was used for several reasons,

ease of operation, when pressurized runs are not required, quicker run time when compared to the high-pressure TGA and small sample mass.

3.4.1 Optimization of Q600 TGA Variables

These are the preliminary experiments used for the optimization of the TGA variables for the work conducted in Chapter 5. First the oxidizer flow rates and sample mass are to be optimized before the kinetic factors can be properly determined. The interaction of the oxidizer and the soot can be affected by the gas flow rate and sample mass, leading to mass-transfer limitations (*12*). The availability of oxygen is critical for the oxidation of the model carbons and soot and the oxidation efficiency may be lowered due to a lack of sufficient oxygen. Oxidation in the furnace can be partially diffusion limited (*4, 12, 13, 14*), but is optimal when the reaction is primarily kinetically controlled (*4*). Kinetically controlled reactions provide the best representation of the kinetic rate constant, activation energy and pre-exponential factor, due to less calculation errors and slowing of the reaction rate. If oxidation is not mainly a kinetically controlled reaction, then a more complicated combination of diffusive and kinetic models is necessary (*12, 13*). A series of experiments were performed to find the most favorable conditions to ensure quality estimations of the kinetic parameters.

The combustion of a 5 mg sample of M1300 at 650°C and flow rates ranging from 100 to 500 mL/min in increments of 100 mL/min were used to estimate the rate of conversion for the different oxidizer flow rates. Conversion of the sample is defined as $\alpha = 1 - \left(\frac{m}{m_o}\right)$. As shown in Figure 3.7, the oxidation rate of 100 mL/min is the slowest, next are the 200 and 300 mL/min and the fastest oxidation rates are the 400 and 500

mL/min, which are nearly identical. The flow rate of 500 mL/min for air was chosen to minimize oxygen diffusional limitations.

A large initial mass may be associated with diffusional limitations, (*4, 9*) as it may cause self-heating (exothermic) and self-cooling (endothermic) reactions, producing a large deviation from the desired heating rate. A small initial mass may result in increased uncertainty along with low reproducibility (*13*) due to the development of a temperature gradient, which could be created as a result of the low thermal conductivity of the samples. Investigation of the effect on conversion by the initial mass loading was carried out on all model carbons. A range of initial mass loading was used for each sample, holding the temperature and oxidizer flow rate constant at 600^{o}C and 500 mL/min, respectively, to identify the impact on soot oxidation.

Varying M1300 initial masses from 2-10 milligrams, OLC and R250 masses from 5-16 milligrams to find the optimal initial mass to be used in the remaining experiments. Figure 3.8 is the mass-based oxidation profiles for M1300. The low initial mass quickly oxidized, while the large initial mass oxidized much more slowly, which may be due to mass-transfer resistances; therefore the 5 mg sample was chosen. Similar analysis led the determination of an 8 mg sample for R250 and a 10 mg sample for OLC.

3.5 Estimation of Kinetic Parameters

The TGA mass-loss curves were obtained under isothermal conditions and used to determine the soot-oxidation kinetic parameters. To determine the kinetic parameters, a simplified rate expression for soot oxidation is developed. The following expression is a

mass rate law for soot oxidation by oxygen, which describes the loss of mass of the soot as it reacts with oxygen:

$$\frac{dm}{dt} = -k_c m_c {p_{O_2}}^n \tag{3.4}$$

where m_c is the initial mass of soot, k_c is the reaction rate constant, p_{O_2} is the partial pressure of oxygen, n is the reaction order of oxygen and t is time. Integrating the differential mass balance, using an initial boundary condition that at $t = t_o$, $m_c = m_{co}$, m_{co} is the initial mass of the soot at time equals zero, yields Equation 3.5.

$$\frac{m_c}{m_{co}} = exp\left(-k_c {p_{O_2}}^n (t - t_0)\right) \tag{3.5}$$

In order to solve Equation 3.5, we first assume that the reaction rate constant follows an Arrhenius model as shown in Equation 3.6:

$$k_c = A\ exp\left(\frac{E_a}{RT}\right) \tag{3.6}$$

where A is the pre-exponential factor, E_a is the activation energy of the reaction, R is the universal gas constant, and T is the temperature of the system. Next, the reaction order of oxygen was determined by performing TGA experiments on the jet-fuel surrogate soot and the Carboxen 1000 samples. The experiments varied the oxygen concentration between 5, 10, and 21 % in nitrogen. The temperature and pressure were held constant at 600°C and 1 atm, respectively. Plotting the natural log of oxygen concentration against the natural log of k_c and using the resulting slope of the line is an estimation of n, shown by Equation 3.7.

$$ln(p_{O_2}) = n\ ln\ (-k_c) \tag{3.7}$$

The estimated reaction order for oxygen was determined to be 0.90 for the jet-fuel surrogate and 0.92 for the Carboxen 1000. This is validation that the reaction order for the jet-fuel surrogate and the Carboxen 1000 can be estimated as unity.

The reaction order determined from our fits varied widely and was difficult to interpret. The bulk of the studies in our temperature ranges have reported the reaction order of oxygen to be unity (*33, 34, 35, 36, 12*) and, due to simplicity and our limited data, n was assumed to be unity for subsequent modeling steps. Rearranging Equations 3.5-3.7 and assuming $n = 1$ yields:

$$ln\left(-\frac{d\left(\frac{m}{m_c}\right)}{dt}\right) = ln\left(Ap_{O_2}\right) - \left(\frac{E_a}{RT}\right) \quad (3.8)$$

By plotting the natural log of the kinetic rate against the inverse of temperature, the activation energy and pre-exponential factor can be determined. The slope of this line is the used to calculate the activation energy by multiplying by the universal gas constant. The pre-exponential factor can be calculated from the intercept. Figure 3.9 shows a plot of the kinetic rates of five isothermal experiments plotted against the inverse of temperature.

Kinetic models are useful tools for the evaluation and comparison of kinetic parameters associated with the oxidation of soot. Differential and graphical methods are widely used for kinetic analysis in the calculation of reaction rates. In thermogravimetric experiments, the main source of error is hidden in the measurement of mass. Methods used to minimize errors in these calculations are optimization of the experimental operation variables, discussed previously, and use of data obtained between 20 to 60% mass loss for the samples. This computational method yields an error of ±0.5% for the

derivative of Equation 3.4 and leads to the error in activation energy of ±2-6 kJ mol^{-1} (*41, 42*).

3.6 Estimation of Kinetic Parameters at Elevated Pressures

3.6.1 Diffusional Limitations of Soot Oxidation

Combustion of a soot particle may be influenced by concentration gradients of oxygen created due to diffusion processes (*6, 13, 14*), resulting in a decreased overall rate of oxidation (*14, 23*). Oxygen diffusion may be explained by three different mechanisms to reach the active surface of the soot: diffusion of oxygen within a soot particle, diffusion of oxygen to the soot particles, and diffusion of oxygen between the soot particles, (*13, 14, 19*) as shown in Figure 3.10. A model was developed to account for these with the following assumptions: no temperature gradients in the sample layer; one-dimensional mass transfer diffusion from the bulk flow to the surface of the sample layer; and an irreversible, first-order reaction.

3.6.2 Diffusion of Oxygen Within the Soot Particle (Intraparticle Diffusion)

Porous soot particles allow for the diffusion of gaseous oxygen into the interior of the particle. Oxygen concentration within the particle is nonuniform and decreases from the outer part to the inner part, along the varied microchannels within the soot particle. The source term, or total rate of oxygen consumption within a particle due to the carbon-oxygen reaction accounting for diffusional limitations, can be expressed as (*23*):

$$r'_{O_{2,p}} = \frac{\beta k_s \rho_b p_{O_2}}{M_c} \tag{3.9}$$

β is the ratio of stoichiometric coefficients (mol oxygen/ mol carbon), k_s is the intrinsic rate constant, M_c is the molecular weight of carbon, and $p_{O_2,}$ is the partial pressure of oxygen and ρ_b is the particle density. This rate expression is applied to a differential annular shell in a spherical particle, and is now used as a source term in the mass balance equation of oxygen species.

$$\mathrm{r'}_{O_{2,p|CV}} = \mathrm{r}_{O_{2,p}} dV = \frac{\beta k_s \rho_{b,p} p_{O_2} (4\pi r^2 dr)}{M_c} = \frac{\beta k_s \rho_{b,p} p_{O_2} R_u T C_{O_2} (4\pi r^2 dr)}{M_c} \quad (3.10)$$

Using a mass balance on the differential annular shell in the spherical soot particle to describe the change in oxygen concentration, Equation 3.10 can be formulated in terms of oxygen concentrations; this is accomplished by balancing the molar oxygen flux and the source terms in a spherical coordinates.

$$\frac{1}{r^2}\frac{d}{dr}\left(r^2 \frac{dC_{O_2}}{dr}\right) = \frac{\beta k_s \rho_{b,p} RT C_{O_2}}{D_{eff,p} M_c} \quad (3.11)$$

The Thiele diffusion modulus inside the particle, or particle modulus, is shown by Equation 3.12:

$$\emptyset_p = r_p \sqrt{\frac{\beta k_s \rho_{b,p} RT}{M_c D_{eff,p}}} \quad (3.12)$$

where r_p is the radius of the particle, $\rho_{b,p}$ is the bulk density of a particle, M_c is the molecular weight of carbon, and $D_{eff,p}$ is the effective diffusion coefficient inside the particle.

The diffusion occurs in the internal pore channels and, since the pore diameter of carbon particles are typically on the order of nanometers, internal diffusion can be related to Knudsen diffusion (*23, 24*). The effective diffusion coefficient is:

$$\mathrm{D}_{eff,p} = \frac{8\varphi_p{}^2}{3\tau_p S_g \rho_{b,p}} \sqrt{\frac{2RT}{\pi M_c}} \quad (3.13)$$

where φ_p is the porosity inside the particle, τ_p is the tortuosity in the particles. Table 3.2 lists the values and sources for these variables.

An effectiveness factor, η_p, is introduced as a correction of the oxygen reaction rate to account for the diffusional resistance to soot oxidation within the nanoparticle and varies from zero to one. The effectiveness factors (η) are related to the Thiele modulus and will be described over the following sections. η_p is calculated using Equation 3.14.

$$n_p = \frac{3}{\emptyset_p}\left[\frac{1}{\tanh \emptyset_p} - \frac{1}{\emptyset_p}\right] \tag{3.14}$$

3.6.3 Diffusion of Oxygen Between the Soot Particles (Interparticle Diffusion)

The soot sample layer in the TGA crucible can be modeled as a one-dimensional porous flat plate (*13, 14*). Oxygen diffuses through the void space between particles, commonly referred to as porosity, to the surface of each particle. Equation 3.15 represents a mass balance of oxygen at any position inside the sample layer (*23*):

$$\frac{D_{eff,1}}{RT}\frac{d^2 p_{O_{2,x}}}{dx^2} = \frac{\beta k_s{}' \rho_{b,1} p_{O_{2,x}}}{M_c} \tag{3.15}$$

where $D_{eff,1}$ is the effective diffusion coefficient between sample particles, x is the distance from the bottom of the crucible plus inert to a point inside a particle layer, $p_{O_{2,x}}$ is the local partial oxygen pressure , $\rho_{b,1}$ is the bulk density of the soot sample layer , and $k_s{}'$ is the effective reaction rate constant (s/m). Because the average diameter of the pore is on the order of micrometers, the diffusion between particles is related to molecular diffusion (*13, 23*) as follows:

$$D_{eff,1} = D_e \frac{\varphi_1}{\tau_1} \tag{3.16}$$

where D_e is the external molecular diffusion coefficient [23], τ_1 is the tortuosity between particles [13, 26], and φ_1 is the porosity between particles. Again, these values are presented in Table 3.2. From Equations 3.17 and 3.18, the Thiele diffusion modulus between particles $\emptyset_1$ (or particle layer modulus) and the effectiveness factor for diffusion to the particle layer η_1 are

$$\emptyset_1 = e\sqrt{\frac{\beta \eta_p k_s S_g \rho_{b,1} RT}{M_c D_{eff,1}}} \tag{3.17}$$

where e is the thickness of the particle layer.

$$\eta_1 = \frac{\tanh \emptyset_1}{\emptyset_1} \tag{3.18}$$

Therefore, we can represent the overall total oxygen consumption rate of a particle layer as a combination of oxygen diffusion within the particles and diffusion between particles, combining Equations 3.9-3.18 yields a reaction rate expression:

$$r'_{O_{2,1}} = \frac{\eta_p \eta_1 \beta k_s \rho_{b,1} A_s e p_{O_{2,s}}}{M_c} \tag{3.19}$$

where A_s is the transaction area of the crucible, and $p_{O_{2,s}}$ is the partial pressure of oxygen at the surface of the particle layer.

3.6.4 Diffusion of Oxygen to the Soot Particle (Bulk Diffusion)

In the TGA experiments, there are differences in the oxygen partial pressure between the crucible inlet and the surface of the particle layer (*27*) due to the oxygen consumption by the particle layer. Oxygen diffuses from the ambient bulk flow to the surface of the particle layer, which occurs on a millimeter scale. The oxygen transfer rate or flux ($\dot{N}$) above the surface of the particle bed is related to an analytical solution of the Stefan problem (*28*). In this case, the oxygen transfer rate above the particle layer can be

estimated as one-dimensional molecular diffusion and the oxygen transfer rate or flux can be expressed as

$$\dot{N} = r'_{O_{2,1}} \tag{3.20}$$

$$r'_{O_2} = \frac{A_S D_e}{R_u T} \frac{p_{O_{2,0}} - p_{O_{2,s}}}{L - e} = \frac{\eta_p \eta_1 \beta k_s S_g \rho_{b,1} A_s e p_{O_{2,s}}}{M_c} \tag{3.21}$$

where $p_{O_{2,0}}$ is the oxygen partial pressure of bulk flow and L is the height of crucible minus the height of inert (*23, 28*). Equation 3.21 is used to estimate the influence of external diffusion effectiveness factor (η_e)

$$\frac{1-\eta_e}{\eta_e} = \frac{\eta_p \eta_1 \beta k_s S_g \rho_{b,1} RTe(L-e)}{D_e M_c} \tag{3.22}$$

The molecular diffusion coefficient $D_e = D_{AB}$ is estimated based on the kinetic theory and the Lennard-Jones expression for intermolecular forces

$$D_e = D_{AB} = \frac{0.0018583 T^{3/2} \left(\frac{1}{M_A} + \frac{1}{M_B}\right)^{1/2}}{P_t \sigma^2_{AB} \Omega_{AB}} \tag{3.23}$$

where D_{AB} is bulk diffusivity between two components in a mixture, P_t is the total pressure of the gas , Ω_{AB} is the collision integral, σ_{AB} is the force constant in the Lennard-Jones potential function, M_A and M_B are the molecular weights of oxygen and nitrogen, respectively (*23*). Thus, the actual total oxygen consumption rate in the particle layer combining all three oxygen diffusion processes can be expressed as

$$r'_{O_{2,1}} = \frac{\eta_p \eta_1 \eta_e \beta k_s S_g \rho_{b,1} A_s e p_{O_{2,s}}}{M_c} \tag{3.24}$$

The computational procedure to calculate the kinetic parameters taking into account the diffusional resistances is as follows:

(1) On the basis of equation 3.6, calculate k_s from the original thermogravimetric data, draw an Arrhenius curve of the natural log of k_s versus 1 over temperature in Kelvin, and correlate kinetic parameters A and E based on equation 3.8.

(2) Calculate effectiveness factors η_p and η_1 and η_e based on equations 3.14, 3.18 and 3.21.

(3) Using equation 3.24, calculate k_s again, create a new Arrhenius curve natural log of k_s versus 1 over temperature in Kelvin, and correlate kinetic parameters A and E based on equation 3.8.

(4) Compare the new kinetic parameters with previous ones, if they similar stop the calculation, if not, go to step 2 and repeat the calculation with the new kinetic parameters.

3.7 X-ray Photoelectron Spectroscopy (XPS)

X-Ray photoelectron spectroscopy (XPS) was used to identify elemental specification and the surface chemistry characterization of soot samples. XPS analysis can identify oxygen groups by bond type as well as the varying proportion of sp^2, sp^3, and fullerenic carbon entities present that help to identify carbon to hydrogen bonding. Carbonyl, carboxylic and phenol oxygen bonding groups, commonly found in carbonaceous material, are also identified. Using the data collected during the XPS analysis we are able to extract the carbon to oxygen (C/O) and the carbon to hydrogen (C/H) ratios.

X-Rays of a known energy (hv) are used to eject core shell electrons from the atom, a photoelectron can be emitted through the photoelectric effect, shown in Figure

3.11. The kinetic energy of the emitted electron is (E_k) and can be measured. Then the atomic core level binding energy E_b relative to the Fermi level E_f of the sample can be determined using the following equation:

$$E_b = h\nu - E_k - \phi_{sp} \tag{3.22}$$

where ϕ_{sp} is the work function of the spectrometer, 4.3 eV for our experiments. This energy is specific to the quantum shell that is influenced by the local electron density, which is that of the element. The binding energy of a core-shell electron is influenced by the valence shell bonding arrangement, this is related to outer electron orbital hybridization and associated bonding to the adjacent atoms. This allows XPS to identify surface functional groups and the elemental bonding states (*3*).

A Kratos Axis Ultra DLD was used to collect all XPS spectra. The ASTM Designation E1078-09 guide was used in the preparation of the samples for use in the XPS instrument (*38*). Core level photoelectrons were excited using monochromatic Al K alpha radiation (1486.6 eV). All survey spectra were collected using pass energy of 160 eV, with hi-resolution regional spectra collected at 40 eV pass energy. Charging was corrected by using a low energy electron flood gun, and by referencing adventitious carbon at 284.5 eV and correcting spectra accordingly.

The resultant scans over the C1s region were curve fitted using Gauss-Lorenz peaks and a Shirley fit to give the best and most accurate results. CasaXPS software was used for the initial peak fitting. The peak analysis and visualization was conducted using Excel.

3.8 High-Resolution Transmission Electron Microscope (HRTEM)

In order to investigate the soot nanostructure, a 200-kV field emission HRTEM (JEOL EM-2010F) was used to take high-resolution bright field images. Soot nanostructure for this study is described as a combination of fringe length and tortuosity. Fringe length is a measure of the physical extent of the atomic carbon layer planes as seen in the HRTEM images, and the tortuosity is a measure of the curvature of the fringes (*16, 17, 18,19, 21*). These parameters describe the overall structure for the samples and can be related to the kinetic parameters represented in Figure 3.12. When visually comparing structure, a decrease in the fringe length and an increase in tortuosity relates to the structure becoming less organized and, conversely, if there is an increase in fringe length and a decrease in tortuosity, then this can be related to more organized, more structured flatter soot.

3.9 References

1. Clague A. D. H.; Donnet J. B.; Wang T. K.; Peng J. C. M., A Comparison Of Diesel Engine Soot With Carbon Black. Carbon **1999,** *37*, 10, 1553-1565.

2. Miller F. J.; Gardner J. A.; Graham R. E.; Lee W. E., Size Considerations For Establishing A Standard For Inhalable Particles. Journal of the Air Pollution Control Association **1979,** *29*, 6, 610-615.

3. Stanmore B. R.; Brilhac P.; Gilot P., The Oxidation Of Soot: A Review Of Experiments, Mechanism And Models. Carbon **2001,** *39*, 15, 2247-2268.

4. Stratakis G. A.; Stamatelos A. M., Thermogravimetric Analysis Of Soot Emitted By A Modern Diesel Engine Run On Catalyst-Doped Fuel. Combustion and Flame **2003,** *132*, 157-169.

5. Song J.; Alam, M.; Boehman A. L.; Kim U., Examination of the Oxidation Behavior of Biodiesel soot. Combustion and Flame **2006,** *146*, 4, 589-604.

6. Stanmore B. R.; Gilot P.; Prado G., The Influence Of Mass Transfer In DTG Combustion Tests. Thermochimica Acta **1994,** *240*, 1, 79-89.
7. Gilot P.; Brillard A.; Stanmore B. R., Geometric Effects On Mass Transfer During Thermogravimetric Analysis: Application To Reactivity Of Diesel Soot. Combustion and Flame **1995,** *102*, 471-480.

8. Zouaoui N.; Brilhac J.; Mechati F.; Jeguirim M.; Djellouli B.; Gilot P., Study Of Experimental And Theoretical Procedures When Using Thermogravimetric Analysis To Determine Kinetic Parameters Of Carbon Black Oxidation. Journal of Thermal Analysis & Calorimetry **2010,** *102*, 837-849.

9. Kalogirou M.; Samaras Z., A Thermogravimetric Kinetic Study Of Uncatalized Diesel Soot Oxidation. Journal of Thermal Analysis & Calorimetry **2009,** *98*, 215-224.

10. Kalogirou M.; Samaras Z., Soot Oxidation Kinetics From TG Experiements. Journal of Thermal Analysis & Calorimetry **2010,** *99*, 1005-1010.

11. Rodriguez-Fernandez J.; Oliva F.; Vazquez R. A., Characterization of the diesel soot oxidation precess through an optimized thermogravimetric method. Energy & Fuels **2011,** *25*, 2039-2039.

12. Gilot P.; Bonnefoy F.; Marcuccilli F.; Prado G., Determination Of Kinetic Data For Soot Oxidation. Modeling The Competition Between Oxygen Diffusion And Reaction During Thermogravimetric Analysis. Combustion and Flame **1993,** *95*, 87-100.

13. Song J.; Chung-Hwan J.; Boehman A., Impacts Of Oxygen Diffusion On The Combustion Rate Of In-Bed Soot Particles. Energy & Fuels **2010,** *24*, 2418-2428.

14. Song Q.; He B.; Yao Q.; Meng Z.; Che C., Influence Of Diffusion On Thermogravimetric Analysis Of Carbon Black Oxidation. Energy & Fuels **2006,** *20*, 1895-1900.

15. Ranzi E., A Wide-Range Kinetic Modeling Study Of Oxidation And Combustion Of Transportation Fuels And Surrogate Mixtures. Energy & Fuels **2006,** *20*, 1024-1032.

16. Edwards T., Liquid Fuels And Propellants For Aerospace Propulsion. Journal of Propulsion and Power **2003,** *19*, 1089-1107.

17. Westbrook C. K.; Pitz W. J., Motor Fuels: Energy Efficiency and Emissions in Transportation. Energy **2002.**

18. McEnally C. S.; Koylu U. O.; Pfefferle L. D.; Rosner D. E., Soot Volume Fraction And Temperature Measurements In Laminar Non-Premixed Flames Using Thermocouples. Combustion and Flame **1997,** *109*, 701-720.

19. Ciambelli P.; Corbo P.; Gambino M.; Palma V.; Vaccaro S., Catalytic Combustion Of Carbon Particulate. Catalysis Today **1996,** *27*, 99-106.

20. Otto K.; Sieg M. H.; Zinbo M.; Baartosiewz L., The Oxidation Of Soot Deposits From Diesel Engines, SAE **1981.**

21. Neeft J. P.; Nijhuis T. X.; Makkee M.; Moulijn J.A., Kinetics Of The Oxidation Of Diesel Soot. Fuel **1997,** *76*, 1129-1136.

22. Sorensen L. H.; Gjernes T.; Fjellerup J., Determination Of Reactivity Parameters Of Model Carbons, Cokes And Flame-Chars. Fuel **1996,** *75*, 31-38.

23. Satterfield C. N., Mass Transfer In Heterogeneous Catalysis; MIT Press: Cambridge, MA, **1970.**

24. Salvador S.; Commandre J. M.; Stanmore B. R., Reaction Rates For The Oxidation Of Highly Sulphurised Petroleum Cokes. Fuel **2003,** *82*, 715-720.

25. Incropera F. P.; Dewit D. P., Fundamental of Heat and Mass Transfer; Wiley & Sons: New York, **1970.**

26. Brilhac J. F.; Bensouda F.; Gilot P.; Brillard A.; Stanmore B., Experimental And Theoretical Study Of Oxigen Diffusion Within Packed Beds Of Carbon Black. Carbon **2000,** *38*, 1011-1019.

27. Turns A. R., An Introduction To Combustion: Concepts And Applications; McGraw Hill: Inc **1996.**

28. Bird R. B., Transport Phenomena; Wiley & Sons: New York, **1960.**

29. Hecker W. C.; Madsen P. M.; Sherman M. R.; Allen J. W.; Sawaya R. J.; Fletcher T. H., High Pressure Intrinsic Oxidation Kinetics Of Two Coal Chars. Energy & Fuels **2003**, *17*, 427-432.

30. Yehliu K.; Vander Wal R. L.; Boehman A. L., Combust. Flame **2011,** *158*, 1837-1851.

31. Edwards T., Surrogate Mixtures to Represent Complex Aviation and Rocket Fuels. Journal of Propulsion and Power **2001,** *17*, 122.

32. Sigma-Aldrich, High-Tech Carbons. Material Matters **2009,** 4.4, 110.

33. Marcucilli F.; Gilot P.; Stanmore B. R.; Prado G., Experimental And Theoretical Study Of Diesel Soot Reactivity. The Combustion Institute **1994,** 619–26.

34. Otto K.; Sieg M. H.; Zinbo M.; Bartosiewicz L., The Oxidation Of Soot Deposits From Diesel Engines. SAE **1981,** 800336.

35. Brilhac J. F., Bensouda F.; Gilot P.; Brillard A.; Stanmore B., Experimental And Theoretical Study Of Oxygen Diffusion Within Packed Beds Of Carbon Black. Carbon **2000,** *38*, 1011– 9.

36. Soete G., Catalysis Of Soot Combustion By Metal Oxides. The Combustion Institute **1988.**

37. CAHN Thermax 500 Operation Manuel.

38. ASTM International. "Standard Guide for Specimen Preparation and Mounting in Surface Analysis." ASTM International. West Conshohocken, PA: ASTM international **2011.**

39. Echavarria C.; Jaramillio I. C.; Sarofim A.; Lighty J., Burnout Of Soot Particles In A Two-Stage Burner With A JP-8 Surrogate Fuel. Combustion and Flame **2012,** *159*, 7.

40. Blanquart G.; Pepiot-Desjardins P.; Pitsch H., Chemical Mechanism For High Temperature Combustion Of Engine Relevant Fuels With Emphasis On Soot Precursors. Combustion and Flame **2009,** *156*, 588–607.

41. Mamleev V.; Bourbigot S.; Calculation Of Activation Energies Using The Sinusoidally Modulated Temperature. Journal of Thermal Analysis and Calorimetry **2002,** *70*, 565–579.

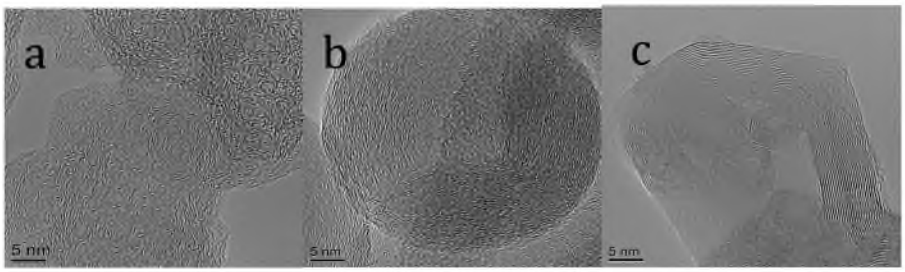

Figure 3.1 Showing the differences in structure, from the amorphous M1300 to the highly structured OLC. a) M1300 Model Carbon, b) R250 Model Carbon, c) OLC Model Carbon.

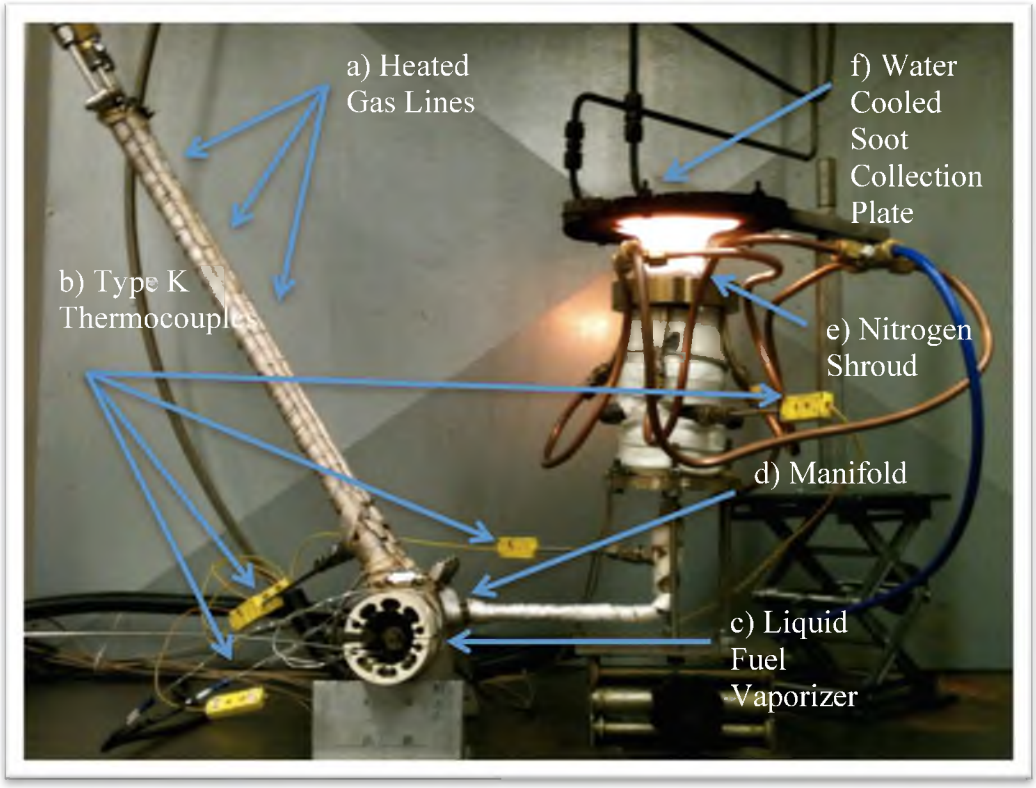

Figure 3.2 Representation of the flat-flame burner, manifold, and vaporizer system used to produce soot. a) Three inlet gas lines wrapped in heating tape and regulated with b) type K thermocouples. c) Liquid fuel vaporizer and heating system. d) Stainless steel manifold used to ensure proper mixing of the vaporized liquid fuel and gases. e) Nitrogen shroud used to protect the flame from ambient air. f) Water-cooled soot collection plate, placed 5 cm above the surface of the burner.

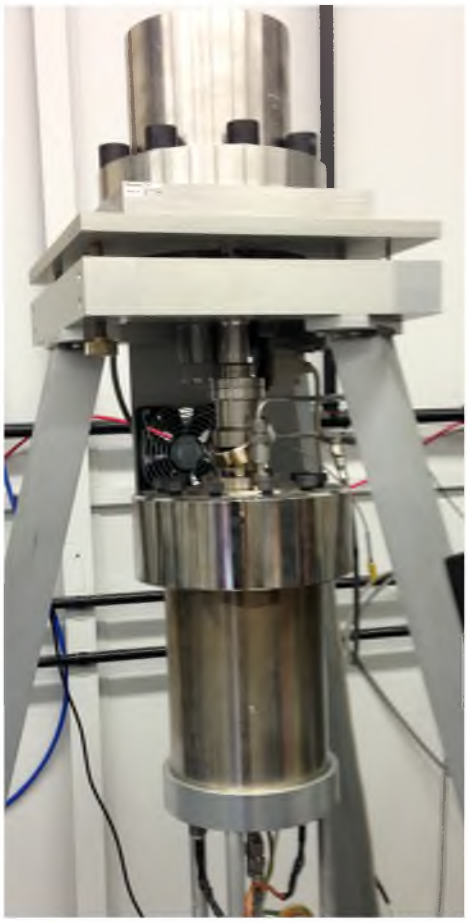

Figure 3.3 Image of the high-pressure thermogravimetric analyzer.

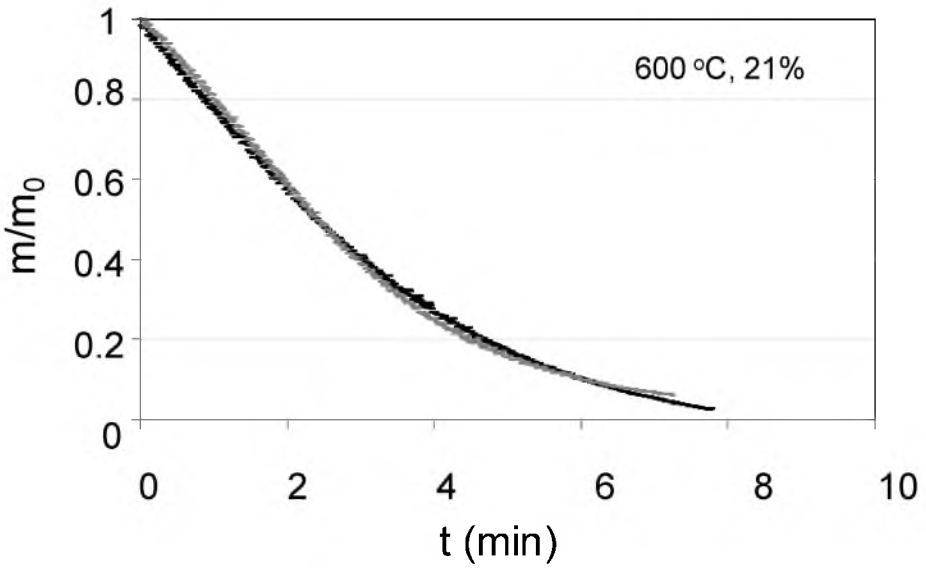

Figure 3.4 Reproducibility of the TGA experiments for surrogate soot sample with an initial mass of 10 mg.

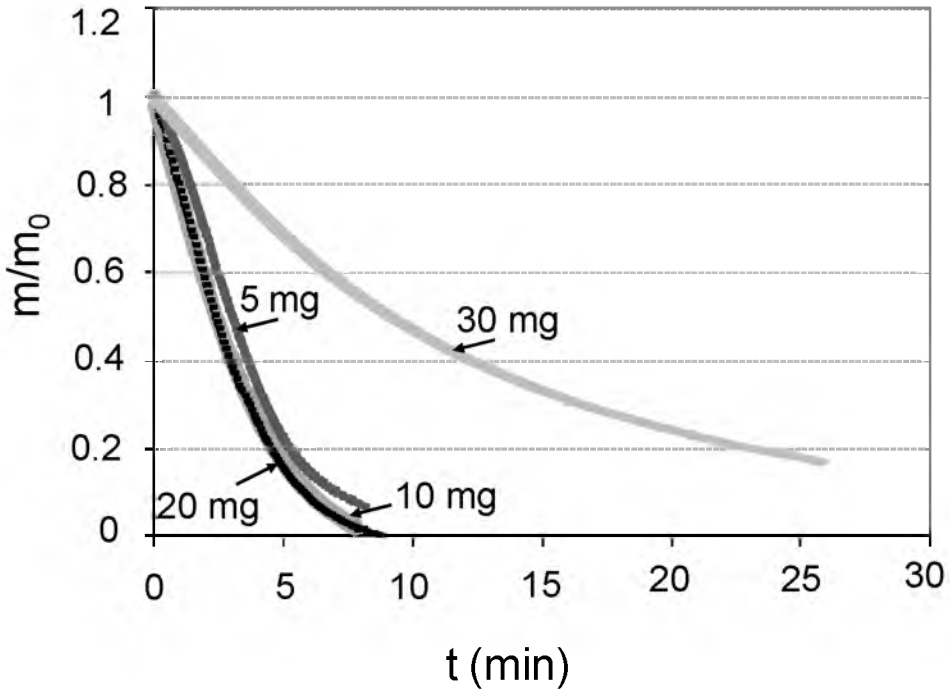

Figure 3.5 Effect of the initial mass loading for surrogate soot oxidized in air, normalized mass-loss plot, estimation of the oxidation kinetic rate derives from the slope of the line.

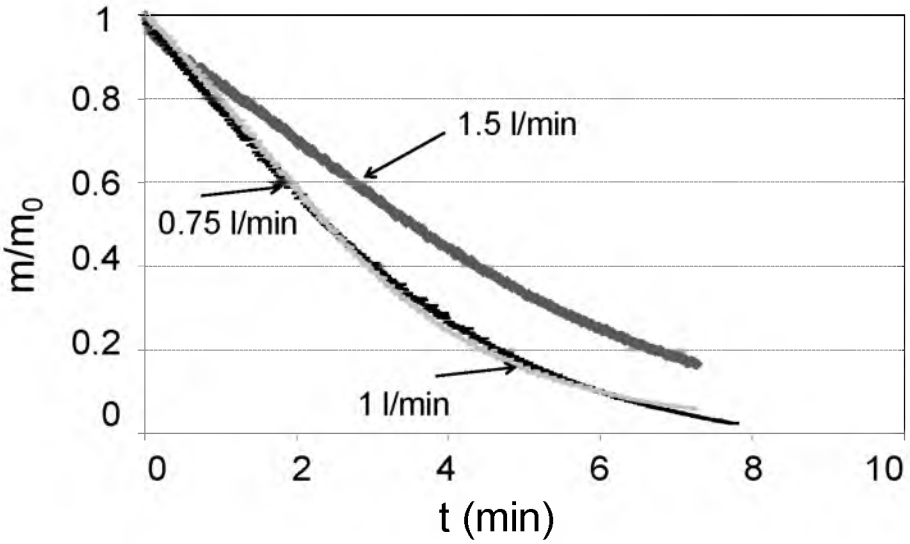

Figure 3.6 Effect of the oxidizer flow rate on the reaction rate for the surrogate soot sample oxidized in air. The 1.0 L/min flow rate was chosen for the remainder of the experiments.

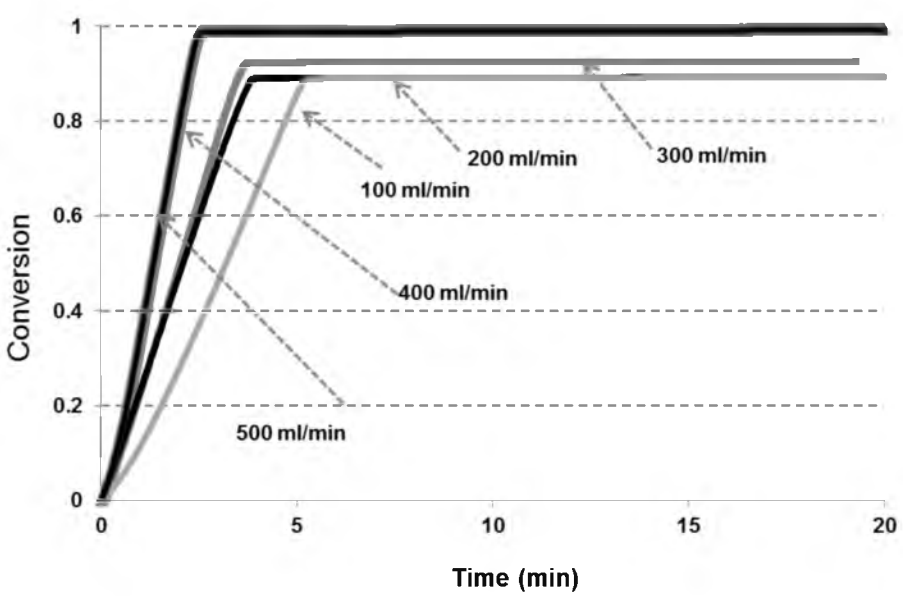

Figure 3.7 Isothermal conversion profiles for a 5 mg sample of M1300 for a range of oxidizer flow rates, ranging from 100 to 500 mL/min at a temperature of 650°C. The flow rate of 500 mL/min was chosen as the optimum oxidizer flow rate as the soot oxidation kinetic rate was the highest.

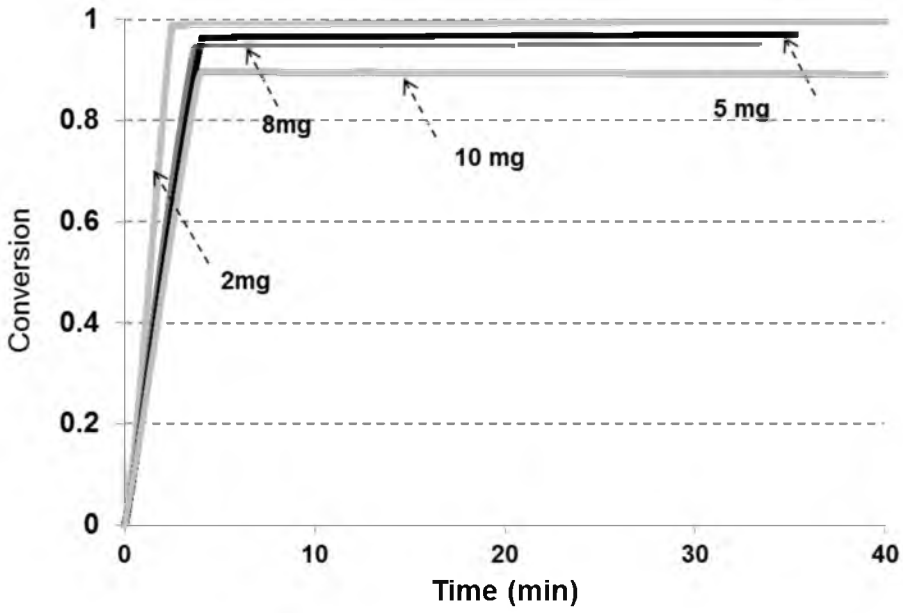

Figure 3.8 Isothermal conversion profiles fro M1300 at 600°C, oxidizer flow rate of 500 mL/min. Initial sample masses ranging from 2,5,8,and 10 mg. Comparison of the conversion profiles was used to choose the optimal initial mass loading for future experiments. A 5 mg sample was chosen fro the M1300, 8 mg for R250 and 10 mg for OLC.

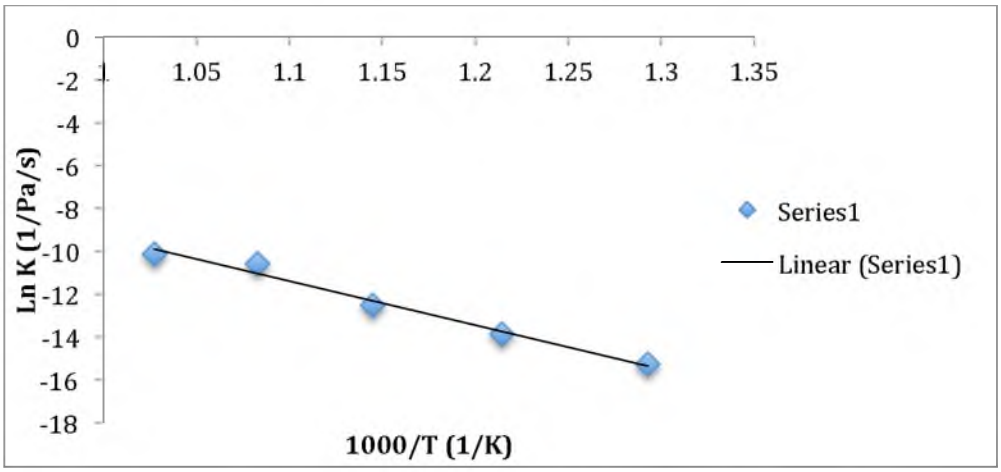

Figure 3.9 Semilog plot of the kinetic rate versus the inverse of temperature in Kelvin (multiplied by 1,000). The slope and intercept of the equation are used to calculate the activation energy and the pre-exponential factor, which determines the effectiveness of soot oxidation and stability of the soot.

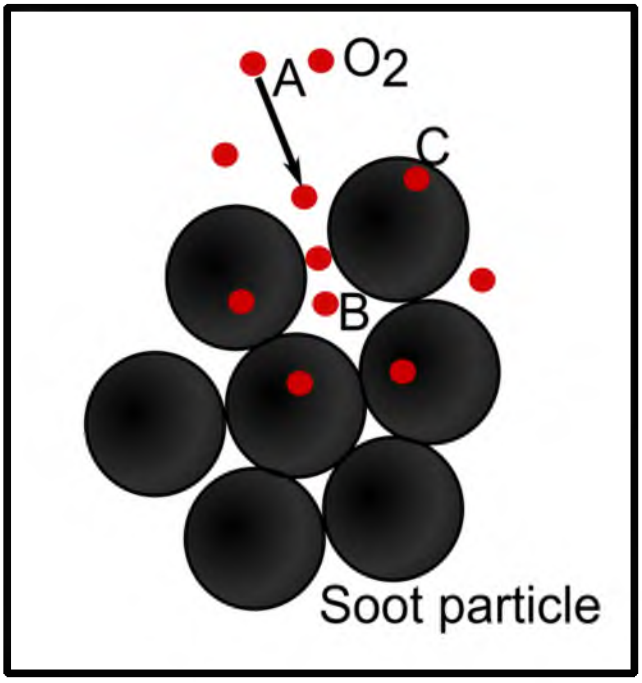

Figure 3.10 Oxygen diffusional modes for soot oxidation. A) Bulk diffusion region where oxygen diffuses to the soot particles. B) Interparticle diffusion region where oxygen diffuses between particles. C) Diffusion region where oxygen diffuses within the soot particle.

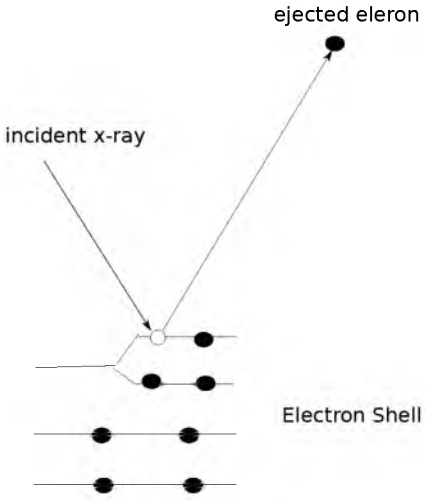

Figure 3.11 Schematic representation of the photoemission of an electron from an atom.

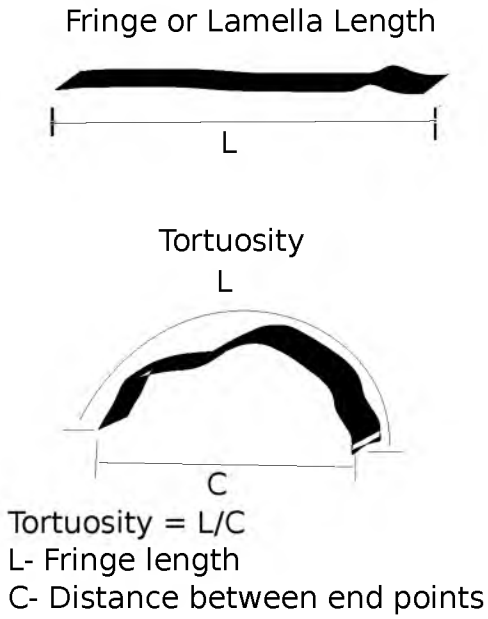

Figure 3.12 Visual representations of fringe length and tortuosity parameters describing and quantifying the nanostructure of the soot particles.

Table 3.1 Experimental conditions used for soot generation.

Fuel	Chapter	Equivalence Ratio (ϕ)	C/O Ratio	Cold Gas Velocity at STP (cm/s)	Flame Temperature, corrected for radiation (K)
Surrogate 17mol% *m*-xylene/83mol% *n*-dodecane	4	2.1	0.69	4.3	1773
40mol% *n*-butanol/60mol% *n*-dodecane	4	2.8	0.92	4.3	1777
n-dodecane	4	1.7	0.65	4.6	1705
m-xylene	4	2.15	0.7	4.6	1725
n-butanol	4	2.8	1.21	4.3	1723
10mol% *n*-butanol/90mol% *n*-dodecane	6	2.18	0.70	4.3	1725
20mol% *n*-butanol/80mol% *n*-dodecane	6	2.18	0.71	4.2	1730
30mol% *n*-butanol/70mol% *n*-dodecane	6	2.18	0.69	4.3	1745
40mol% *n*-butanol/60mol% *n*-dodecane	6	2.18	0.69	4.3	1777
60mol% *n*-butanol/40mol% *n*-dodecane	6	2.18	0.68	4.2	1777

Table 3.2 Parameter used to estimate the effectiveness factors.

Parameter	Value	Source
β	0.75	Song et al.[14], Salvador et al.[24]
$\boldsymbol{\varphi_1}$	0.65	Song et al.[14]
$\boldsymbol{\varphi_p}$	0.26	Song et al.[14], Satterfield [23]
$\boldsymbol{\tau_1}$	2.1	Song et al. 13, Song et al. 14, Brilhac et al. [26]
$\boldsymbol{\tau_p}$	2.8	Song et al.[14], Satterfield [23]
$\boldsymbol{\Omega_{AB}}$	1	Satterfield [23]
σ_{AB}	3.525	Satterfield [23]
$\boldsymbol{\rho_{b,1}}$	283 kg/m^3	Song et al. [14]
S_g	199 m^2/g	Obtained by BET
e	0.003 m	
$\mathbf{A_s}$	0.000215 m^2	

CHAPTER 4

COMPARISION OF FUEL SURROGATES AND EFFECTS OF PRESSURE ON OXIDATION KINETICS

4.1 Introduction

The oxidation kinetics of a jet-fuel surrogate, an oxygenated fuel surrogate, and a commercial carbon black (used as a reference material) were obtained using thermogravimetric analysis (TGA), which is a common and reliable method to determine oxidation kinetics. These fuels are discussed in sections 3.1, 3.1.2 and 3.1.3. Soot produced from the surrogate fuels was created using a flat-flame burner, collected and used for oxidation experiments in the high-pressure TGA, reviewed in section 3.3. The materials and the methods used for soot production and collection are outlined in section 3.2. Thermogravimetric analysis was conducted at two separate pressures (1 and 10 atm) and oxygen concentrations that varied between 10 and 21% oxygen in nitrogen gas.

Thermogravimetric experiments conducted at the elevated pressures presented with a reduction in kinetic rate constant and elevated activation energy. This is indicative of mass-transfer limitations and required additional calculations to extract the kinetic parameters. The calculations are discussed in sections 3.6.1- 3.6.4. Diffusional limitations of soot oxidation along with a variety of different approaches to account for the mass-

transfer limitations have been discussed extensively in the literature (*6, 7, 9, 11, 12, 13, 14*). Soot oxidation kinetics inside the TGA furnace are affected by oxygen diffusion into the sample, which is a partially diffusion limited reaction (*4, 5, 6, 7, 8*). When the reaction is diffusion limited, the kinetic parameters of soot oxidation cannot be directly obtained from TGA plots, rather a combination of diffusive and kinetic models are used (*9, 10*). We have chosen a simplified analysis to quantify the influence of three diffusion processes characterized by (1) diffusion of oxygen outside the particle layer, (2) diffusion of oxygen through the particle layer, and (3) diffusion of oxygen inside the porous particle. These are all described in terms of effectiveness factors, which were obtained from analytical solution of the Thiele diffusion modulus (*13, 14*).

A high-resolution transmission electron microscope (HRTEM) was used to obtain images of the soot. A description of the parameters used to describe the images and information about the HRTEM are discussed in section 3.8. These images were then put through a rigorous image analysis algorithm described in (*30*). This analysis reveals the soot nanostructure, the fringe length and the tortuosity, which was used to determine the relationship between the nanostructure and the soot reactivity for the surrogate fuels at 1 and 10 atm. Partially oxidized soot samples collected at 40 atm and were studied using HRTEM analysis; however, we were unable to extract the kinetic parameters from the data.

4.2 Results and Discussion

4.2.1 Effect of Total Pressure

The pressure of the system was varied between 1 and 10 atmospheres to determine its influence on the kinetic parameters of soot oxidation. Experiments were conducted using *m*-xylene/*n*-dodecane, a jet-fuel surrogate and a commercial carbon black, Carboxen 1000, with temperatures ranging from 550 to 625°C. The oxidizer was a 10% oxygen and 90% nitrogen mixture at a flow rate of 1.0 L/min. Figure 4.1 and 4.2 show a typical thermogram obtained from the TGA for 1 and 10 atm.

For the experiments at 1 atm, an initial weight loss of roughly 1 mg was recorded while bringing the system up to temperature in the helium environment before introduction of the oxidizer gas. A nearly linear weight loss was observed until the end of combustion, as seen in Figure 4.2.

The high-pressure TGA experiments showed an apparent increase in weight due to the pressurization of the system, but weight stabilization was achieved when the system reached the desired pressure and prior to oxidation of the sample, shown by Figure 4.2. The mass-loss data for the pressurized experiments have a variation of ±5 mg due to the small changes in pressure (±0.3 atm).

The activation energy for different soot samples under atmospheric conditions were found to be in the range reported by Ciampelli et al. (*19*), Otto et al. (*20*) and Neeft et al. (*21*) for experiments in which kinetics drove the reaction. Carboxen 1000's activation energy was also found to be in the range previously reported (*22*). Activation energy values extracted from pressurized experiments were lower than those obtained under atmospheric pressure for Carboxen 1000 and surrogate soot, respectively,

suggesting that the oxidation is not only a function of the kinetics, but is also limited by mass transfer.

For a total pressure of 1 atm, the results show that the effectiveness factors η_1, η_p, and η_e are very close to 1, shown in Table 4.1, as the gas temperature increases from 700 to 900 K. This suggests that at 1 atm and the mentioned temperature range, diffusional limitations are not a factor under these optimized conditions. The effectiveness factors start to drop at a gas temperature of 1000 K, as reported by Song et al. (*13*), suggesting the presence of diffusional limitations at elevated temperatures. Higher temperatures require faster diffusion of oxygen to the surface of the soot, if diffusion limitations are present this is exacerbated at the higher temperatures (*13*).

The effectiveness factors η_1 and η_p, for pressurized runs (10 atm) are also near 1, as seen in Table 4.1, for a gas temperature in the range from 700 to 900K and begin to drop for temperatures higher than 900 K. The effectiveness factor for external bulk diffusion is much lower than 1 for all the temperatures evaluated in this study, suggesting at higher pressures the oxidation process is dominated by external mass transfer diffusion. Table 4.2 shows the results of the kinetic parameters after mass transfer limitation corrections were applied.

4.2.2 Effect of Type of Soot

To study the role that the type of soot had on the kinetic parameters, a surrogate jet fuel, *m*-xylene/*n*-dodecane, and the pure components, *m*-xylene and *n*-dodecane were chosen for TGA experiments at pressures of 1 and 10 atm and compared to the Carboxen 1000 standard carbon black. The activation energy value for *m*-xylene/*n*-dodecane was

161 kJ/mol, *m*-xylene was 160 kJ/mol, and *n*-dodecane was 162 kJ/mol, all at 1 atm with values at 10 atm after being corrected to obtain similarity. These compared with the Carboxen 1000 standard of 141 kJ/mol. The activation energies of *m*-xylene/*n*-dodecane, *m*-xylene and *n*-dodecane are similar.

To study the effect of oxygenated fuels on the kinetic parameters *n*-butanol and a mixture of *n*-butanol/*n*-dodecane were chosen. The activation energy values were found to be 114 kJ/mol for *n*-butanol and 129 kJ/mol for the mixture of *n*-butanol/*n*-dodecane. On the other hand, the pre-exponential factor was found to increase by two orders of magnitude as *n*-butanol was added to the *n*-dodecane. This is an average decrease of 14% for the activation energy of the oxygenated fuels when compared to the jet-fuel surrogate, suggesting that the soot created from the oxygenated fuel is easier to burn. Figure 4.3 presents the mass-oxidation rates for surrogate *m*-xylene/*n*-dodecane fuel, *n*-butanol/*n*-dodecane and *n*-butanol soot samples at 600°C. A faster mass-based oxidation rate was observed with an oxygenated fuel, also suggesting easier burning of the sample.

4.2.3 HRTEM Image and Image Analysis

Figures 4.4-4.9 are the images of the soot samples that are the nascent soot collected from the flat-flame burner setup, partially oxidized soot samples collected from the TGA at pressures of 1, 10, and 40 atm. The image analysis is preformed and the histograms are created showing the distribution of fringe length and tortuosity. Quantification of the data obtained from the histograms is correlated to the structure of the soot. If there is a decrease in the fringe length and an increase in tortuosity, then the structure is becoming less organized, and conversely, if there is an increase in fringe

length and a decrease in tortuosity, then this can be related to more organized, more structured soot. Figure 4.4 illustrates that, with an increase in oxidation pressure, for the *n*-butanol/*n*-dodecane mixture, there is a progressive decrease in structure; and this is manifested by the narrowing of the lamella length distribution across the oxidation series and a broadening of the tortuosity distributions. Simply put, this corresponds to an ever shortening and increasing curvature of the lamella, and a less-organized structure for the soot. The trend shown by the *n*-butanol/*n*-dodecane mixture is not present in the pure components of the fuel as shown by Figures 4.5 and 4.6, respectively. As observed in the HRTEM images and represented by the lamella distributions, the structure of the soot at various oxidation pressures is similar to that of the nascent soot. Figure 4.7 is of the *m*-xylene/*n*-dodecane mixture and shows that this mixture does not exhibit changes between oxidation pressures or when compared to the nascent soot. The *m*-xylene sample exhibits a small flattening of the structure with oxidation pressure, as seen in Figure 4.8.

Figure 4.9 is the nascent soot series for all fuels and corresponding lamella length distributions. This figure demonstrates the point that their nascent structure is quite similar and not the origin for the observed differences in either the activation energy, kinetic rate constant or the changes in nanostructure.

HRTEM images and image analysis of all the soot samples across the pressurized conditions illustrate that with increasing pressure an amorphous region develops within the soot nanostructure. This region grows inward with increasing TGA pressure and is characterized by a loss of long lamella, a narrowing of the distribution, and a "negative" difference in the histogram difference plots. This loss of structure is a unique observation and may be due to a combination of the external surface oxidation and internal burning

modes. Oxygen may be penetrating within outer portions of the particles and causing breakup of the initial graphene segments as shown in the pressurized experiments in the TGA; as pressure increased so did the depth of break up in the soot particle.

This trend for amorphous development in the soot from the *m*-xylene/*n*-dodecane mixture is manifested in the activation energy measured using the TGA. With increasing pressure the observed activation energy decreases, prior to mass transfer calculations being performed, and only a slight decrease after the calculations are performed. This is consistent with the breakup of lamella and a possible creation of more edge sites and dangling bonds that increase the active sites on the soot leading to a quicker oxidation and fragmentation.

4.3 Summary and Conclusion

Isothermal experiments were conducted in a TGA for soot generated from different liquid fuels and for a commercial Carboxen 1000. Two total pressures were evaluated to examine the kinetic parameters, 1 and 10 atm, and oxygen concentration was varied between 10 and 21%. The liquid fuel combinations were also evaluated using HRTEM image analysis at three pressures, 1, 10, and 40 atm. An inert material was used in all the tests to minimize thermal and mass transfer effects by decreasing the stagnant region between the top surface of the soot and the entrance of the crucible. Oxidizer flow rate, initial mass loading, and amount of inert bed were optimized. Varying these parameters helped to minimize the mass transfer limitations and to ensure that the experiments were carried out under kinetic controlled conditions. The oxidation reactions were modeled using first-order reaction kinetics to determine kinetic parameters and the

change in the kinetic parameters were studied as a function of pressure. Mass transfer diffusion limitations were found to affect the pressurized experiments at the conditions evaluated in this study and effectiveness factors were used to correct for the limitations in oxygen transfer. The activation energy values for Carboxen 1000 were in close agreement with the literature values for both atmospheric and pressurized environments. Jet-fuel surrogate soot kinetic parameters were also constant when the total pressure was increased from 1 to 10 atm, and the values obtained were found to agree well with those reported in the literature for the oxidation of black carbon and soot samples. A decrease of about 28 % in the activation energy value was obtained when an oxygenated fuel (*n*-butanol) was added to *n*-dodecane. The pre-exponential factor was found to increase by two orders of magnitude as *n*-butanol was added to the *n*-dodecane. The pre-exponential factor is related to the surface area of the soot, the addition of *n*-butanol may increase the surface area of the soot, thereby lowering the activation energy.

These finding suggest that synergies between fuel components may occur, leading to different oxidation modes and changes in the kinetics parameters for soot from such fuels. Partial oxidation, well known in other macroscale carbons, leads to graphitization corresponding to a measurable increase in the carbon lamella. We have found the opposite to occur. This trend is only observed for this particular fuel combination, *n*-butanol/*n*-dodecane oxygenated surrogate fuel, not for others such as *m*-xylene/*n*-dodecane and not for any individual components, *n*-butanol, *m*-xylene, and *n*-dodecane. A comparison of the HRTEM data among any and all of the nascent soot or their combinations as binary mixtures shows very similar nanostructure by the physical metrics of lamella length and tortuosity.

4.4 References

1. Clague A. D. H.; Donnet J. B.; Wang T. K.; Peng J. C. M., A Comparison Of Diesel Engine Soot With Carbon Black. Carbon **1999,** *37*, 1553-1565.

2. Miller F. J.; Gardner J. A.; Graham R. E.; Lee W. E., Size Considerations For Establishing A Standard For Inhalable Particles. Jornal of the Air Pollution Control Association **1979,** *29*, 610-615.

3. Stanmore B. R.; Brilhac P.; Gilot P., The Oxidation Of Soot: A Review Of Experiments, Mechanism And Models. Carbon **2001,** *39*, 2247-2268.

4. Stratakis G. A.; Stamatelos A. M., Thermogravimetric Analysis Of Soot Emitted By A Modern Diesel Engine Run On Catalyst-Doped Fuel. Combustion and Flame **2003**, *132*, 157-169.

5. Song J.; Alam M.; Boehman A. L.; Kim U., Examination of the Oxidation Behavior of Biodiesel soot. Combustion and Flame **2006,** *146*, 589-604.

6. Stanmore, B. R.; Gilot, P.; Prado, G., The Influence Of Mass Transfer In DTG Combustion Tests. Thermochimica Acta **1994,** *240*, 79-89.

7. Gilot P.; Brillard A.; Stanmore B. R., Geometric Effects On Mass Transfer During Thermogravimetric Analysis: Application To Reactivity Of Diesel Soot. Combustion and Flame **1995,** *102*, 471-480.

8. Zouaoui N.; Brilhac J.; Mechati F.; Jeguirim M.; Djellouli B.; Gilot P., Study Of Experimental And Theoretical Procedures When Using Thermogravimetric Analysis To Determine Kinetic Parameters Of Carbon Black Oxidation. Journal of Thermal Analysis & Calorimetry **2010,** *102*, 837-849.

9. Kalogirou M.; Samaras Z., A Thermogravimetric Kinetic Study Of Uncatalized Diesel Soot Oxidation. Journal of Thermal Analysis & Calorimetry **2009,** *98*, 215-224.

10. Kalogirou M.; Samaras Z., Soot Oxidation Kinetics From TG Experiements. Journal of Thermal Analysis & Calorimetry **2010,** *99*, 1005-1010.

11. Rodriguez-Fernandez, J.; Oliva, F.; Vazquez, R.A., Characterization Of The Diesel Soot Oxidation Precess Through An Optimized Thermogravimetric Method. Energy & Fuels **2011,** *25*, 2039-2039.

12. Gilot P.; Bonnefoy F.; Marcuccilli F.; Prado G., Determination Of Kinetic Data For Soot Oxidation. Modeling The Competition Between Oxygen Diffusion And Reaction During Thermogravimetric Analysis. Combustion and Flame **1993,** *95*, 87-100.

13. Song J.; Chung-Hwan J.; Boehman A., Impacts Of Oxygen Diffusion On The Combustion Rate Of In-Bed Soot Particles. Energy & Fuels **2010,** *24*, 2418-2428.

14. Song Q.; He B.; Yao Q.; Meng Z.; Che C., Influence Of Diffusion On Thermogravimetric Analysis Of Carbon Black Oxidation. Energy & Fuels **2006,** *20*, 1895-1900.

15. Ranzi E., A Wide-Range Kinetic Modeling Study Of Oxidation And Combustion Of Transportation Fuels And Surrogate Mixtures. Energy & Fuels **2006,** *20*, 1024-1032.

16. Edwards T., Liquid Fuels And Propellants For Aerospace Propulsion. Journal of Propulsion and Power **2003,** *19*, 1089-1107.

17. Westbrook C. K.; Pitz W. J., Motor Fuels: Energy Efficiency and Emissions in Transportation. fuel **2002,** *12*, 132**.**

18. McEnally C. S.; Koylu U. O.; Pfefferle L. D.; Rosner D. E., Soot Volume Fraction And Temperature Measurements In Laminar Non-Premixed Flames Using Thermocouples. Combustion and Flame **1997,** *109*, 701-720.

19. Ciambelli P.; Corbo P.; Gambino M.; Palma V.; Vaccaro S., Catalytic Combustion Of Carbon Particulate. Catalysis Today **1996**, *27*, 99-106.

20. Otto K.; Sieg M. H.; Zinbo M.; Baartosiewz L., The Oxidation Of Soot Deposits From Diesel Engines. SAE **1981.**

21. Neeft J. P.; Nijhuis T. X.; Makkee M.; Moulijn J. A., Kinetics Of The Oxidation Of Diesel Soot. Fuel **1997,** *76*, 1129-1136.

22. Sorensen L. H .; Gjernes T.; Fjellerup J., Determination Of Reactivity Parameters Of Model Carbons, Cokes And Flame-Chars. Fuel **1996,** *75*, 31-38.

23. Satterfield C. N., Mass Transfer In Heterogeneous Catalysis; MIT Press: Cambridge, MA, **1970.**

24. Salvador S.; Commandre, J. M.; Stanmore, B.R., Reaction Rates For The Oxidation Of Highly Sulphurised Petroleum Cokes. Fuel **2003,** *82*, 715-720.

25. Incropera F. P.; Dewit D. P., Fundamental of Heat and Mass transfer; Wiley & Sons: New York, **1970.**

26. Brilhac J. F.; Bensouda F.; Gilot P.; Brillard A.; Stanmore B., Experimental And Theoretical Study Of Oxigen Diffusion Within Packed Beds Of Carbon Black. Carbon **2000,** *38*, 1011-1019.

27. Turns A. R., An Introduction To Combustion: Concepts and Applications; McGraw Hill: Inc **1996.**

28. Bird R. B., Transport Phenomena; Wiley & Sons: New York, **1960.**

29. Hecker W. C.; Madsen, P. M.; Sherman M. R.; Allen J. W.; Sawaya R. J.; Fletcher T. H., High Pressure Intrinsic Oxidation Kinetics Of Two Coal Chars. Energy & Fuels **2003,** *17*, 427-432.

30. Yehliu K.; Vander Wal R. L.; Boehman A. L., Combust. Flame **2011,** *158*, 1837-1851.

31. Edwards T., Surrogate Mixtures to Represent Complex Aviation and Rocket Fuels. Journal of Propulsion and Power **2001,** *17*, 2.

32. Sigma-Aldrich, High-Tech Carbons, Material Matters **2009,** *44*, 110.

33. Marcucilli F.; Gilot P.; Stanmore B. R.; Prado G., Experimental and theoretical study of diesel soot reactivity. The Combustion Institute **1994,** 619–26.

34. Otto K.; Sieg M. H.; Zinbo M.; Bartosiewicz L., The Oxidation Of Soot Deposits From Diesel Engines. SAE **1981,** 800336.

35. Brilhac J. F.; Bensouda F.; Gilot P.; Brillard A.; Stanmore B., Experimental And Theoretical Study Of Oxygen Diffusion Within Packed Beds Of Carbon Black. Carbon **2000,** *38*, 1011– 9.

36. Soete G., Catalysis Of Soot Combustion By Metal Oxides. The Combustion Institute **1988.**

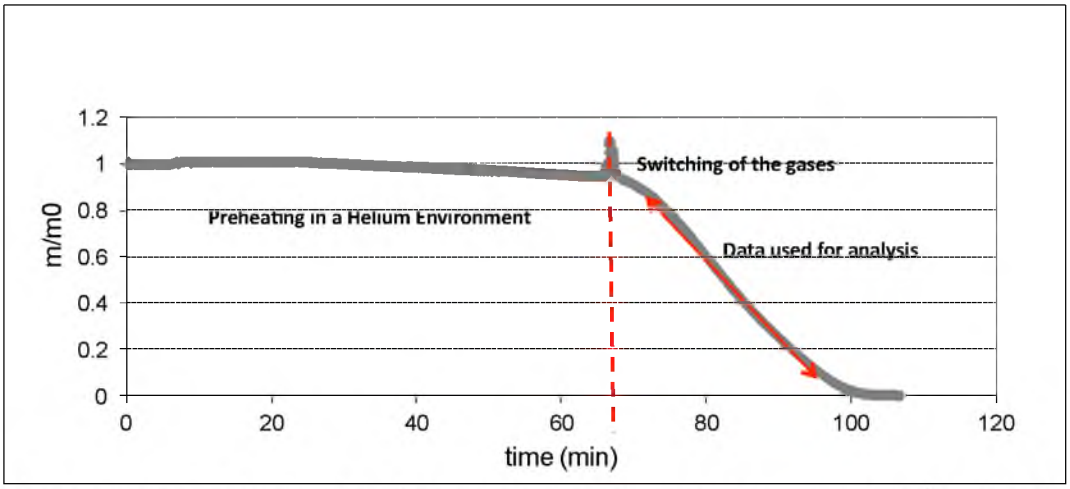

Figure 4.1 Normalized weight loss versus time, for a soot sample at 600°C, 10% oxygen and 1 atm. An initial weight loss of about 1 mg is seen due to the loss of volatiles in the helium environment during the heating ramp.

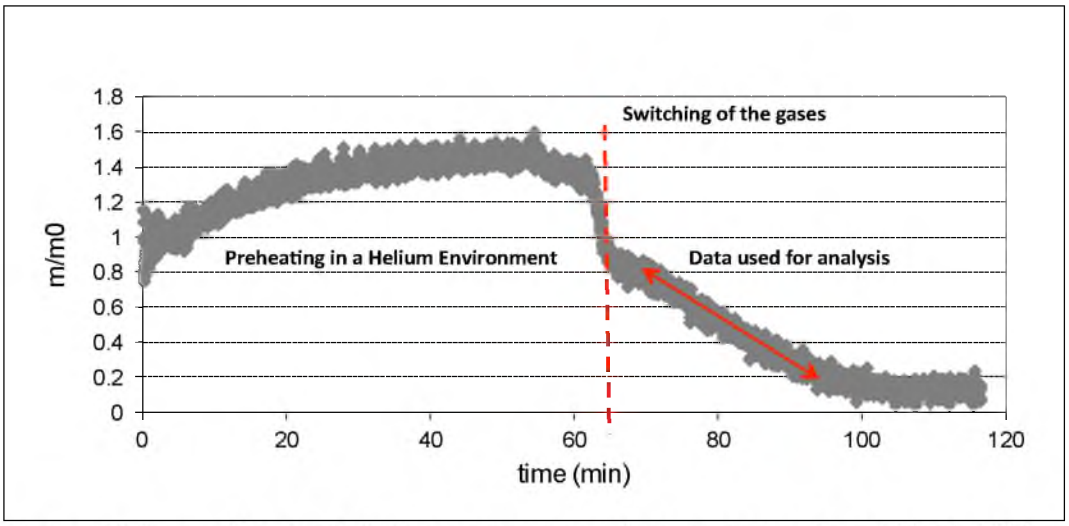

Figure 4.2 Normalized weight loss versus time, for a soot sample at 600oC, 10% oxygen and 10 atm. An apparent increase in the mass is shown due to the heating and pressurization of the system, mass-loss data are allowed to stabilize after the oxidizer is applied.

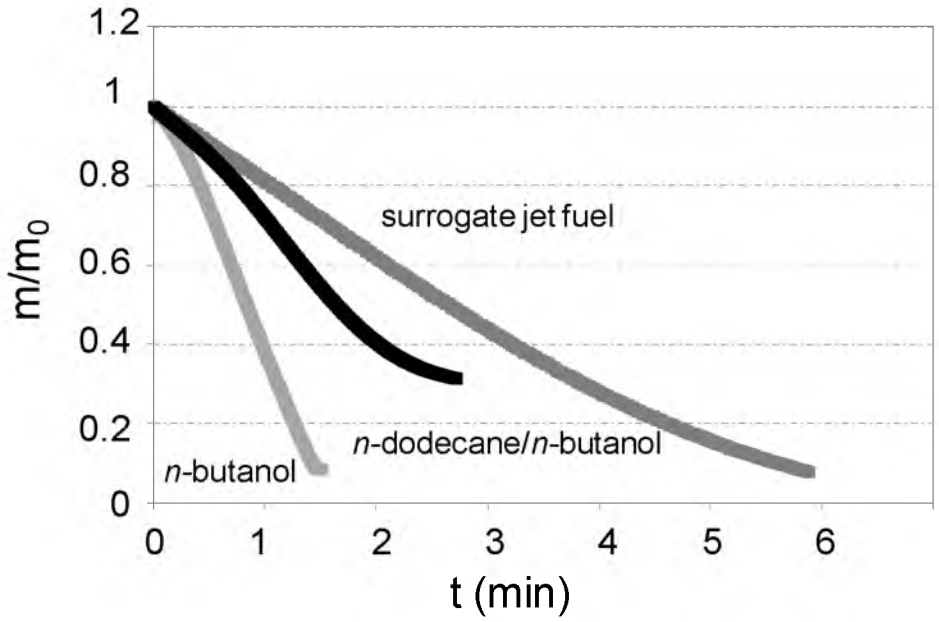

Figure 4.3 Mass-based oxidation rates for three different soot samples at 600°C oxidized in air. Showing the *n*-butanol oxidation rate is the fastest, *n*-butanol/*n*-dodecane kinetic rate is slower, and the surrogate fuel, *m*-xylene/*n*-dodecane, has the slowest kinetic rate.

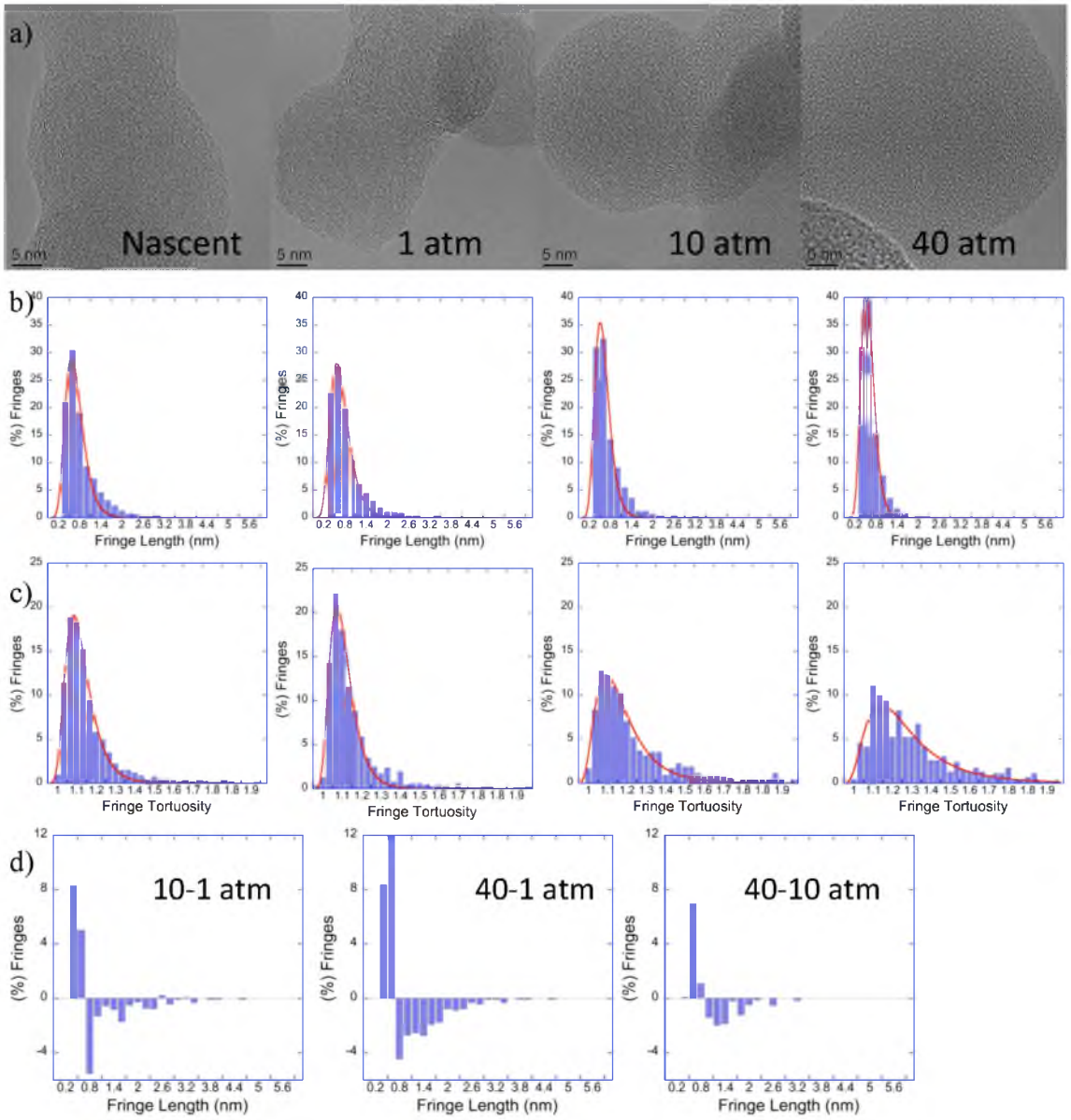

Figure 4.4 a) *n*-butanol/ *n*-dodecane mixture HRTEM images and analysis, illustrating that with an increase in oxidation pressure, for the *n*-butanol/*n*-dodecane mixture, there is a progressive decrease in structure, and this is manifested by the narrowing of the lamella length distribution across the oxidation series and a broadening of the tortuosity distributions.

Images are obtained from the HRTEM, histograms labeled b) Fringe Length show the concentration of fringe length in nanometers, histograms labeled c) Fringe Tortuosity show the concentration of the fringe tortuosity in nanometers. The images and histograms are aligned vertically corresponding to the Nascent, 1 atm, 10 atm, and 40 atm. Difference plots labeled d) 10-1 atm, 40-1 atm, and 40-10 atm are aligned horizontally at the bottom of the figures and show how the change in pressure effects the fringe length.

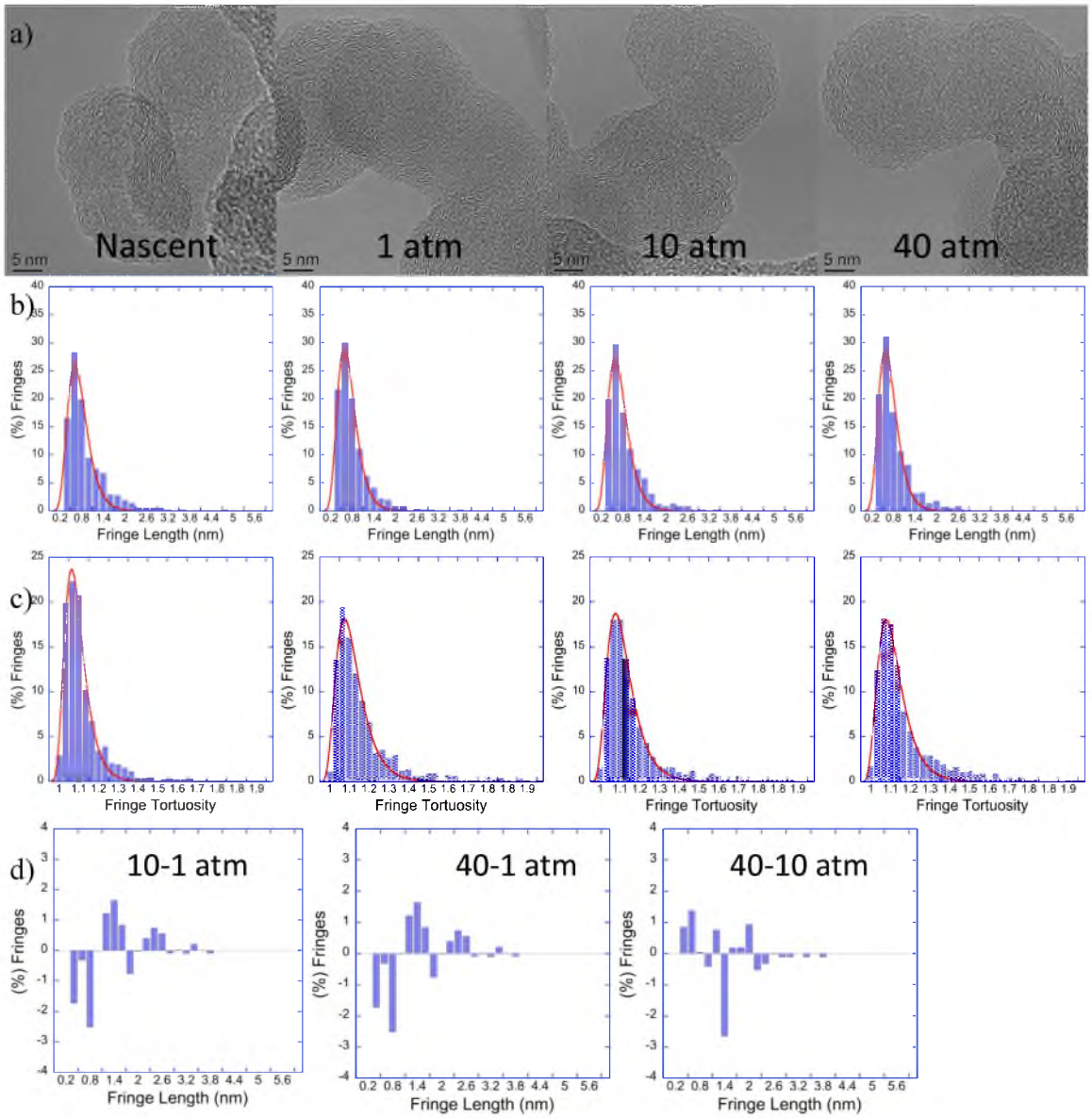

Figure 4.5 a) *n*-butanol HRTEM images and analysis. There is not a significant change in the lamella length and the tortuosity.
Images are obtained from the HRTEM, histograms labeled b) Fringe Length show the concentration of fringe length in nanometers, histograms labeled c) Fringe Tortuosity show the concentration of the fringe tortuosity in nanometers. The images and histograms are aligned vertically corresponding to the Nascent, 1 atm, 10 atm, and 40 atm. Difference plots labeled d) 10-1 atm, 40-1 atm, and 40-10 atm are aligned horizontally at the bottom of the figures and show how the change in pressure effects the fringe length.

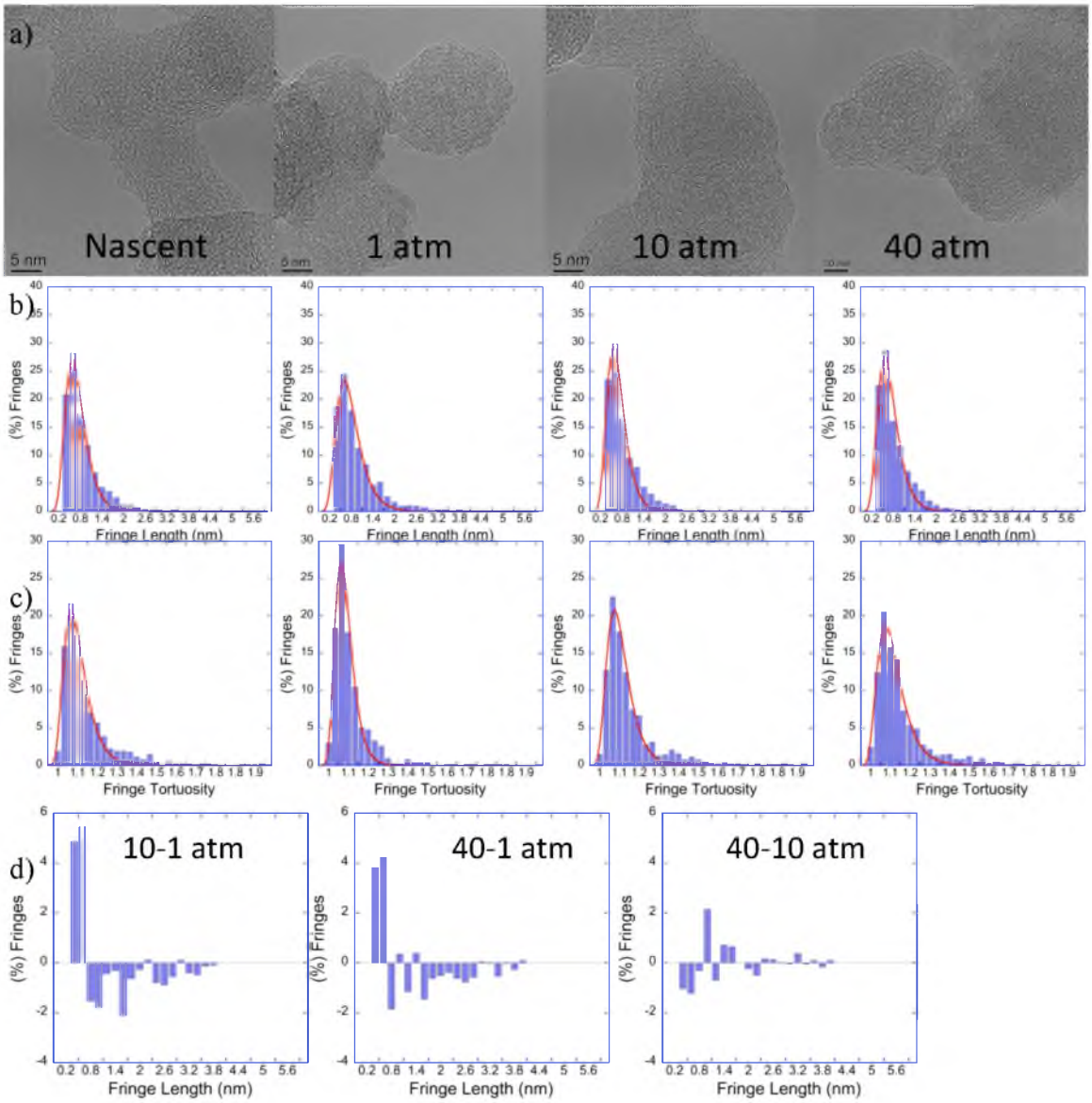

Figure 4.6 a) *n*-dodecane HRTEM images and analysis. There is not a significant change in the lamella length and the tortuosity.
Images are obtained from the HRTEM, histograms labeled b) Fringe Length show the concentration of fringe length in nanometers, histograms labeled c) Fringe Tortuosity show the concentration of the fringe tortuosity in nanometers. The images and histograms are aligned vertically corresponding to the Nascent, 1 atm, 10 atm, and 40 atm. Difference plots labeled d) 10-1 atm, 40-1 atm, and 40-10 atm are aligned horizontally at the bottom of the figures and show how the change in pressure effects the fringe length.

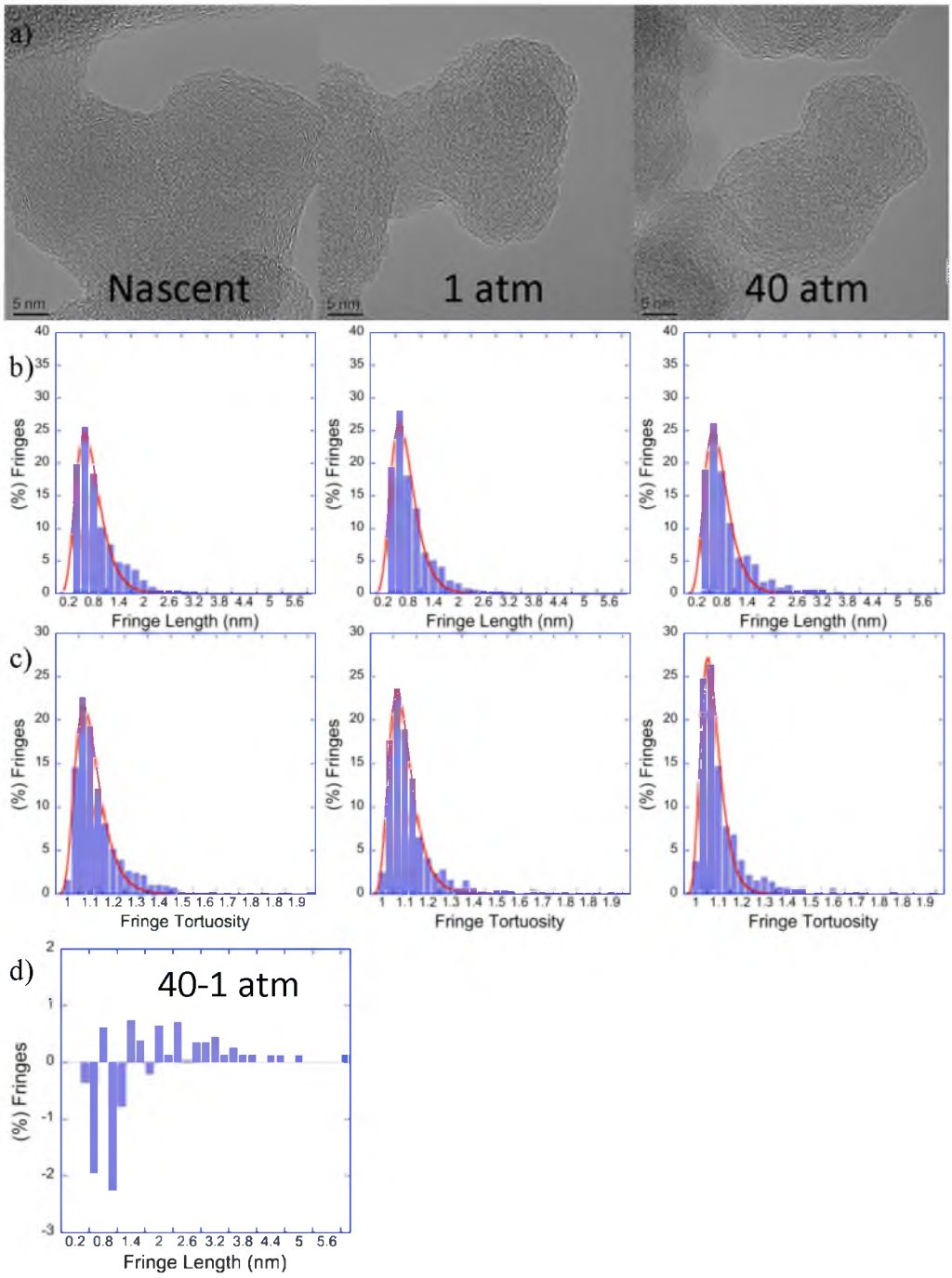

Figure 4.7 a) *m*-xylene/*n*-dodecane HRTEM images and analysis. Showing that this mixture does not exhibit changes between oxidation pressures and when compared to the nascent soot.
Images are obtained from the HRTEM, histograms labeled b) Fringe Length show the concentration of fringe length in nanometers, histograms labeled c) Fringe Tortuosity show the concentration of the fringe tortuosity in nanometers. The images and histograms are aligned vertically corresponding to the Nascent, 1 atm, and 40 atm. Difference plots labeled d) 40-1 atm are aligned horizontally at the bottom of the figures and show how the change in pressure effects the fringe length.

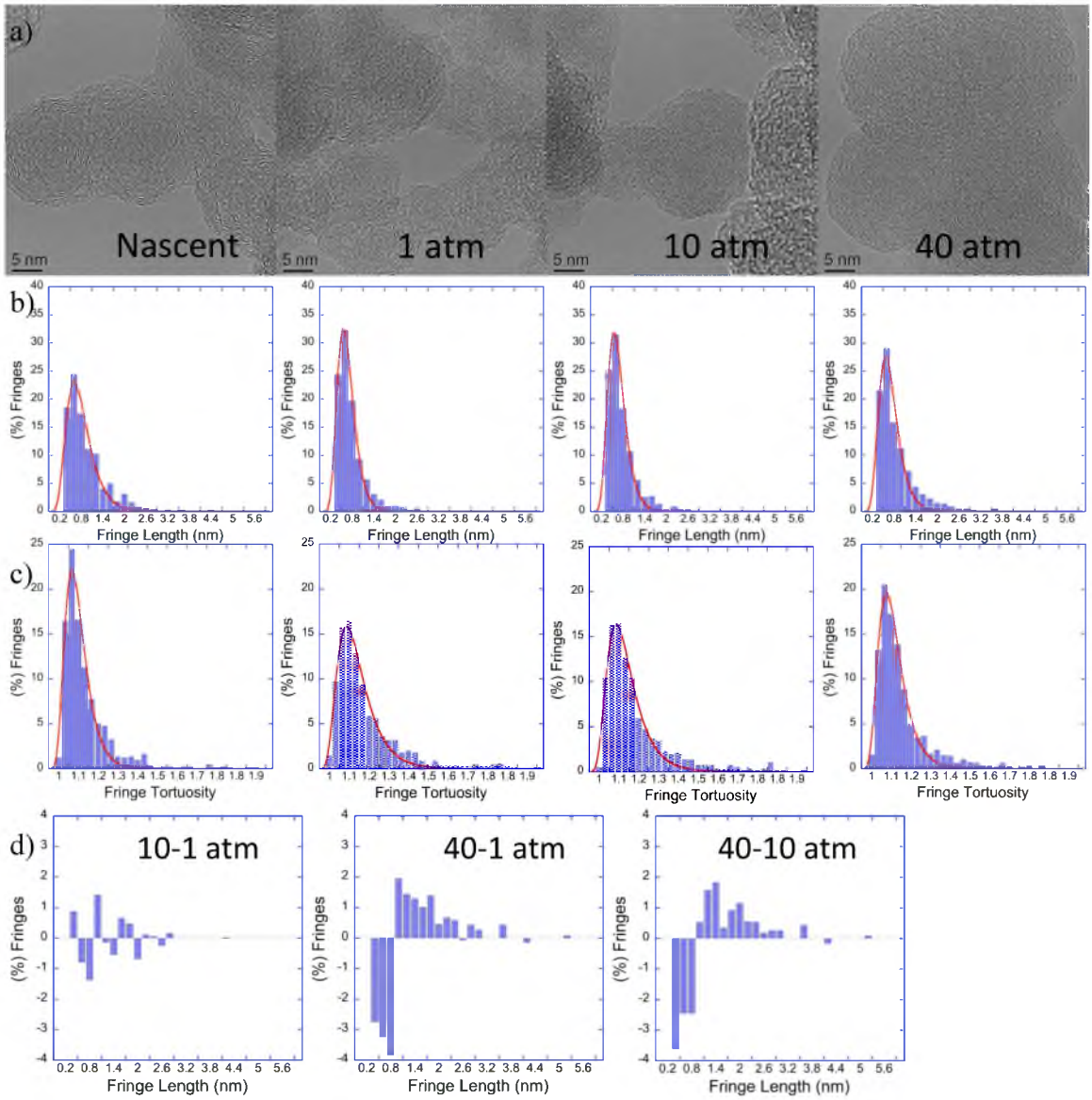

Figure 4.8 a) *m*-xylene HRTEM images and analysis. As pressure increases the fringe lengths are increasing and the tortuosity is decreasing, the structure of the soot is becoming flatter.
Images are obtained from the HRTEM, histograms labeled b) Fringe Length show the concentration of fringe length in nanometers, histograms labeled c) Fringe Tortuosity show the concentration of the fringe tortuosity in nanometers. The images and histograms are aligned vertically corresponding to the Nascent, 1 atm, 10 atm, and 40 atm. Difference plots labeled d) 10-1 atm, 40-1 atm, and 40-10 atm are aligned horizontally at the bottom of the figures and show how the change in pressure effects the fringe length.

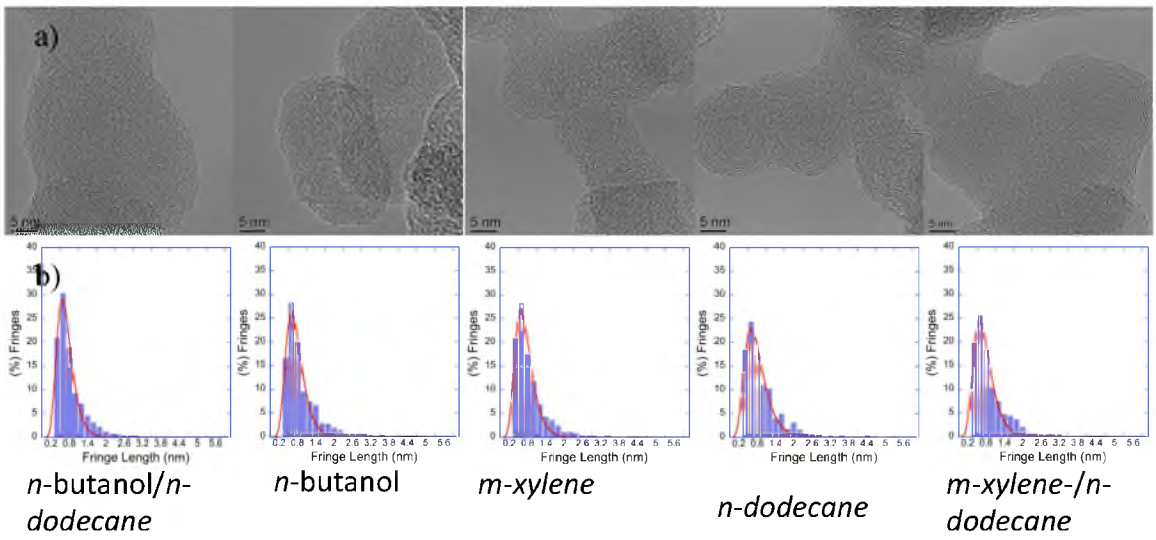

Figure 4.9 Fringe analysis for nascent soot samples for the fuel combinations, demonstrating the point that their nascent structure is quite similar and not the origin for the observed differences in either the activation energy, kinetic rate or the changes in nanostructure. a) HRTEM images of the all nascent soot samples created from all fuel combinations studied. b) Fringe length histograms for the HRTEM images

Table 4.1 Effectiveness factors for the three separate diffusional processes at 1 and 10 atm.

		1 atm		
Fuel sample	T(K)	η_p (Oxygen diffusion between the particles)	η_l (Oxygen diffusion within the particle)	η_e (Oxygen diffusion to the particle layer)
Surrogate *m*-xylene/*n*-dodecane	700	1	1	1
	800	1	1	1
	900	0.99	0.99	0.99
	1000	0.96	0.93	0.92
Carboxen 1000	700	1	1	1
	800	1	1	0.99
	900	0.99	0.99	0.99
	1000	0.98	0.99	0.98
		10 atm		
Fuel sample	T(K)	η_p	η_l	η_e
Surrogate *m*-xylene/*n*-dodecane	700	0.99	0.99	0.53
	800	0.98	0.97	0.46
	900	0.5	0.38	0.1
	1000	0.1	0.07	0.01
Carboxen 1000	700	0.99	0.99	0.56
	800	0.99	0.99	0.45
	900	0.65	0.61	0.1
	1000	0.23	0.15	0.01

Table 4.2 Kinetic parameters activation energy and pre-exponential factor, at 1 and 10 atm; mass-transfer limitation corrections were applied to experiments at elevated pressures.

Soot sample	% O_2	Total pressure (atm)	E_a (kJ/mol)	A ($Pa^{-1}min^{-1}$)
Carboxen	10	1	141	1.43E+05
Carboxen	10	10	142	8.90E+04
m-Xylene	10	1	160	2.63E+05
m-Xylene	10	10	161	1.58E+04
n-Dodecane	10	1	162	2.03E+05
n-Dodecane	10	10	165	1.56E+04
m-Xylene/*n*-Dodecane	10	1	161	3.04E+05
m-Xylene/*n*-Dodecane	10	10	162	6.07E+03
Soot sample	% O_2	Total pressure (atm)	E_a (kJ/mol)	A ($Pa^{-1}min^{-1}$)
n-Butanol/n-Dodecane	21	1	129	7.38E+03
n-Butanol	21	1	114	2.67E+02

CHAPTER 5

OXIDATION KINETICS AND NANOSTRUCTURE OF MODEL CARBONS BASED ON THERMOGRAVIMETRIC (TGA) DATA AND HIGH-RESOLUTION TRANSMISSION ELECTRON MICROSCOPE (HRTEM) IMAGE ANALYSIS

5.1 Introduction

An investigation of three model carbons, M1300, R250, OLC and commercially produced diesel soot was conducted to find a correlation between oxidation kinetics and nanostructure. Thermogravimetric analysis (TGA) was preformed at isothermal temperatures. A description of the Q600 is provided in section 3.4. Arrhenius kinetics were used to extract the kinetic parameters of activation energy (E_a), kinetic rate (k_c) and the pre-exponential factor (A), discussed in section 3.5. A description of the model carbons and the diesel soot is presented in section 3.1 and 3.1.1.

A high-resolution transmission electron microscope (HRTEM) was used to obtain images of the samples, which were then put through a rigorous image analysis algorithm described in (*13*). This analysis reveals the soot nanostructure, the fringe length and the

tortuosity. The resulting data were used to determine the relationship between nanostructure and soot reactivity.

5.2 Data Analysis and Results

A series of experiments to determine the kinetic parameters were conducted at atmospheric conditions over a range of temperatures, depending on the type of sample, as shown in Table 5.1. The mass loss data chosen for analysis were between the conversion of 20 and 60% for M1300, diesel, and R250, and 10 and 60% for OLC. This conversion range was chosen for comparison of kinetic parameters of similar studies (*12, 13, 23, 24*). As shown in Table 5.2, the activation energies for the oxidation of the model carbon samples ranged from 124 to 204 kJ/mol. These values are comparable to reported values of previous studies (*12, 13, 23, 24*). Table 5.3 shows the kinetic rate constants over a range of temperatures. M1300 has the highest kinetic rate constants and the lowest activation energy for this study, except at higher temperatures. This exception may be due to the oxygen diffusion limitations at high temperatures where soot oxidation rate is high and is limited by the lack of oxygen. R250 exhibited lower kinetic rates and a higher activation energy than the M1300, and also showed a similar trend at the higher temperatures. OLC had the slowest kinetic rate and the highest activation energy.

Figure 5.1 is a comparison of the conversion profiles for the model carbons and the diesel soot, allowing for visualization of the kinetic rates of the samples studied. OLC, with the highest ordered structure, has the slowest rate. R250 and diesel are very similar in structure, and kinetic rate constant while M1300 is the lowest ordered structure and displayed the highest kinetic rate constant.

Shown in Figure 5.2 is the percent of mass loss per time for the R250 sample at 575°C. At approximately 65% conversion of the sample, a change in the slope occurs, relating to a change in the kinetic rate constant and activation energy. This difference in slope may be due to changes in structure, or possibly creation of a different compound. The same effect was identified at temperatures of 600, 625, and 650°C.

Figure 5.3, 5.4, and 5.5 show the images for nascent soot, partially oxidized soot at 1, and 10 atm with the histograms quantifying the fringe lengths, tortuosity and the differences in these parameters from sample to sample. Quantification of the data obtained from the histograms is correlated to the structure of the soot. If there is a decrease in the fringe length and an increase in tortuosity, then the structure is becoming less organized. Conversely, if there is an increase in fringe length and a decrease in tortuosity, then this can be related to more organized, more structured soot.

After being oxidized to 50% by weight, the samples were removed and placed into vials containing ethanol. The mixture was filtered in a BHS Sonthofen pressurized filtration system and sonicated for 15 minutes. Using a micropipette one drop of liquid was place on a Ted Pella 200-mesh Formvar coated lacey carbon TEM grid. Images were obtained and a rigorous imaging analysis algorithm was performed at Penn State University [13].

Beginning with the M1300 sample, the least structured model carbon with the highest kinetic rate constant and the lowest activation energy, one would expect the nascent image to show a high degree of tortuosity and shorter fringe lengths. Figure 5.3 confirms these findings. The images in Figure 5.3 for the partially oxidized samples at both 1 atm and 10 atm show roughened surfaces, which is indicative of oxidation of the

sample. The change in structure across the oxidation pressures was minimal. However, as seen in Table 5.4, progressing from nascent soot to the oxidized soot there was an observed increase in lamella length and a decrease in tortuosity.

R250 samples showed that with increasing oxidation pressure, there is a progressive increase in structure, as manifested by the broadening of the lamella length distribution across the oxidation series. This corresponds to longer lamella, and a narrowing of the complementary tortuosity distributions. Both of these observations suggest that the layer planes are becoming longer and have less curvature.

The R250 sample, before 65% conversion partially oxidized at 1 atm shows extended lamella at the particle perimeters, clearly observable in Figure 5.4. Hollow shell-like particles appear together within aggregates. The overlapping of particles generally obscures clear visualization except those at the aggregate perimeter. The images in Figure 5.4 show that while some particles have been oxidized, others have not. This burning mode, coupled with nonoxidized particles suggests a consistent picture of mass transport limitations leading to slow burnout.

Beyond 65% conversion, the R250 sample showed an internal burning mode, leading to the formation of hollow shells. Figure 5.6 shows the formation of hollow shells. This suggests a faster kinetic rate and lower activation energy. The hollow shell formation is often termed in coal literature as oxidation induced densification. During soot oxidation this effect is related to induced graphitization (*13*). This change in burning mode was earlier reported for diesel soot, but is a unique observation for R250.The partially oxidized R250 model carbon at a pressure of 10 atm shows that an external burning occurred where layer plane groups “flaked off” and were consumed.

The highly structured OLC model carbon shown in Figure 5.6 depicts the images for the nascent soot and partially oxidized samples in the TGA at pressures of 1 and 10 atm. The difference plots and parameterized median values show that the OLC model carbon, partially oxidized at 1 atm, shows a decrease or a narrowing of the tortuosity distribution, signifying that the structure is flattening out. The histograms show that the differences in the structure of the sample at 1 atm and the nascent soot are similar. For the sample at a pressure of 10 atm, the fringe lengths decreased and the tortuosity increased, and the outer surface of the soot showed a broken or eaten structure. This observation could signify the penetration of oxygen into the outer portions of the soot particles.

Images for the diesel soot are shown in Figure 5.7. The image analysis was not conducted. Visual inspection shows that the diesel soot is similar to the R250 in structure and oxidation. Hollow shells were formed both inside the particle and on the edges. Quantification using image analysis is necessary for further investigation.

5.3 Summary and Conclusion

The model carbons, M1300, R250, OLC and commercially produced diesel soot kinetic parameters were extracted using Arrhenius kinetics. The activation energies ranged from 124 to 204 kJ/mol. M1300 showed the least amount of structure correlating to the lowest activation energy and largest kinetic rate. The OLC model carbon had the most structure and the highest activation energy and the slowest kinetic rate. The diesel soot and the R250 were found to be in the middle for structure activation energy and kinetic rate.

The structure of the M1300 model carbon was more amorphous with more edge sites, which has been shown to be more reactive. This result was in agreement with the kinetic parameters. Image analysis showed changes in the nascent soot and the partially oxidized samples at 1 and 10 atm. Oxidation of the M1300 revealed increased fringe length and decreased tortuosity. The differences in the oxidation pressures were not significant. The R250 model carbon showed an increase in the fringe length and a decrease in the tortuosity across the nascent soot and the two pressurized cases. Near 65% conversion the R250 sample showed evidence of two separate burning modes and a change in kinetic rate. The OLC did not show significant changes between the 1 atm sample and the nascent soot sample. At 10 atm, OLC showed an outer surface breakup, possibly due to the oxygen penetrating into the outer portions of the particles.

Comparison of nanostructure and kinetic parameters of model carbons, of a highly organized OLC model carbon and an amorphous less structured M1300 model carbon, has shown that a more structured model carbon has a lower kinetic rate and higher activation energy. The lower kinetic rate, meaning a more stable model carbon, slows the burnout of the soot. Furthermore, higher activation energy increases the difficulty of burnout leading to increased temperatures for complete burnout. Conversely, the less structured model carbons have higher kinetic rates, increasing the oxidation or burnout, and lower activation energies lowering the temperature for complete burnout.

5.4 References

1. Boehman A. L.; Song J.; Alam A., Impact of Biodiesel Blending on Diesel Soot and the Regeneration of Particle Filters. Energy and Fuels **2001,** *19*, 1857-1864.
2. Chang I. P., Climate Change: The scientific basis. Cambridge, UK: Cambridge

University Press **2001.**

3. Clague A. D. H.; Donnet J. B.; Wang T. K.; Peng, J. C. M., A Comparison Of Diesel Engine Soot With Carbon Black. Carbon **1999,** *37*, 1553-1565.

4. Gilot P.; Brillard A.; Stanmore B. R., Geometric Effects On Mass Transfer During Thermogravimetric Analysis: Application To Reactivity Of Diesel Soot. Combustion and Flame **1995,** *102*, 471-480.

5. Kalogirou M.; Samaras Z., A Thermogravimetic Kinetic Study Of Uncatalyzed Diesel Soot Oxidation. Journal of Thermal Analysis and Calorimetry **2009,** *98*, 215-224.

6. Kalogirou M.; Samaras Z.; Soot Oxidation Kinetics From TG Experiments: Can They Be Used Reliably In Diesel Particulate Filter Modeling Tools? Journal of Thermal Analysis and Calorimetry **2010,** *99*, 1005-1010.

7. Liati A.; Dimopoulos D.; Eggenschwiler P.; Schreiber D.; Zelenay V.; Ammann M., Variations In Diesel Soot Reactivity Along The Exhaust After-Treatment System, Based On The Morphology And Nanostructure Of Primary Soot Particles. Combustion and Flame **2013,** *160*, 671-681.

8. Lighty J. S.; Veranth J. M.; Sarofim A. F., Combustion Aerosols: Factors Governing Their Size And Composition And Implications To Human Health. Journal of Air and Waste Management **2000,** *50*, 1565-1618.

9. Neeft J. P. A.; Nijhuis T. X.; Makkee M.; Moulijn, J. A., Kinetics Of The Oxidation Of Diesel Soot. Fuel **1997,** *76*, 1129-36.

10. Pahalagedara L.; Sharma H.; Kuo C.H.; Dharmarathna S.; Joshi A.; Suib S.L.; Mhadeshwar A. B.; Structure and Oxidation Activity Correlations for Carbon Blacks and Diesel Soot. Energy and Fuels **2012,** *26*, 6757-6764.

11. Sharma H. N.; Pahalagedara L.; Joshi A.; Suib S. L.; Mhadeshwar A. B.; Experimental Study Of Carbon Balck And Diesel Engine Soot Oxidation Kinetics Using Thermogravimetric Analysis. Energy and Fuels **2012,** *26*, 5613-5625.

12. Song J.; Chung-Hwan J.; Boehman A., Impacts of Oxygen Diffusion on the Combustion Rate of In-Bed Soot Particles. Energy Fuels **2012,** *24*, 2418-2428.

13. Yehliu K.; Vander Wal R. L.; Boehman A.L., Combust. Flame **2011,** *158*, 1837-1851.

14. Song Q.; He B.; Yao Q.; Meng Z.; Che C., Influence of Diffusion on Thermogravimetric Analysis of Carbon Black Oxidation. Energy Fuels **2006,** *20*, 1895-1900.

15. Stanmore B.; Gilot P.; Prado G., The Influence Of Mass Transfer In DTG Combustion Tests. Thermochimica Acta **1994,** *240*, 79-89.

16. Stratakis G. A.; Stamatelos A. M., Thermogravimetric Analysis Of Soot Emitted By A Modern Diesel Engine Run On Catalyst-Doped Fuel. Combustion and Flame **2003,** *132*, 157-169.

17. Vander Wal R. L.; Tomasek A. J., Soot Oxidation: Dependence Upon Initial Nanostructure. Combustion and Flame **2003,** *134*, 1-9.

18. Vander Wal R. L.; Tomasek A. J.; Street K.; Hull D. R.; Thompson W. K., Carbon Nanostructure Examined by Lattice Fringe Analysis of High-Resolution Transmission Electron Microscopy Images. Applied Spectroscopy **2004,** *58*, 230-237.

19. Vander Wal R. L.; Mueller C. J., Initial Investigation of Effects of Fuel Oxygenation on Nanostructure of Soot from Direct-Injection Diesel Engine. Energy & Fuels **2006,** *20*, 2364-2369.

20. Vander Wal R. L.; Yezerets A.; Currier N. W.; Kim D. H.; Wang C. M., HRTEM Study Of Diesel Soot Collected From Diesel Particulate Filters. Carbon **2007,** *45*, 70-77.

21. Boehman A. L.; Song J.; Alam A., Impact of Biodiesel Blending on Diesel Soot and the Regeneration of Particulate Filters. Energy and Fuels **2005,** *19*, 1857-1864.

22. Vander Wal R. L.; Bryg V. M.; Hays M. D., Fingerprinting Soot (Towards Source Identification) Physical Structure and Chemical Composition. Aerosol science **2010,** *41*, 108-117.

23. Vyazovkin S.; Burnham A. K.; Criado J. M.; Perez-Maqueda L. A.; Popescu C.; Sbirrazzuoli N.; Thermochim. Acta **2011,** *520*, 1-19.

24. Zouaoui N.; Brilhac J.F.; Mechati F.; Jequirim M.; Djellouli B.; Gilot P., Study Of Experimental And Theoretical Procedures When Using Thermogravimetric Analysis To Determine Kinetic Parameters Of Carbon Black Oxidation. Journal of Thermal Analysis and Calorimetry **2010,** *102*, 837-849.

25. Marcucilli F.; Gilot P.; Stanmore B. R.; Prado G., Experimental And Theoretical Study Of Diesel Soot Reactivity. The Combustion Institute **1994,** 619–26.

26. Otto K.; Sieg M. H.; Zinbo M.; Bartosiewicz L., The Oxidation Of Soot Deposits From Diesel Engines. SAE **1981,** 800336.

27. Brilhac J. F.; Bensouda F.; Gilot P.; Brillard A.; Stanmore B., Experimental And Theoretical Study Of Oxygen Diffusion Within Packed Beds Of Carbon Black. Carbon **2000,** *38*, 1011– 9.

28. Soete G., Catalysis Of Soot Combustion By Metal Oxides. The Combustion Institute, **1988.**

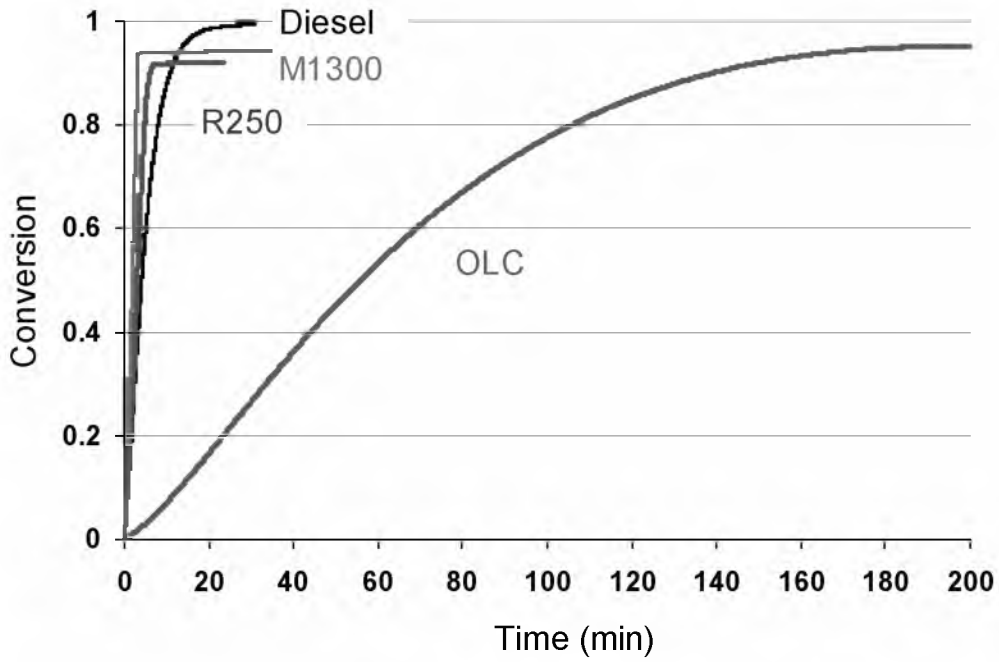

Figure 5.1 Conversion profiles for the M1300, R250, diesel soot and OLC samples. OLC has the slowest conversion rate for the samples studied. The diesel soot and the R250 are similar in conversion rate and quicker than the OLC. The quickest conversion rate is the M1300.

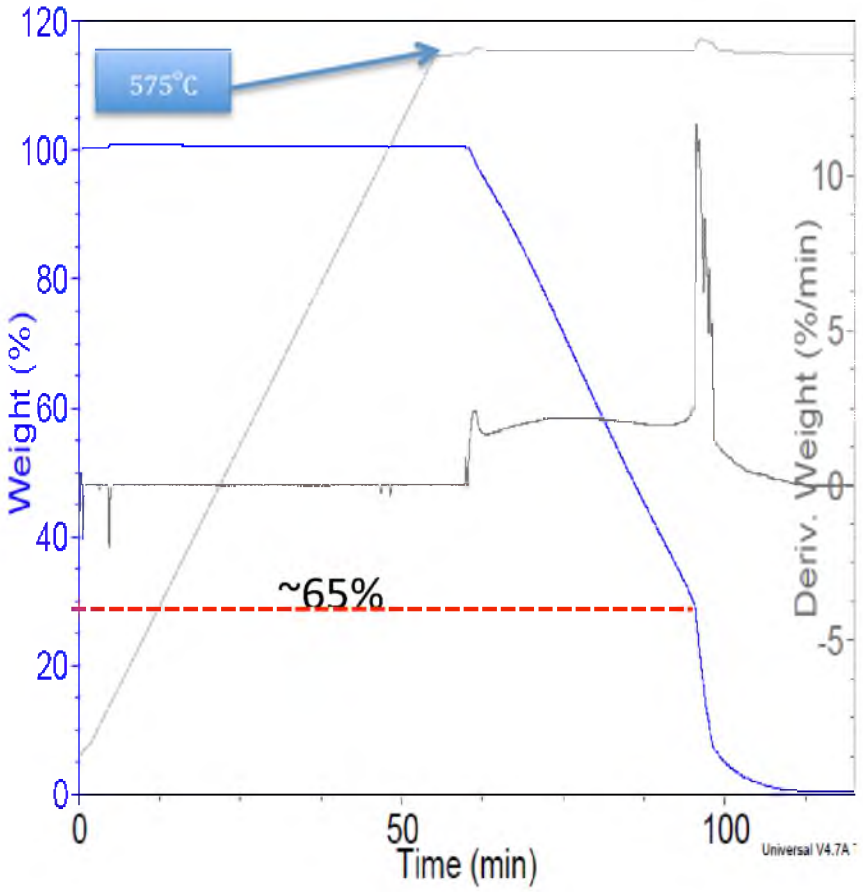

Figure 5.2 Sample differential scanning calorimeter (DSC) for the R250 at 575°C, weight % loss versus time. The kinetic rate constant for the sample changes drastically at 25 weight (%), attributed to changes in structure or composition of the sample.

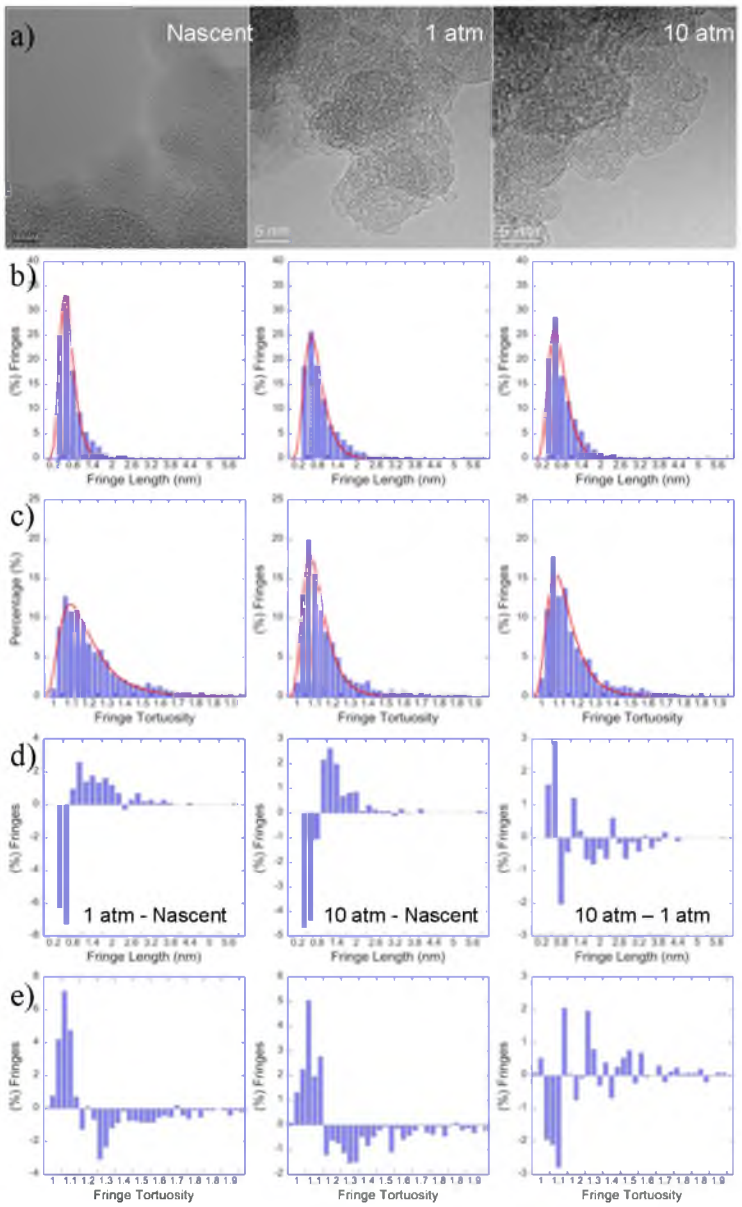

Figure 5.3 a) Images and image analysis of M1300 model carbon showing the histograms for fringe length and tortuosity. Nascent image and histograms show a high degree of tortuosity and shorter fringe lengths. The partially oxidized samples at both 1 atm and 10 atm show roughened surfaces, indicative of oxidation. Change in structure across the oxidation pressures was minimal.
Images are obtained from the HRTEM; histograms labeled b) Fringe Length show the concentration of fringe length in nanometers, histograms labeled c) Fringe Tortuosity show the concentration of the fringe tortuosity in nanometers. The images and histograms are aligned vertically corresponding to the Nascent, 1 atm, and 10 atm. Difference plots labeled d)1 atm-Nascent, 10 atm-Nascent, and 10-1 atm are aligned horizontally at the bottom of the figures and show how the change in pressure effects the fringe length. Those labeled e) Fringe Tortuosity are aligned below the difference plots are labeled 1 atm-Nascent, 10 atm-Nascent, and 10-1 atm show the changes in fringe tortuosity across pressures.

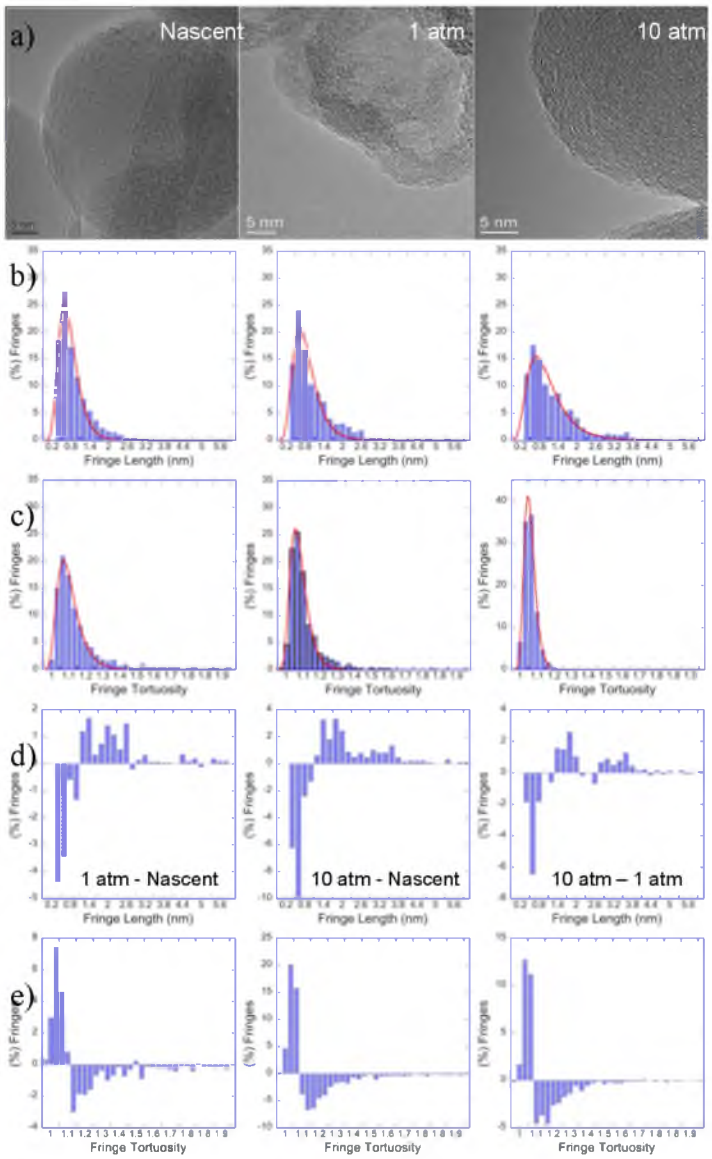

Figure 5.4 a) Images and image analysis of the R250 model carbon showing the histograms for fringe length and tortuosity. With increasing oxidation pressure, there is a progressive increase in structure, as manifested by the broadening of the lamella length distribution across the oxidation series, corresponding to longer lamella, and a narrowing of the tortuosity distributions, suggesting that the layer planes are becoming longer and have less curvature.

Images are obtained from the HRTEM; histograms labeled b) Fringe Length show the concentration of fringe length in nanometers, histograms labeled c) Fringe Tortuosity show the concentration of the fringe tortuosity in nanometers. The images and histograms are aligned vertically corresponding to the Nascent, 1 atm, and 10 atm. Difference plots labeled d) 1 atm-Nascent, 10 atm-Nascent, and 10-1 atm are aligned horizontally at the bottom of the figures and show how the change in pressure effects the fringe length. Those labeled e) Fringe Tortuosity aligned below the difference plots are labeled 1 atm-Nascent, 10 atm-Nascent, and 10-1 atm show the changes in fringe tortuosity across pressures.

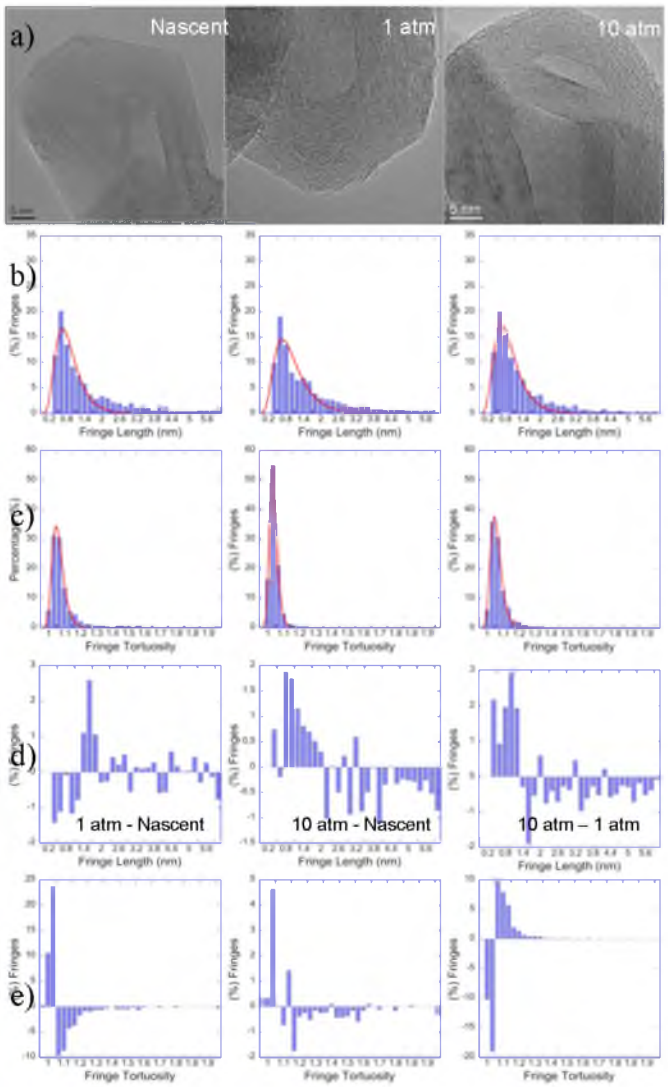

Figure 5.5 a) Images and image analysis of OLC model carbon showing the histograms for fringe length and tortuosity. Images for the nascent soot and partially oxidized samples in the TGA at pressures of 1 and 10 atm. The 1 atm images shows a decrease or a narrowing of the tortuosity distribution, signifying that the structure is flattening out. The 1 atm and the nascent soot are similar. For 10 atm, the fringe lengths decreased and the tortuosity increased, and the outer surface of the soot showed a broken or eaten structure. The latter observation signifies the penetration of oxygen into the outer portions of the soot particles.
Images are obtained from the HRTEM, histograms labeled b) Fringe Length show the concentration of fringe length in nanometers, histograms labeled c) Fringe Tortuosity show the concentration of the fringe tortuosity in nanometers. The images and histograms are aligned vertically corresponding to the Nascent, 1 atm, and 10 atm. Difference plots labeled d) 1 atm-Nascent, 10 atm-Nascent, and 10-1 atm are aligned horizontally at the bottom of the figure and show how the change in pressure effects the fringe length. Those labeled e) Fringe Tortuosity aligned below the difference plots are labeled 1 atm-Nascent, 10 atm-Nascent, and 10-1 atm show the changes in fringe tortuosity across pressures.

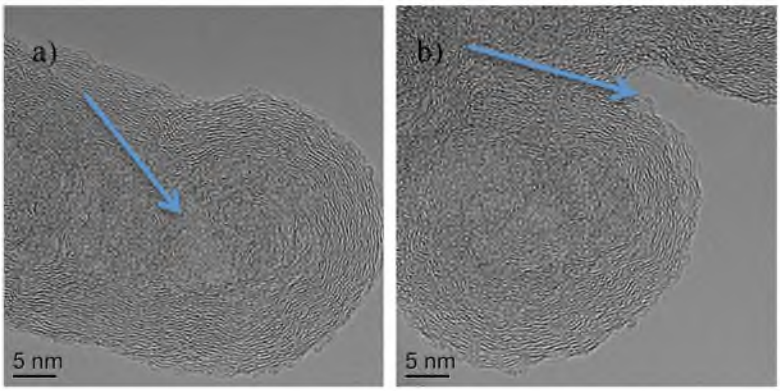

Figure 5.6 Images are R250 oxidized to 70% at 575°C. Evidence of a hollow shell formation in the sample, beyond 65% conversion, leading to a faster kinetic rate and lower activation energy. a) Illustrates the formation of the hollow shell. b) Illustrates the formation of the hollow shell and oxidation at the edge sites.

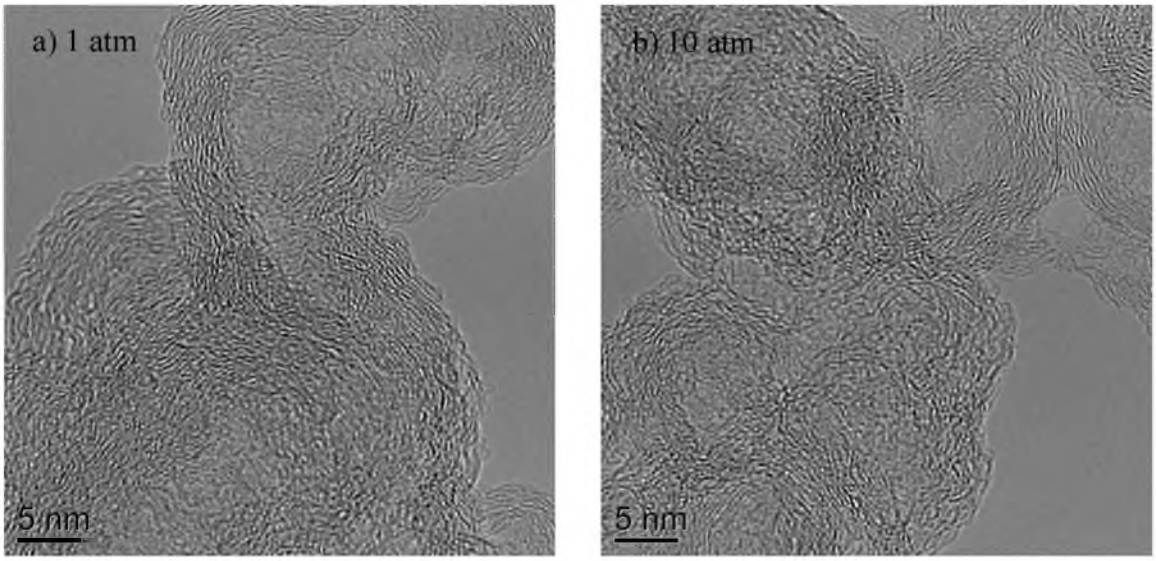

Figure 5.7 Images for the commercially produced diesel soot oxidized to 50% by weight in the TGA. On the left a) is the sample at 1 atm. Image on the right b) is pressurized to 10 atm. Visual inspection shows the similarity to R250 in structure and is also similar to the oxidation mode, forming hollow shells both inside the particle and on the edges. Quantification using image analysis is necessary for further investigation.

Table 5.1 Temperature range of TGA experiments performed on the model carbons and diesel soot.

Sample	**Temperature Range [°C]**
M1300	550-650
R250	550-700
Diesel	550-650
OLC	575-775

Table 5.2 Kinetic parameters, activation energy and pre-exponential factor, for the model carbons and diesel soot, over a range of temperatures and conversion from 0.2 to 0.6, listed in ascending order with the r-squared value.

Sample	Fractional Conversion	Temperature Range (^oC)	Activation Energy (kJ/mol)	Pre-exponential Factor (Pa^{-1} min^{-1})	R^2
M1300	0.2-0.6	575-650	124	9.82E+02	0.97
Diesel	0.2-0.6	575-650	139	8.15E+02	0.92
R250	0.2-0.6	575-700	141	6.75E+02	0.95
OLC	0.1-0.6	600-700	204	2.25E+05	0.98

Table 5.3 Kinetic rate constants for the model carbons and diesel soot samples analyzed over the range of isothermal temperatures.

Sample	k_c@ 575^oC (Pa^{-1} min^{-1})	k_c@ 600^oC (Pa^{-1} min^{-1})	k_c@ 625^oC (Pa^{-1} min^{-1})	k_c@ 650^oC (Pa^{-1} min^{-1})	k_c@ 700^oC (Pa^{-1} min^{-1})
M1300	2.05E-05	3.04E-05	6.20E-05	7.95E-05	1.7E-04
Diesel	2.21E-06	3.58E-06	9.09E-06	9.50E-06	1.80E-06
R2500	1.77E-06	3.13E-06	7.60E-06	1.29E-05	1.98E-05
OLC	2.38E-07	1.71E-07	2.54E-07	6.69E-07	2.76E-06

Table 5.4 Median values for fringe length and tortuosity for all model carbons

	Fringe Length (nm)	Fringe Tortuosity
R250		
Nascent	0.9	1.2
1 atm	1.02	1.16
10 atm	1.16	1.1
Onion		
Nascent	1.4	1.12
1 atm	1.38	1.08
10 atm	1.18	1.11
M1300		
Nascent	0.8	1.31
1 atm	0.91	1.2
10 atm	0.88	1.22

CHAPTER 6

INFLUENCE ON OXYGENATED FUEL SURROGATE FORMULATION ON SOOT OXIDATION BEHAVIOR AND NANOSTRUCTURE: EXAMINATION USING X-RAY PHOTOELECTRON SPECTROSCOPY (XPS), HIGH-RESOLUTION TRANSMISSION ELECTRON MICROSCOPE (HRTEM) AND THERMOGRAVIMETRIC ANALYSIS (TGA)

6.1 Introduction

This study investigated the effects of adding *n*-butanol to *n*-dodecane (10, 20, 30, 40, 60 mole%) on nanostructure, kinetic rate constant, surface functional groups (SFGs) and stability of the soot. The fuels used have been previously discussed in sections 3.1 and 3.1.3. Soot was created using the flat-flame premixed burner, collected on the water-cooled stabilization plate, crushed and placed in a nitrogen evacuated glass vial. Changes in soot oxidation kinetics, using a thermogravimetric analyzer (Q600 TGA), were investigated with comparisons to SFGs (Kratos Axis Ultra DLD X-Ray photoelectron spectroscopy) and nanostructure (high-resolution transmission electron microscopy) of the differing compositions. A Kratos Axis Ultra DLD was used to collect all XPS spectra. A basic description the XPS analysis is presented in section 3.5.

6.2 Results and Discussion

6.2.1 Impact of *n*-butanol Content on Soot Oxidation Reactivity

Figure 6.1 shows the apparent kinetic rate constant for the samples with the 10, 20, 30, 40, and 60 mol% *n*-butanol and *n*-dodecane at 650°C. Results suggest that with an increase in *n*-butanol from 10 to 20% *n*-butanol, the kinetic rate constant was higher, resulting in faster kinetics and a less stable soot. The 30% *n*-butanol sample exhibited a lower rate constant leading to a slower oxidation and more stable soot. With the addition of 40% *n*-butanol the kinetic rate constant increased, and with 60% *n*-butanol the kinetic rate constant decreased slightly.

6.2.2 Impact of SFGs on Soot Oxidation Reactivity

Soot reactivity and nanostructure are closely tied to the functional groups and active sites on the surface of the soot. SFGs (surface functional groups), sp^2, sp^3 and oxygenated SFGs, carbonyl and phenol groups are generated as intermediates from partial oxidation of soot (*6, 7, 8*). These groups provide a greater number of active sites, which aid in the oxidation of soot. Thermal decomposition of SFGs at these sites can physically and chemically reduce the barriers to the lamella realignment and altering of the soot nanostructure (*8*). To gain a better understanding of the oxidation kinetics and the changes in nanostructure, a study of SFGs was conducted. XPS analysis was used to identify the binding energy signatures of elemental carbon and oxygen on the soot surface. A typical XPS survey scan is shown in Figure 6.2. Carbon and oxygen were detected on the surface of the soot sample, based on their binding energy signature. The large content of O-atoms is associated with the oxygenated SFGs bonded to carbon on the

soot surface. To facilitate elemental comparison, the elemental compositions of O-atoms and C-atoms on the soot surface have been calculated from the area of the O 1s and C 1s peaks.

Deconvolution of the overlapping C1s peaks of the XPS spectrum allow for identification of the SFGs by relative peak position. Figure 6.3 is an example of a high-resolution scan of the C1s peak for the 10% *n*-butanol/90% *n*-dodecane soot sample. The extended and asymmetric shape C 1s peak implies that multiple peaks are evident. The high-resolution scan is used to fit three to four separate peaks, corresponding to the C-C sp^2 at 284.5 eV; C-C sp^3 at 285.2 eV; C-OH (Phenol) at 286.3 eV; and C=O (Carbonyl) at 288.2 eV (*4, 5, 6*). Care was taken to ensure that the separation of the peaks was greater than resolution of the Kratos instrument of 0.5 electron volts, and a minimum number of peaks were used in achieving a good fit. Curve fitting of the high-resolution C 1s region used Gauss-Lorenz peaks and a Shirley fit to give the best and most accurate results. CasaXPS software was used for fitting and identification of the peaks. Information was imported into an Excel plot for visualization and quantification, shown in Figure 6.4. Concentrations of the SFGs were quantified from the relative intensities of the corresponding peaks (*10, 11, 12*). The percentages of SFGs in the soot samples are presented in Figure 6.5. No significant changes are seen with an increase in *n*-butanol. The sp^2/ sp^3 ratio is related to the amount of aliphatic C-H groups on the soot surface. The aliphatic C-H groups are considered reactive sites that have an impact on oxidation reactivity of soot (*17, 18*). Figure 6.6 shows the ratio of sp^2/ sp^3 in the soot samples related to the amount of *n*-butanol and the kinetic rate constant. Once again, there does not seem to be a correlation with the percentage of *n*-butanol in the fuel, and how the sp^2/

sp^3 ratio affects the kinetic rate constant. A lower sp^2/ sp^3 ratio relates to a higher oxidation kinetic rate constant.

6.2.3 Investigation of Soot Nanostructure and Soot Oxidation Reactivity

Initial visual HRTEM image analysis shows that with an increase in *n*-butanol there is an increase in disorder of the structure. This implies that the structure is becoming less stable and easier to oxidize (*1-4*). Again, at 30% *n*-butanol the nanostructure appears to be more organized and therefore more stable. Figures 6.7 and 6.8 are the HRTEM images of soot collected from the flat-flame premixed burner, fuel mixture of 10% *n*-butanol and 90% *n*-dodecane and 20% *n*-butanol and 80% *n*-dodecane, suggesting that the structure is becoming less organized and the kinetic rate constant of oxidation is increasing with the increase of *n*-butanol. This can be seen by the short and curved fringe lengths. Visual inspection of the images shows that they are overall disorganized. Figure 6.9 is the HRTEM images of soot collected from the flat-flame premixed burner, fuel mixture of 30% *n*-butanol and 70% *n*-dodecane, showing a higher degree of structure and organization, correlating to the lower kinetic rate and a more stable soot (*17, 18*). The longer fringe lengths and the less curved fringes present in the images give the overall visual impression of a more ordered structure. Figure 6.10 shows HRTEM images of soot collected from the flat-flame premixed burner, with 40% *n*-butanol and 60% *n*-dodecane, returning to the less organized structure with an increase in *n*-butanol percentage, and an increase in the kinetic rate constant, relating to a decrease in

soot stability. Figure 6.11 illustrates that as the percentage of *n*-butanol increases, the structure decreases, and the related kinetic rate is increasing.

6.3 Summary and Conclusions

This study investigated the effect of adding *n*-butanol to *n*-dodecane, ranging from 10-60% *n*-butanol to form a biodiesel surrogate. The results show how an increase in *n*-butanol changed the nanostructure, kinetic rate constant, and the stability of the soot. With an increase in *n*-butanol from 10 to 20%, the kinetic rate constant was higher resulting in faster kinetics, less stable soot and was easier to burn. With 30% *n*-butanol addition to *n*-dodecane, the rate constant became lower leading to a slower oxidation and more stable soot.

Visually analyzing the HRTEM images shows that with an increase in *n*-butanol there is an increase in disorder of the structure thus, implying that the structure is becoming less stable and easier to oxidize. With 30% *n*-butanol addition to *n*-dodecane, the nanostructure appears to be more organized and therefore more stable, correlating to the oxidation kinetic rate. Image analysis needs to be conducted to quantify the initial visual findings of the soot nanostructure.

XPS analysis allowed for the identification of C-C sp^2 at 284.5 eV; C-C sp^3 at 285.2 eV; C-OH (Phenol) at 286.3 eV; and C=O (Carbonyl) at 288.2 eV. By relative peak position, concentrations of the SFGs were quantified from the relative intensities of the corresponding peaks. The results indicate that there was not a significant difference in SFG percentages to make a correlation to kinetic rate or nanostructure.

6.4 References

1. Vander Wal R. L.; Tomasek A. J., Soot Oxidation: Dependence Upon Initial Nanostructure. Combustion and Flame **2003,** *134*, 1-9.

2. Vander Wal R. L.; Tomasek A. J.; Street K.; Hull D. R.; Thompson W. K., Carbon Nanostructure Examined by Lattice Fringe Analysis of High-Resolution Transmission Electron Microscopy Images. Applied Spectroscopy **2004,** *58*, 230-237.

3. Vander Wal R. L.; Mueller C. J., Initial Investigation of Effects of Fuel Oxygenation on Nanostructure of Soot from Direct-Injection Diesel Engine. Energy & Fuels **2006,** *20*, 2364-2369.

4. Vander Wal R. L.; Yezerets A.; Currier N. W.; Kim D. H.; Wang C. M., HRTEM Study Of Diesel Soot Collected From Diesel Particulate Filters. Carbon **2007,** *45*, 70-77.

5. Boehman A. L.; Song J.; Alam A., Impact of Biodiesel Blending on Diesel Soot and the Regeneration of Particulate Filters. Energy and Fuels **2005,** *19*, 1857-1864.

6. Gilot, P.; Bonnefoy, F.; Marcuccilli, F.; Prado, G., Determination Of Kinetic Data For Soot Oxidation. Modeling The Competition Between Oxygen Diffusion And Reaction During Thermogravimetric Analysis. Combustion and Flame **1993,** *95*, 87-100.

7. Marcucilli F.; Gilot P.; Stanmore B. R.; Prado G., Experimental And Theoretical Study Of Diesel Soot Reactivity. The Combustion Institute **1994,** 619–26.

8. Otto K.; Sieg M. H.; Zinbo M.; Bartosiewicz L., The Oxidation Of Soot Deposits From Diesel Engines. **1981,** SAE 800336.

9. Brilhac J.F.; Bensouda F.; Gilot P.; Brillard A.; Stanmore B., Experimental And Theoretical Study Of Oxygen Diffusion Within Packed Beds Of Carbon Black. Carbon **2000,** 1011– 9.

10. Soete G., Catalysis Of Soot Combustion By Metal Oxides. The Combustion Institute **1988.**

11. Hufner S., Photoelectron Spectroscopy. Solid State Science Series; Springer: Berlin, **1995.**

12. Briggs D.; Seah (Eds.), Practical Surface Analysis by Auger and X-ray Photoelectron Spectroscopy; John Wiley & Sons: Chichester, **1983.**

13. Briggs D.; Grant (Eds.), Surface Analysis by Auger and X-ray Photoelectron Spectroscopy; IM Publications: Chichester, **2003.**

14. Fadley C. S.; Electron Spectrosc. Relat. Phenom. **2010,** 178/179, 2.

15. Briggs D.; Grant J. T.; Briggs D.; Grant (Eds.), Perspectives on XPS and AES Surface Analysis by Auger and X-ray Photoelectron Spectroscopy; IM Publications: Chichester, **2003,** 1-12.

16. Moulder J. F.; Stickle W. F.; Sobol P. E.; Bomben K. D.; Handbook of X-ray Photoelectron Spectroscopy; Perkin-Elmer Corp: Eden Prairie, MN, **1992.**

17. Williams S., Surface Intermidiates, Mechanism and Reactivity of Soot Oxidation; Ph.D. thesis, University of Toronto, Toronto, **2008.**

18. Wang L.; Song C., Aliphatic C–H And Oxygenated Surface Functional Groups Of Diesel In-Cylinder Soot: Characterizations And Impact On Soot Oxidation Behavior. Proceedings of the Combustion Institute **2013,** *34*, 2, 3099-3106.

19. Al-Qurashi K.; Boehman A., Impact Of Exhaust Gas Recirculation (EGR) On The Oxidative Reactivity Of Diesel Engine Soot. Combustion and Flame **2008,** *155*, 4, 675-696.

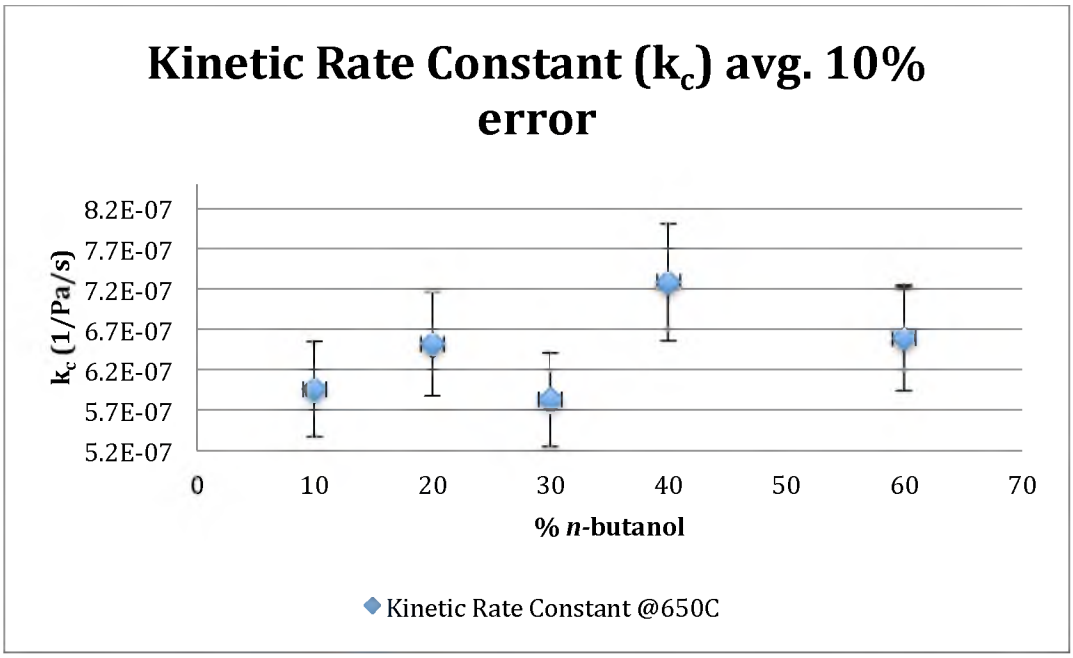

Figure 6.1 Kinetic rate constant for all the fuel combinations. With an increase in *n*-butanol up to 20% the kinetic rate constant increased, resulting in faster kinetics and a less stable soot; at 30% *n*-butanol the kinetic rate constant decreased leading to slower oxidation and a more stable soot; 40% to 60% showed a general increase in the kinetic rate constant.

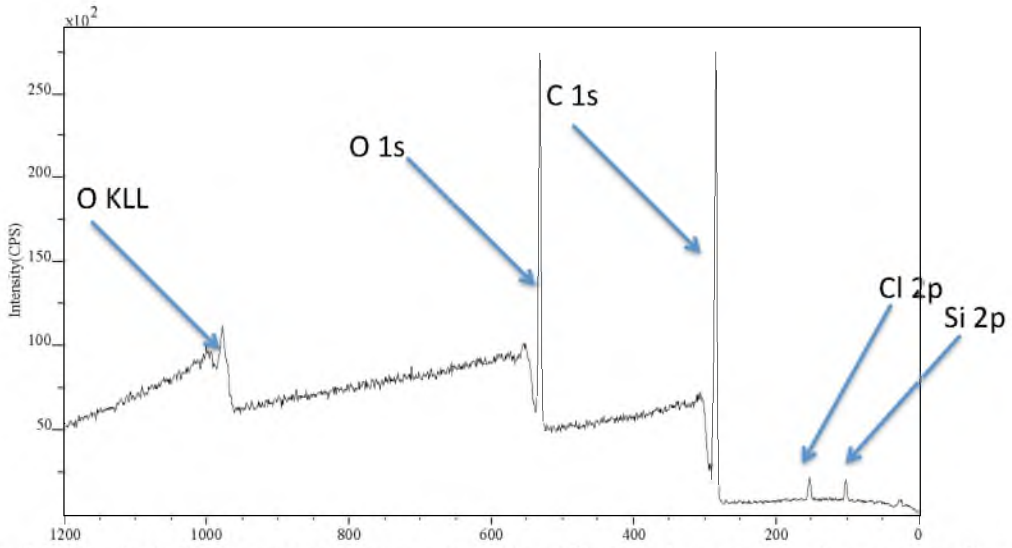

Figure 6.2 Typical XPS survey scan used to identify the elements on the soot surface, based on the element's binding energy. Oxygen and carbon were found in the greatest amount with traces of chlorine and silicon from contaminants.

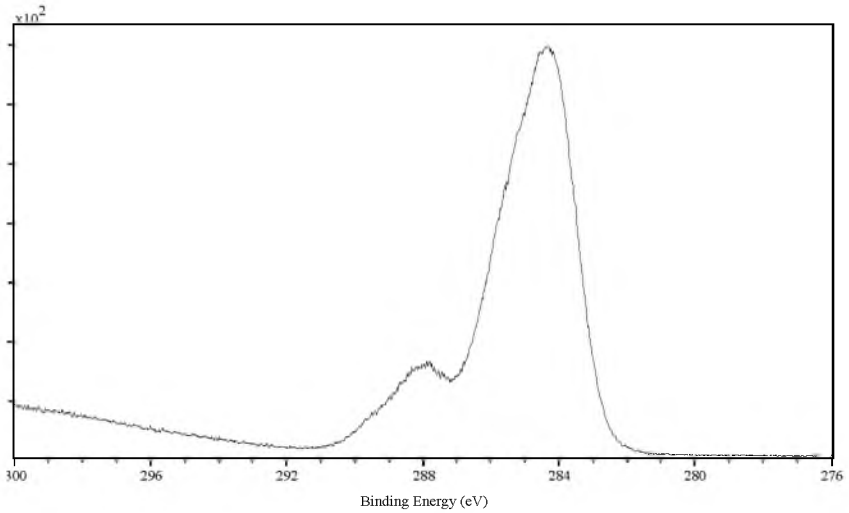

Figure 6.3 High-resolution scan of the Carbon 1s peak, used for identification of the surface functional groups.

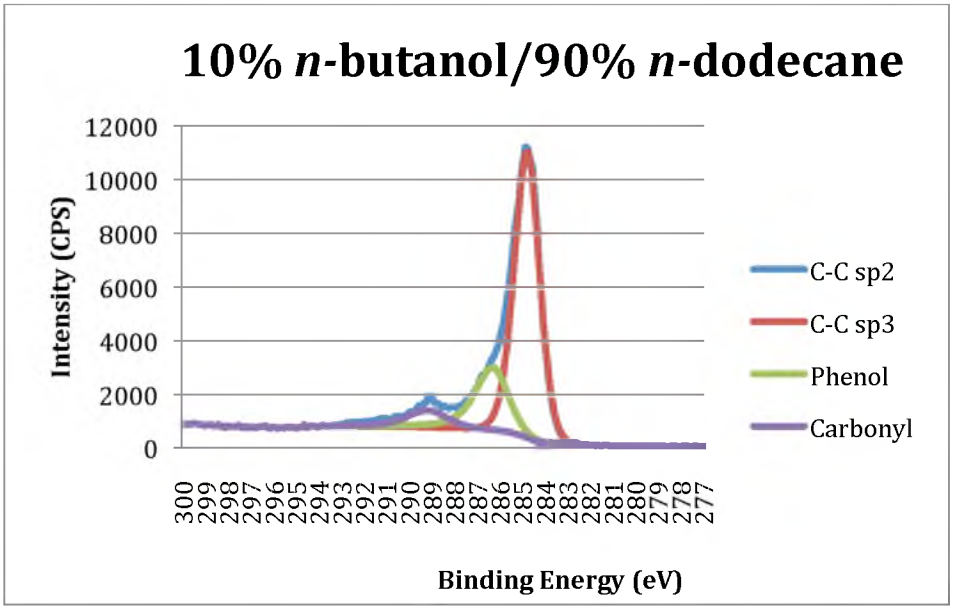

Figure 6.4 The C1s peak fitted using four separate peaks, correspond to the C-C sp^2 at 284.5 eV; C-C sp^3 at 285.2 eV; C-OH (Phenol) at 286.3 eV; and C=O (Carbonyl) at 288.2 eV. C-C sp^2 and C-C sp^3 have the largest areas indicating the largest amount of bonds present. Phenol and carbonyl groups have significantly smaller percentages.

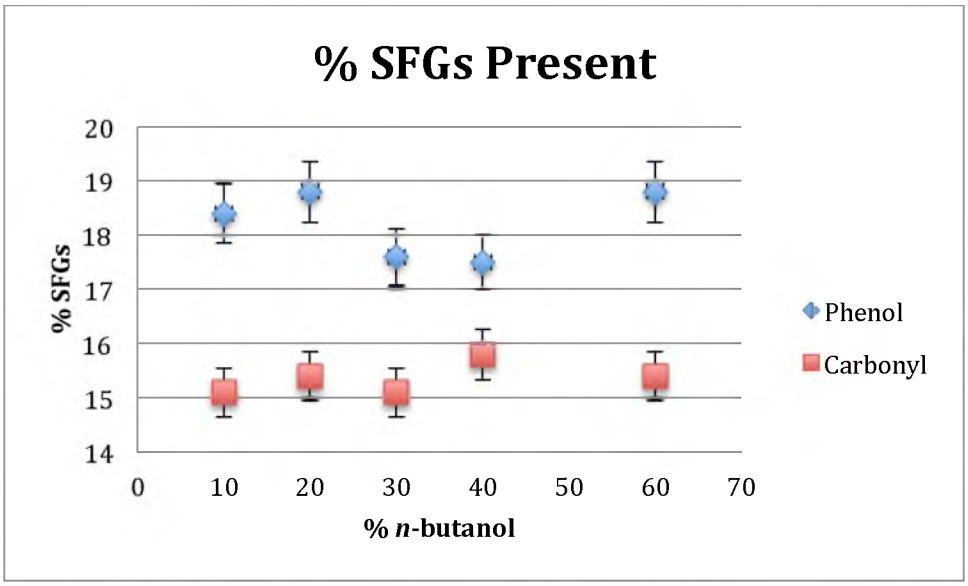

Figure 6.5 Showing the percentage of the functional group detected on the surface of the soot sample. Results show no significant change in percentage of functional group as a function of percent *n*-butanol.

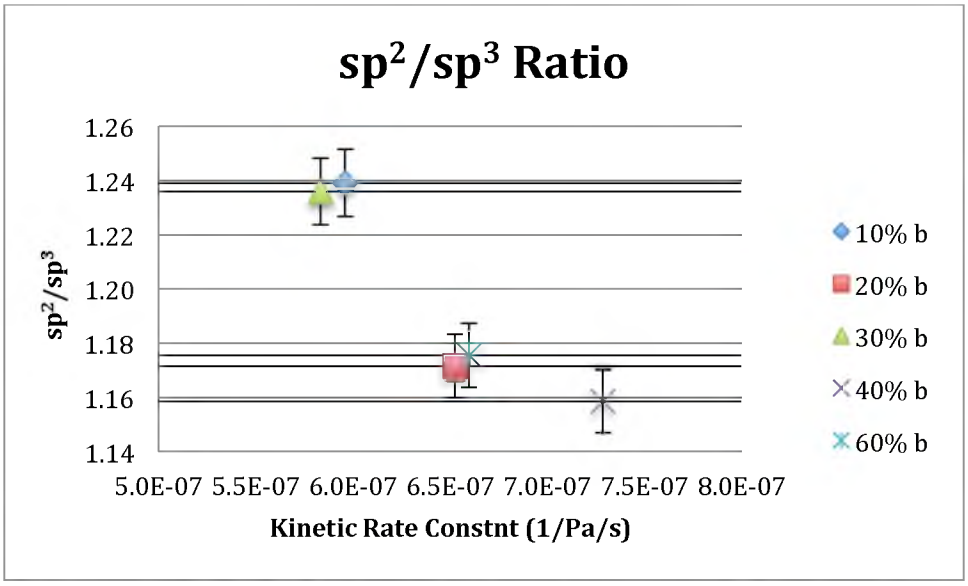

Figure 6.6 sp^2/sp^3 ratio for all fuel combinations compared to the kinetic rate constant at 650°C. Results show no significant correlation between sp^2/sp^3 ratio and kinetic rate constant. Results indicate that lowest sp^2/sp^3 ratio is related to the highest kinetic rate constant.

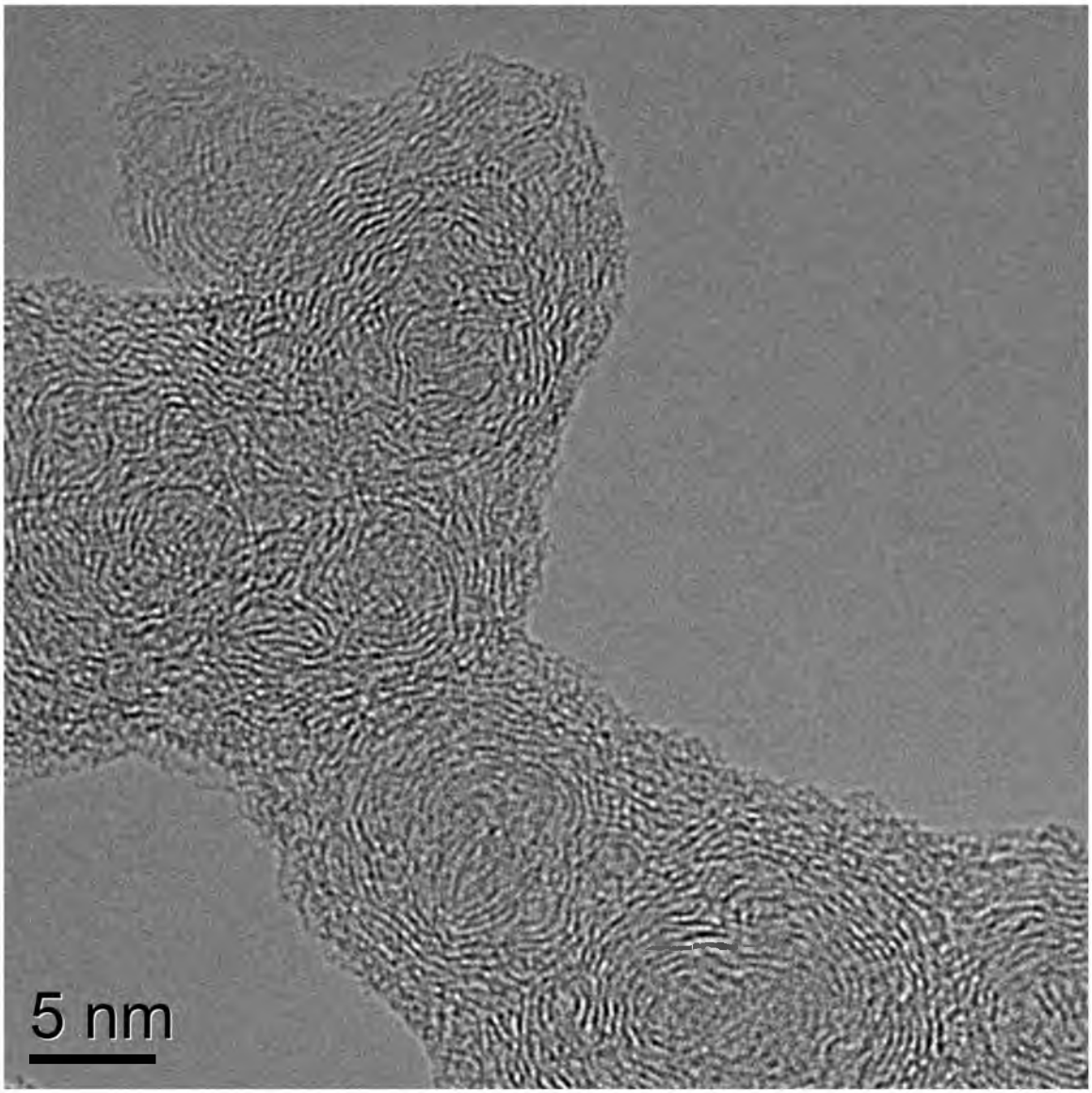

Figure 6.7 HRTEM images of soot collected from the flat-flame premixed burner, fuel mixture of 10% *n*-butanol and 90% *n*-dodecane, showing a disorganized amorphous structure.

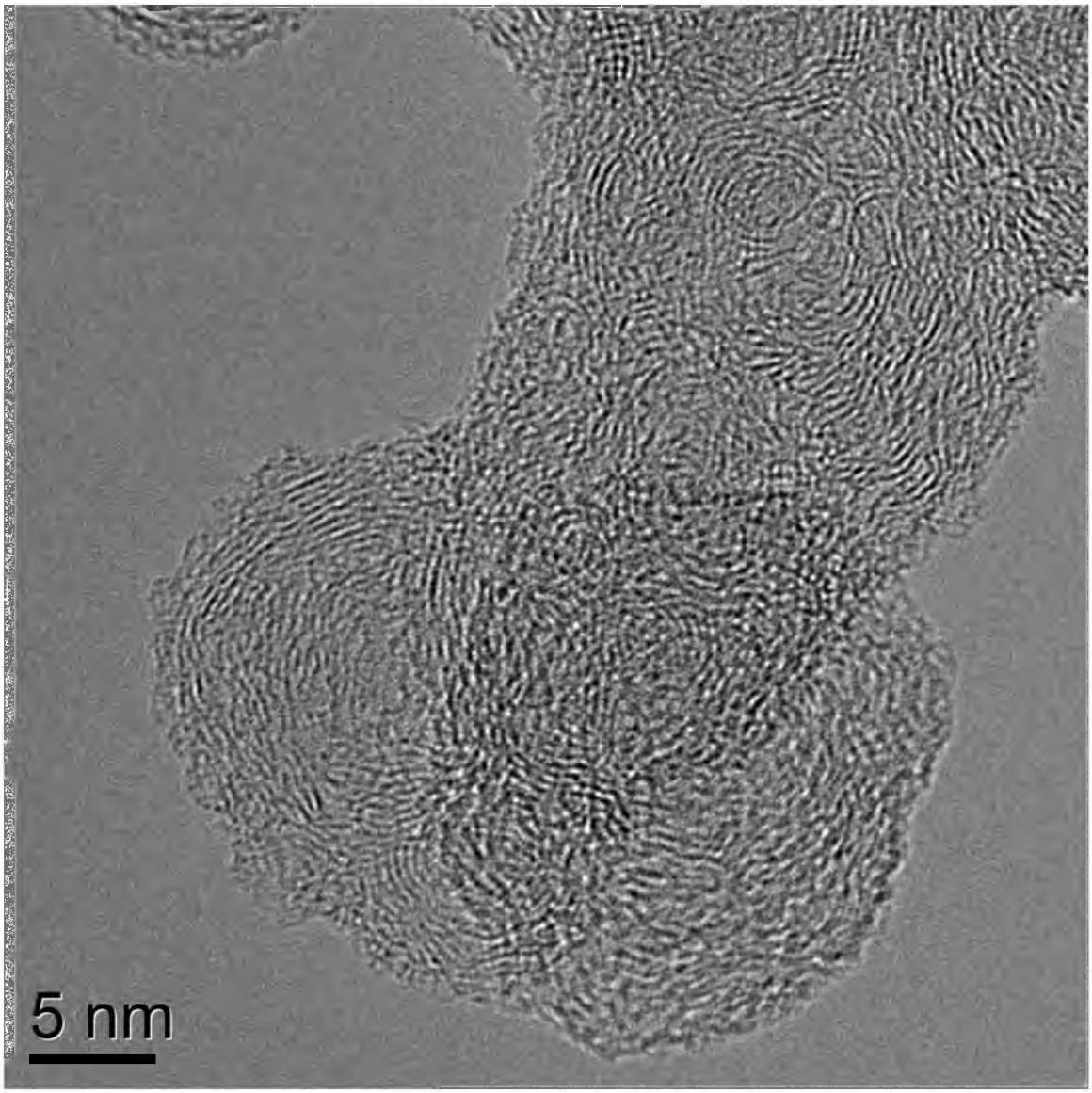

Figure 6.8 HRTEM images of soot collected from the flat-flame burner, fuel mixture of 20% *n*-butanol and 80% *n*-dodecane, showing that the structure is more disorganized than that of the previous fuel combination.

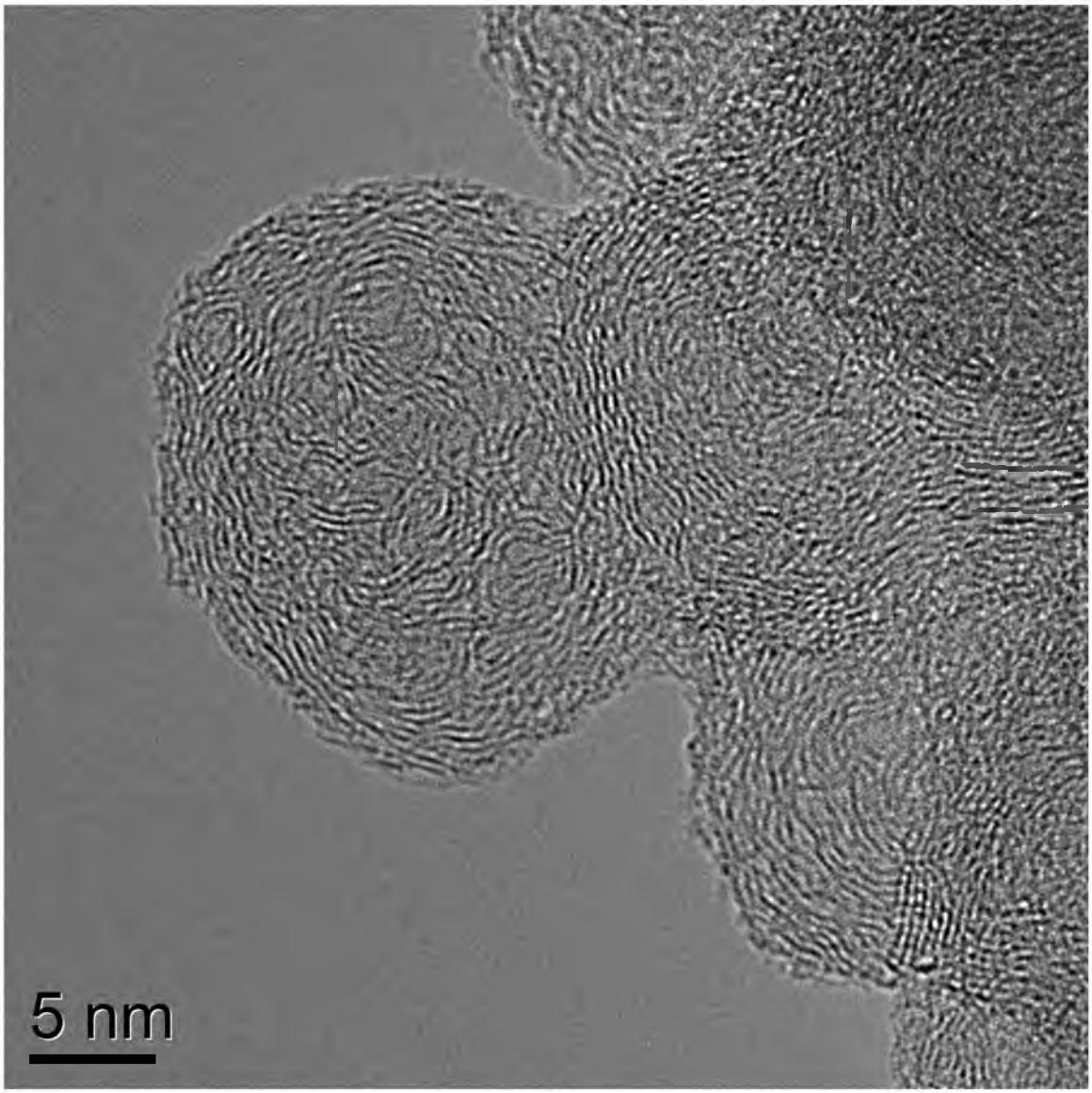

Figure 6.9 HRTEM images of soot collected from the flat-flame premixed burner, fuel mixture of 30% *n*-butanol/ and 70% *n*-dodecane, showing a higher degree of structure and organization.

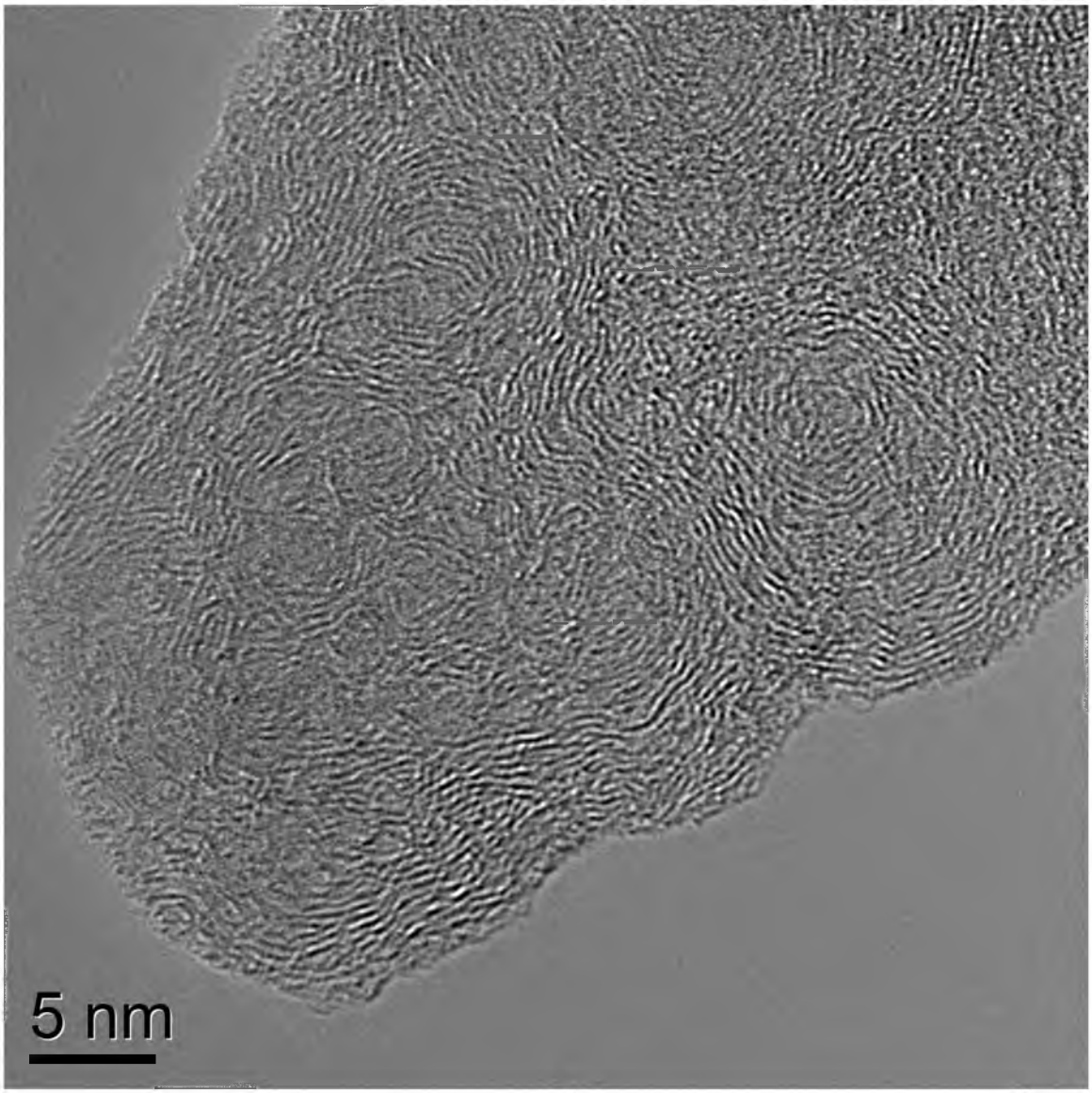

Figure 6.10 HRTEM images of soot collected from the flat-flame premixed burner, fuel mixture of 40% *n*-butanol and 60% *n*-dodecane, returning to the less organized structure with an increase in the *n*-butanol percentage.

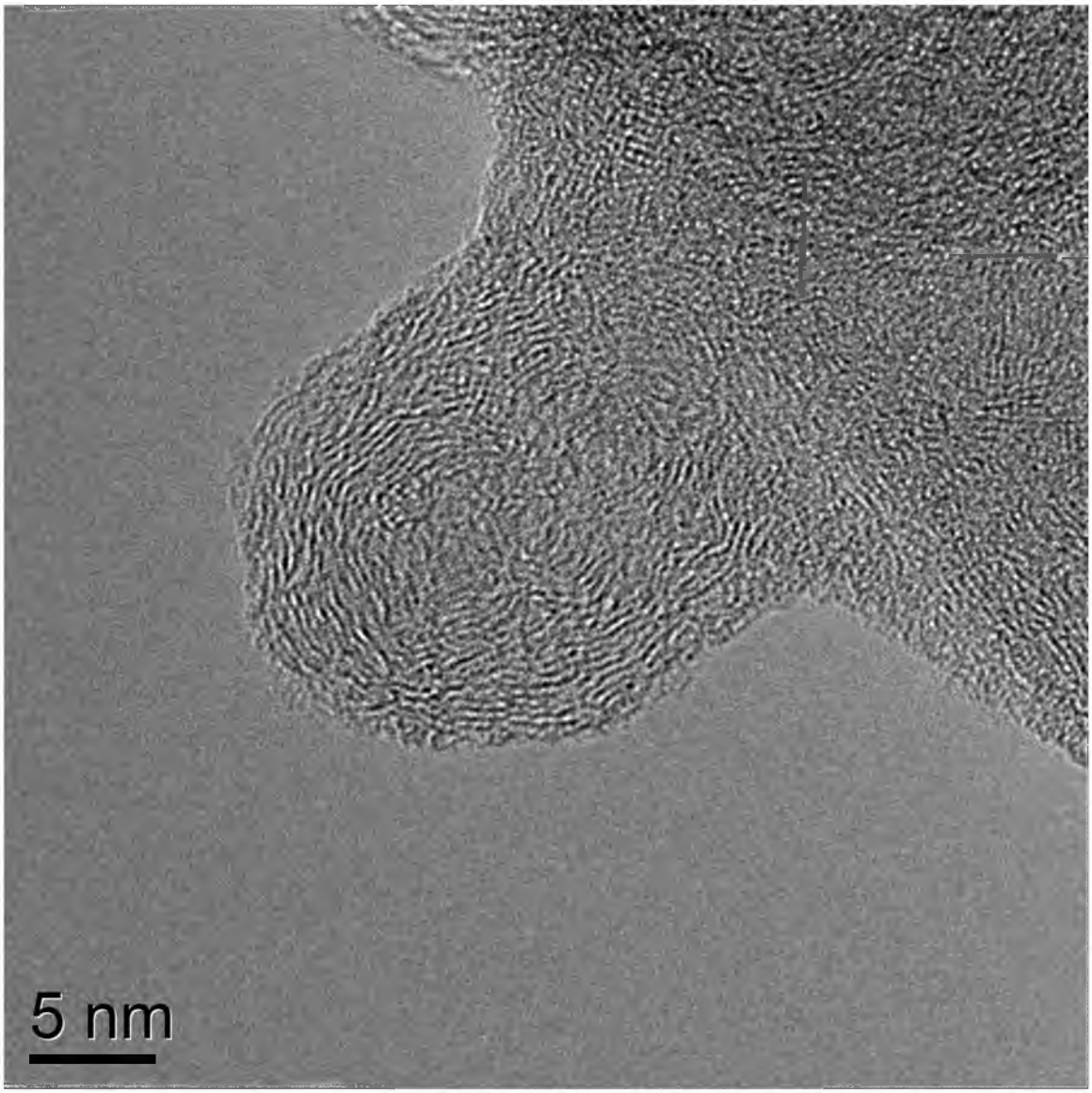

Figure 6.11 HRTEM images of soot collected from the flat-flame premixed burner, fuel mixture of 60% *n*-butanol and 40% *n*-dodecane, showing the less structured soot coinciding with the increase in *n*-butanol.

CHAPTER 7

CONCLUSION AND RECOMMENDATIONS

The focus of this research was to better understand the fundamental mechanism behind oxidation kinetics of soot. An in depth study led to insights on how soot oxidation kinetics were affected by nanostructure, surface functional groups (SFGs, C-C sp^2, C-C sp^3, phenol, carbonyl and carboxylic), pressure, and type of fuel. The findings of this research can be used to develop kinetic models for soot oxidation that will be used in combustion models.

The structure of soot changed as a function of oxygenated fuel addition, and oxidation kinetics varied greatly as a result of these changes. The fuel type had an effect on the ordering of microstructures of graphene within soot particles, as determined by HRTEM analysis. This knowledge can be used to design fuel combinations that create soot that is easily burned and aid in the reduction of carbonaceous material pollutants.

There is currently little understanding of the variations in soot nanostructure and its dependence upon pressure. Most practical systems for power generation operate at elevated pressures, upwards of 15 times atmospheric pressures. Exploring the changes created at elevated pressures in the nanostructure of soot and the impact on oxidation kinetics is a new frontier in the study of these fundamental mechanisms. The reduction

of particulate emission after the addition of oxygenated fuels has been studied, but further investigation could be explored focusing on changes in nanostructure and SFGs.

The experimental techniques used in this research, along with measurements of flame temperature, SFG's, kinetic parameters and soot nanostructure allowed for identification of major characteristics that will improve the existing kinetic models and provide better understanding of the processes of soot oxidation in combustion systems. Continued research will generate a correlative database relating physical soot nanostructure, and its dependence on fuel type, pressure and their respective role in the changes in oxidation kinetics.